UNIVERSIDAD NACIONAL AUTÓNOMA DE MEXICO
POSGRADO EN CIENCIAS FÍSICAS
INSTITUTO DE CIENCIAS NUCLEARES

GRAVEDAD Y PRESIÓN DE RADIACIÓN EN REGIONES H II

T E S I S
QUE PARA OPTAR POR EL GRADO DE:
DOCTOR EN CIENCIAS (FÍSICA)

PRESENTA:
JUAN CARLOS RODRÍGUEZ RAMÍREZ

TUTOR PRINCIPAL:

DR. ALEJANDRO CRISTIAN RAGA RASMUSSEN
INSTITUTO DE CIENCIAS NUCLEARES, UNAM

MIEMBROS DEL COMITÉ TUTOR:

DR. JORGE DANIEL CANTÓ ILLA
INSTITUTO DE ASTRONOMÍA, UNAM

DR. PABLO FABIÁN VELÁZQUEZ BRITO
INSTITUTO DE CIENCIAS NUCLEARES, UNAM

CIUDAD DE MÉXICO, MAYO DE 2017.

Gravity and Radiation Pressure in HII Regions

Dedico esta tesis a mis padres Rocío y Juan,
a mi asesor y amigo Alejandro,
a mi novia Elena,
a mis amigos Uziel, Marco, Alejandra, Yuri, Adrianita, Gloria, Aldo, Manuel, Vero,
y a la memoria de Juan René y Angie.

Agradecimientos

Los resultados de este trabajo se obtuvieron en colaboración de mi asesor el Dr. Alejandro Raga, a quien agradezco enormemente mi formación académica y personal.

Agradezco también a los miembros de mi Comité Tutorial el Dr. Pablo Velázquez y el Dr. Jorge Cantó, por su ayuda y asesoría durante el doctorado.

A los miembros del jurado de esta tesis, Dra. Catalina Stern, Dr. Luis Felipe Rodríguez, Dr. William Henney y Dr. Sergiy Silich, por la revisión y sugerencias enriquecedoras a esta tesis.

A la M. C. Elena Atkinson por las correcciones de estilo en este texto.

Al Consejo Nacional de Ciencia y Tecnología por la beca para realizar la investigación de doctorado.

Al Instituto de Ciencias Nucleares por el espacio otorgado para realizar esta investigación.

Agradezco con mucho afecto a la UNAM por toda mi formación académica.

Resumen

Durante su nacimiento, tiempo de vida y muerte las estrellas masivas (de masa > 20 $M_\odot$) liberan momento y energía que interactúa con el medio interestelar (ISM) que las forma. Este tipo de estrellas producen regiones HII expansivas cuando nacen, pierden masa mediante vientos estelares a lo largo de su vida, y explotan como supernovas (SNe) cuando mueren. Esta tesis se enfoca en el efecto de la presión de radiación en regiones HII, así como también en remanentes de SN que se expanden dentro de un viento de cúmulo estelar preexistente.

Primero estudiamos de manera analítica el efecto de la presión de radiación en regiones HII esféricas, que es el mismo problema estudiado numéricamente por Draine (2011). Obtenemos una solución analítica aproximada para la estructura nebular. Esta solución está determinada por la luminosidad de la estrella central L_*, la sección eficaz de absorción del polvo σ_d y el radio exterior de la nebulosa R_s. Comparamos nuestra solución analítica con integraciones numéricas de las ecuaciones de Draine, encontrando muy buen acuerdo entre ambos modelos. De nuestra solución analítica derivamos que la presión de radiación crea cavidades centrales considerables en regiones HII cuando se cumple que $R_s \lesssim \sigma_d L_*/(8\pi ckT)$, donde k es la constante de Boltzmann, c es la velocidad de la luz y $T \sim 10^4$ K es la temperatura típica de las regiones HII. Además, en una región fotoionizada con tal configuración, ya no hay un efecto de reducción de volumen (el cual tiene lugar en modelos anteriores de regiones HII con polvo, que no consideran la presión de radiación).

Extendemos el análisis del caso esférico al caso de una distribución de fuentes de radiación en un plano. Esta configuración es relevante para modelar episodios de formación estelar en discos galácticos o en formación estelar producida por colisiones frontales de nubes moleculares. Obtenemos la estructura vertical del ISM alrededor de una distribución plana de estrellas, mediante soluciones semi-analíticas de las

ecuaciones del modelo, en el que también se toma en cuenta la masa de las estrellas y la auto-gravedad del gas. Estas soluciones son perfiles hidrostáticos de regiones fotoionizadas planas, que están en balance de presión con una capa neutra envolvente. Esta estructura tiene distintas extensiones (tanto de la zona fotoionizada como de la neutra) de acuerdo a la configuración de los parámetros del sistema. Evaluamos la estabilidad gravitacional de la zona neutra de las soluciones, encontrando que la mayoría de ellas son estables. Sin embargo, encontramos algunas soluciones inestables donde hay formación estelar subsecuente, producida por los efectos combinados de la auto-gravedad del gas y la presión de radiación.

En el útimo capítulo de esta tesis desarrollamos un modelo semianalítico de un remanente de SN que se expande en el centro de un viento de cúmulo estelar. Del modelo semianalítico se obtiene el radio de la burbuja del material expulsado, y el radio del choque externo del remanente como función del tiempo.

Encontramos que en el caso de supernovas tipo II, el remanente generalmente alcanza la fase T-S afuera del cúmulo. En este caso el choque reverso del remanente de SN nunca regresa al centro de la explosión, expandiénsode siempre detrás de la discontinuidad de contacto. Calculamos la luminosidad de rayos X del flujo resultante y encontramos por ejemplo que para un cúmulo de 1000 estrellas O dentro de un radio de 2.5 pc, el remanente de SN aumenta la luminosidad de rayos X del del cúmulo en $\sim$ 3 ordenes de magnitud. Este incremento de luminosidad decae en un período de $\sim$ 1000 años a su valor original (antes de la explosión de SN). Los modelos de este capítulo podrían ser aplicados para interpretar observaciones en rayos X de cúmulos de estrellas masivas.

Las aportaciones principales de esta tesis también pueden encontrarse en los artículos de Rodríguez-Ramírez et al. (2014), Rodríguez-Ramírez & Raga (2016) y Rodríguez-Ramírez et al. (2016).

Abstract

During their formation, life-time, and death, massive stars (with mass > 20 $M_\odot$) release energy and momentum that interact with their forming interstellar medium (ISM). These type of stars produce expanding HII regions when they are formed, lose mass through stellar winds during their life, and to explode as supernovae (SNe) when they die. This thesis focuses on the effect of radiation pressure in HII regions as well as SN blast waves that expand in a pre-existing star cluster wind. The motivation for these studies are the difficulties that the standard models of wind-bubbles face to explain the properties of particular interstellar bubbles.

We first study analytically the effect of radiation pressure on spherical HII regions, which is the same problem studied numerically by Draine (2011). We obtain an analytic approximate solution for the nebular structure. This solution is determined by the luminosity of the central star L_*, the dust absorption cross section σ_d, and the external boundary of the nebula R_S. We compare our analytic solution with numerical integrations of Draine's model equations, and find a very close agreement between both models. From our analytic solution, we infer that radiation pressure creates significant central cavities in the nebula when the parameters of the system are such that $R_s \lesssim \sigma_d L_*/(8\pi ckT)$, being c the speed of light, k the Boltzmann constant, and $T \sim 10^4$ K the typical temperature of HII regions. Also, if the nebula is close to this configuration, the size reduction effect of dusty HII regions (found in previous models with dust absorption but not including radiation pressure) now disappears.

We extend the analysis of the spherical case to a planar distribution of radiation sources. This configuration is relevant to model star forming episodes in galactic disks, or in star formation triggered by cloud-cloud collisions. We obtain the vertical structure of the ISM around a plane distribution of stars through semi-analytic solu-

tions of model equations that also consider the stellar mass and the self-gravity of the gas. These solutions are hydrostatic profiles of a planar photoionised region in pressure balance with a covering neutral layer. This structure has different extensions (of the photoionised and neutral zones) according to the parameter configurations of the system. We evaluate the gravitational stability of the neutral layers of the solutions and find most of them in the stable regime. However, we find unstable cases where further star formation is triggered by the combined effects of self-gravity and radiation pressure.

In the last chapter of this thesis we developed a semi-analytic model for a SN blast wave that expands in the centre of a pre-existing cluster wind produced by the individual winds of the massive stars in the cluster. Our semi-analytic model gives the radius of the bubble of ejected material as well as the outer shock of the blast wave as a function of time. We find that blast waves produced by type II SNe are likely to begin the T-S phase outside the cluster radius. In this case the reverse shock of the SN remnant never goes back to the centre of the explosion and always expands behind the contact discontinuity.

We calculate the total X-ray luminosity of the resulting flow, and obtain for instance that in a cluster of 1000 O stars inside a radius of 2.5 pc, the blast wave increases the X-ray luminosity of the cluster wind by ~ 3 orders of magnitude. This increased luminosity decays over a period of $\sim$1000 yr to its undisturbed cluster wind value. The models of this chapter could be applied to interpret X-ray observations of massive star clusters.

The main contributions of this thesis can also be found in the papers by Rodríguez-Ramírez et al. (2014), Rodríguez-Ramírez & Raga (2016) and Rodríguez-Ramírez et al. (2016).

Contents

Chapter 1

Introduction

Stars influence the formation and evolution of astrophysical structures at several scales: planets, interstellar gas, star clusters, galaxies, etc. Stars also reveal the properties of "invisible" objects such as black holes and dark matter.

Nowadays it is understood that stars form in cosmic condensations of gas and dust, which eventually collapse due to gravity. This process is likely to occur collectively, resulting in bound or unbound stellar populations. However, some points in the scenario of star formation are not well understood. In particular, forming the massive stars (with masses > 20 $M_\odot$) is relatively difficult, since they are very few in comparison with low mass stars (e.g. solar type or smaller), which dominate by far the population of stellar systems.

The mass distribution in stellar populations follows what astronomers call the initial mass function (IMF). This is an empirical formula that gives the number of stars as a function their mass $\xi(M)$ and appears to hold at several cosmic scales. By considering the stellar field population in the Milky Way, Salpeter (1955) obtained the distribution:

$$\xi(M) = \xi_0 M^{-\alpha}, \tag{1.1}$$

with $\alpha = 2.35$. The factor ξ_0 is obtained by normalising the distribution with the total mass of a particular stellar population, with an upper and lower limit for the stellar masses. According to (1.1), the low mass stars are dominant in number and posses most of the total mass of their stellar population. For instance, for each O5 V star (with ~ 40 $M_\odot$) in a stellar population, the IMF predicts that there are ~ 6000 stars of solar type.

Although massive stars are a minority, they are the dominant source of energy and momentum deposition into the interstellar medium (ISM) in form of expanding ionised gas, radiation pressure, stellar winds, and supernova blast waves among others. This is what astrophysicists call *feedback* and believe that regulates the global star formation process. On one hand feedback stabilises the gas against its own gravitational collapse, disrupting molecular gas clouds and driving turbulence. On the other hand feedback also compresses interstellar matter driving further star formation.

In comparison with low mass stars, massive stars emit very large amount of ionising radiation. Then, after a massive star is formed, it quickly photoionises the cold surrounding medium, creating what is known as an HII region. HII regions are in many cases the first manifestation of the birth of massive stars. Therefore, their properties are useful to interpret the parameters of the newborn star, and the parental cloud and disk from which they are formed.

Massive stars also lose material from their atmospheres through supersonic stellar winds, which are likely to develop inside the photoionised region previously formed. These stellar winds are expected to affect the structure and evolution of HII regions if the wind gas remain confined inside the nebula (see Cappriotti & Kosminski 2001, Raga et al. 2012b). The lifetime of a massive star (much shorter than the lifetime of low mass stars) is likely to end as a SN explosion, and the resulting blast wave will evolve in an environment previously modified by the ionising radiation and the stellar wind of the massive star.

HII regions, stellar winds and SNe often show their presence in the form of interstellar *bubbles*, which are spherical structures of hot gas surrounded by a cold thin layer of swept up interstellar material. These stellar bubbles are produced by a single massive star or as a result of the feedback of many massive stars in OB associations or compact star clusters. The standard models of interstellar bubbles are (i) the wind-bubble model of Castor et al. (1975) (see also Weaver et al. 1977) appropriate for punctual stellar sources and (ii) the model of Chevalier & Clegg (1985) and Cantó et al. (2000) (see also Silich et al. 2004), appropriate for extended configurations of massive stars, as star clusters where the individual stars contribute to drive a collective "cluster wind".

However, the application of these models in recent years have presented sig-

nificant discrepancies with particular observations. For instance, the wind-bubble model of Castor et al. (1975) over-predicts the internal pressure, the expansion velocity and the X-ray emission in compact HII regions. To alleviate this over-estimations it has been suggested that the gas of the wind should escape through gaps and leaky structure in the bubbles (see e.g. Carral et al. 2002 and Harper-Clark & Murray 2009). On the other hand, the cluster wind model of Chevalier & Clegg (1985) under-predicts in some cases the X-ray luminosity in observed star clusters (see Stevens & Hartwell 2003 and Harper-Clark & Murray 2009), and SN blast waves that expand in the cluster wind have been suggested to enhance the theoretical X-ray luminosity (Chu & McLow 1990, Rodríguez-González et al. 2011).

1.1 This thesis

This thesis focuses on (i) the effect of radiation pressure in HII regions, and (ii) SN remnants that evolve in a well developed cluster wind. With this investigation we aim to provide alternative models that could alleviate some problems of the standard wind bubble models mentioned above.

We explore the effect of radiation pressure on HII regions with spherical as well as plane-parallel symmetry. The spherical models are relevant for HII regions powered by a single star (hypercompact, ultracompact, compact and classical HII regions) and the slab models are relevant in the context of extended star bursts in spiral galaxies, or in star formation triggered by cloud-cloud collisions. In these HII region models we neglect the effect of stellar winds. The stellar winds can be neglected if (i) the HII region is very young ($< 10^5$ yr) and therefore the stellar winds have not yet filled a substantial volume of the nebula, (ii) the ISM presents leaky or/and clumpy structure, (iii) the stellar winds are weak (found in HII regions with B-type stars). In the "leaky structure" case, the gas of the stellar wind escapes from the HII region (Harper-Clark & Murray 2009, Yeh & Matzner 2012 and Rosen et al. 2014), and therefore is not able to heat the inner part of the HII region. In this case the structure and expansion of the nebula is mainly determined by the radiation pressure of the starlight photons.

The models of supernova blast waves described in the last part of this thesis are in the context of young massive star clusters. Our contribution is then to study

the evolution of supernova blast waves in the wind environment and obtain the dependence of the resulting X-ray emission on the parameters of the cluster.

Along this thesis our approach is mainly analytic and semi-analytic. In this manner the resulting models for the discussed problems can easily be evaluated according to the configuration of the involved astrophysical parameters.

The content of this work is presented as follows. In Chapter 2 we introduce basic physical concepts in the context of the theory of star formation. We present the physics of gravitational instabilities for astrophysical fluids, and the physics of feedback mechanisms from massive stars. Chapter 3 presents an analytic treatment of radiation pressure in static, spherical HII regions, which is the same problem studied numerically by Draine (2011). The result of our analysis is a surprisingly simple approximate analytic solution for the relevant range of the involved astrophysical parameters. We then apply our solution to discuss some general properties of dusty nebulae. In Chapter 4 we extend the treatment of radiation pressure to planar geometry, where we also include the gravity of the stars and the self-gravity of the gas, and extend the analysis to the covering neutral layer. In this latter region we evaluate the gravitational stability, finding stable and unstable regimes. In Chapter 5 we present a semi-analytic model as well as spherical symmetric, gas dynamic simulations of supernova blast waves in star cluster outflows. The conclusions of this work are presented in Chapter 6.

At the end of the thesis we include three appendices. In Appendix A we describe the numerical algorithm used to solve the gas dynamic equations to obtain the SN blast waves models of Chapter 5. In Appendix B we present a simple analytic fit to the implicit exact solution of Cantó et al. (2000) for the star cluster wind (which is used in Chapter 5). In Appendix C we include a glossary of abbreviations and constants used in this thesis.

The content of Chapters 3, 4 and 5 can also be found in the papers by Rodríguez-Ramírez et al. (2016), Rodríguez-Ramírez & Raga (2016) and Rodríguez-Ramírez et al. (2014), respectively.

Chapter 2

Basic Concepts

2.1 Gas dynamics

A useful assumption for studying star formation processes is to consider that the interstellar matter behaves as a fluid. This is a suitable approximation when the mean free path of the particles of the interstellar material is very small in comparison with any length scale of interest. If the atoms or molecules exchange momentum and energy in many elastic collisions, their microscopic motions can be described by a Maxwell-Boltzmann distribution, and the kinetic degrees of freedom of the material are in local thermodynamic equilibrium.

Under this condition, the macroscopic description of the gas is given by the well known *Navier-Stokes equations*, which can be derived by calculating the "moments" of the *Boltzmann transport equation* (details can be seen in the books of F. Shu and A. R. Choudhuri).

In the astrophysical context, the fluid dynamics equations are usually applied with some modifications:

- Terms corresponding to viscosity and thermal conduction are neglected, since for astrophysical fluids the *Reynold's number* is huge. In this form, they are called the *Euler equations*.
- External forces due to gravity, radiation and magnetic fields are included.
- Heating and cooling functions due to atomic/ionic/molecular processes are included.

Also, the relativistic version of the fluid equations is widely applied. For the problems treated in this thesis, the relevant version of the hydrodynamic equations are

$$\partial_t \rho + \nabla \cdot (\rho \bar{v}) = 0, \tag{2.1}$$

$$\partial_t (\rho v_i) + \nabla \cdot (\rho v_i \bar{v}) + \partial_i P = \rho g_i + f_i, \tag{2.2}$$

$$\partial_t E + \nabla \cdot [(E + P)\, \bar{v}] = H - C + \left(\rho \bar{g} + \bar{f}\right) \cdot \bar{v}, \tag{2.3}$$

which represent the mass, momentum and energy conservation in the non-relativistic regime. In equation (2.3) $E = \frac{1}{2}\rho v^2 + P/(\gamma - 1)$ is the kinetic+thermal energy per unit volume, and $\gamma = C_P/C_V$ the specific heat ratio (usually $\gamma = 5/3$ for a monoatomic gas and $\gamma = 7/5$ for diatomic molecules with thermalised rotation states). Equation (2.2) represents three equations, each one labelled with the sub-index i which is associated with each spatial direction. $\bar{g}$ is the gravity field and is related to the gas density through Poisson's equation

$$\nabla \cdot \bar{g} = -4\pi G \rho. \tag{2.4}$$

$\bar{f}$ can represent other external forces such as radiation pressure, which should be complemented with equations describing the radiative transport. The heating and cooling functions H and C take into account absorption and emission of radiation and depend on the gas temperature T, density ρ and the ionisation and/or chemical state of the gas. The temperature can be obtained from the ideal gas equation of state:

$$P = \frac{k \rho T}{\mu m_H}, \tag{2.5}$$

where k is the Boltzmann constant, m_H is the mass of hydrogen and μ is the mean molecular weight ($\mu = 1.3$ for neutral gas with 90% H and 10% He).

Given the initial and boundary conditions of the system, equations (2.1)-(2.5) determine the time evolution of the density ρ, velocity field $\bar{v}$ and pressure P of the flow, which is obtained very often with numerical methods (see Appendix A), but also analytic solutions can be obtained for particular cases (e. g. for spherical symmetry or for the case of linear solutions). Modifications of equations (2.1)-(2.3)

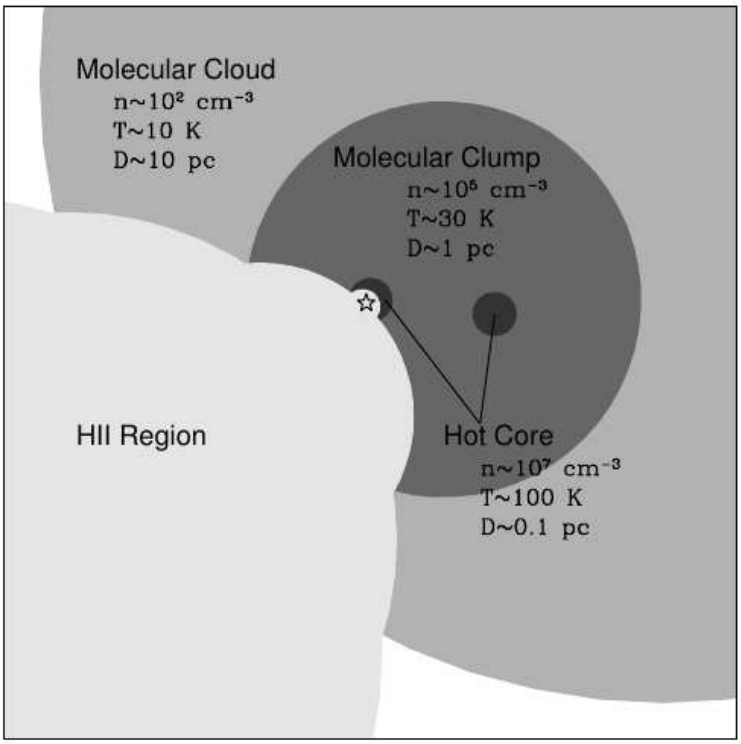

Figure 2.1: Schematic illustration of the levels of condensations in the theory of star formation, taken from (Kim & Koo 2001).

will be done throughout this text, according to the problem that we treat, e. g. including energy and mass loading terms, isothermal approximations or hydrostatic regimes.

2.2 Gravitational instability

Observations suggest that the precursors of massive stars are *hot cores* (Kurtz et al. 2000). These are condensations of gas with characteristic diameters of ~ 0.1 pc, and densities of $\sim 10^6$ cm^{-3} or greater. At the same time hot cores are substructures formed hierarchically as condensations of larger and less dense objects such as cold molecular clouds or *giant* molecular clouds. This is illustrated in Figure 2.1, taken from Kim & Koo (2001). Following this scenario, it is understood that giant molecular clouds provide the matter from which stellar systems are formed.

Nowadays the topics in the study of star formation can be identified as large scales (how clumps and cores are formed from molecular clouds, what is the efficiency of

star formation?) and small scales (accretion disks, jets, do massive stars form from collapsing cores or by merging binaries?, see the review of Mckee & Ostriker 2007).

For studying micro or macro processes of star formation, one of the basic mechanisms is *gravitational instability*. This is the idea that small perturbations in gaseous media, when self-gravity is taken into account, can evolve to create structures of very dense material. Depending on the scale, these structures can eventually collapse to form dense molecular clouds, stars or planets.

This can be shown by considering a medium in which pressure disturbances propagate isothermally. In this case, the density at a given position is related to the gas pressure as

$$P = c_s^2 \rho, \tag{2.6}$$

where $c_s = \sqrt{kT/m_H}$ is the isothermal sound speed in a medium composed of hydrogen, m_H is the mass of the hydrogen atom, and T is the gas temperature. Jeans (1902), who first discussed this idea formally, considered the hydrodynamic quantities of the gas as small oscillations, which we denote here with the prime symbol ($'$), around the values of the static state of the gas, which we will denote with the subindex 0. Thus, the density of the perturbed gas can be written as

$$\rho = \rho_0 + \rho', \tag{2.7}$$

with $|\rho'| \ll \rho_0$. The velocity field of the perturbed medium is $\bar{v} = \bar{v}'$ being the unperturbed medium static ($\bar{v}_0 = 0$). Analogously, the gravity field in the medium is $\bar{g} = \bar{g}_0 + \bar{g}'$, with $|\bar{g}'| \ll |\bar{g}_0|$, being $\bar{g}_0$ the gravitational field of the unperturbed medium. Jeans considered an infinite medium with uniform density, for which $\bar{g}_0 = 0$. However the analysis can also be done with non-homogeneous unperturbed media, as we will see later on.

To describe the small perturbations, the linearised version of equations (2.1), (2.2) and (2.6) apply, and one straightforwardly obtains a second order equation for the density fluctuations:

$$\partial_t^2 \rho' - c_s^2 \nabla^2 \rho' = \rho_0 4\pi G \rho', \tag{2.8}$$

which is a wave-like equation, with a non-homogeneous term due to gravity. Let us

now consider a generic wave mode of the form

$$\rho' = \widetilde{\rho} \exp\left\{-i(\bar{k} \cdot \bar{r} + \omega t)\right\}, \tag{2.9}$$

where i is the imaginary unity, $\bar{k}$ is the wave vector with real components, $\widetilde{\rho}$ and ω are the amplitude and oscillation frequency which are in general complex, and it is understood that physical oscillations are represented by the real part of equation (2.9).

Combining equations (2.8)-(2.9), one directly finds the dispersion relation

$$\omega^2 = 4\pi G\rho_0 - c_s^2|\bar{k}|^2, \tag{2.10}$$

with $|\bar{k}| = 2\pi/\lambda$, being λ the oscillation wavelength. If $c_s^2|\bar{k}|^2 < 4\pi G\rho_0$, ω is real and ρ' represents a standard harmonic motion. However, if $c_s^2|\bar{k}|^2 > 4\pi G\rho_0$, ω must take the form $\omega = i\omega_R$, where ω_R is a real number with both, positive and negative values satisfying the dispersion relation (2.10).

If we now look at equation (2.9), the sign of ω_R determines whether the oscillation mode decays or is amplified in time. This implies that any oscillation mode with wavelength

$$\lambda > c_s\sqrt{\frac{\pi}{\rho_0 G}} \equiv \lambda_J, \tag{2.11}$$

is able to create over-dense, unstable regions in the gaseous medium. This is the so-called *Jeans wavelength* for gravitational instability. The usual interpretation of inequality (2.11) is that the mass of any amount of matter with density ρ_0, speed of sound c_s, and dimensions larger than λ_J generates self-gravity that its gas pressure cannot balance, and therefore the gaseous object collapses.

The Jeans length depends on the mass density of the medium ρ_0 but also on its temperature through the speed of sound c_s. For this reason HII regions produce feedback that stops the collapsing process of a core of gas, since the radiation of the newborn star ionises and enhances the temperature of the surrounding material and then its Jeans length λ_J increases, leading the material to a stable regime.

For deriving equations (2.8)-(2.11) we considered an infinite medium with constant density ρ_0. For such a configuration the unperturbed gravitational acceleration $\bar{g}_0$ is null. However, this is not consistent with Poisson's equation (2.4), which is the

widely discussed "Jeans swindle". Later works have been done performing stability analyses (most of them numerically) over non-homogeneous configurations of the unperturbed state, e. g. on plane-parallel gaseous disks, stationary rotating disks, full numerical simulations of the gas dynamic equations of initially turbulent molecular clouds, etc. Surprisingly, they do not differ dramatically from Jeans's (1902) result.

The simplest stability analysis, consistent with Poisson's equation was done by Ledoux (1951), where the unperturbed static solution is an isothermal slab of gas (which models e. g. the vertical structure of a gaseous disk). In this case plane symmetry applies. Then, to obtain the static unperturbed state one just considers the z-component of the momentum and Poisson's equations (2.2) and (2.4), giving

$$\frac{\rho_0}{\rho_c} = \mathrm{sech}^2\left(\frac{1}{2}\frac{z}{z_{sl}}\right), \tag{2.12}$$

being ρ_c the value of the gas density at $z = 0$ and $z_{sl} \equiv c_s/\sqrt{8\pi G\rho_c}$ the characteristic length of the slab. We now consider plane waves with small amplitude, that propagate in the $x-$direction, i. e. perpendicular to the stratification of the static state. These oscillation modes can be written as

$$\begin{pmatrix} \bar{v} \\ \rho \\ \Phi \end{pmatrix} = \begin{pmatrix} 0 \\ \rho_0(z) \\ \Phi_0(z) \end{pmatrix} + \begin{pmatrix} [v_x(z), 0, v_z(z)] \\ \rho_1(z) \\ \Phi_1(z) \end{pmatrix} \times \exp\left\{-i(\omega t + k_x x)\right\} \tag{2.13}$$

where $\bar{g} = -\nabla\Phi$. To find the critical wavelength of these oscillation modes, one introduces equation (2.13) into equations (2.1), (2.2) and (2.6), keeps only first order terms for the amplitudes v_{x1}, v_{z1}, ρ_1 and Φ_1 and assumes that the exchange of stability occurs at $\omega = 0$ (as occurs in the analysis for the constant ρ_0 case, see equation 2.10). Following this procedure, one directly obtains an equation for the critical wave number, which is related to the amplitude of the density fluctuations as the eigenvalue problem:

$$\frac{d^2}{dz^2}\left(\frac{\rho_1}{\rho_0}\right) + \left(\frac{4\pi G}{c_s^2}\rho_0(z) - k_{cr}^2\right)\frac{\rho_1}{\rho_0} = 0, \tag{2.14}$$

where $\rho_0(z)$ is the unperturbed state given by the stratification (2.12). Consider

now the eigenfunctions of equation (2.14), symmetric with respect to $z = 0$:

$$\frac{\rho_1}{\rho_0} = (\nu - \chi)\left(\frac{1+\chi}{1-\chi}\right)^{\nu/2} + (\nu + \chi)\left(\frac{1-\chi}{1+\chi}\right)^{\nu/2}, \tag{2.15}$$

with

$$\chi \equiv \tanh\left(\frac{z}{2z_{sl}}\right), \qquad \nu \equiv \frac{k_{cr}c_s}{\sqrt{2\pi G\rho_c}}. \tag{2.16}$$

The amplitude ρ_1 should not diverge as $z \to \infty$, which implies that $\nu = 1$, giving the critical wavelength

$$\lambda_{cr} = c_s\sqrt{\frac{2\pi}{G\rho_c}} = \sqrt{2}\lambda_J, \tag{2.17}$$

which is very close to the Jeans wavelength (2.11). The interpretation of the fact that λ_{cr} is larger that λ_J is that a larger volume of the slab is needed to compensate for the density decay of the slab profile (2.12).

In Chapter 5 we study the effect of self-gravity and radiation pressure on the ISM surrounding a planar star burst. For some configurations we obtain density profiles of models with a photoionized slab covered by a dense and narrow neutral layer. On this latter layer, we apply equation (2.17) to evaluate the gravitational stability.

2.3 Feedback

During their formation, life-time and death, massive stars release energy and momentum which interacts with the surrounding ISM. This is what astrophysicist call *feedback*, which takes the form of jets, stellar winds, expanding HII regions, radiation pressure and supernova blast waves. Feedback is an important element in the star formation theory since

- the energy and momentum expulsion stabilise the gas in molecular clouds against its own gravitational collapse, thereby reducing the global star formation efficiency (McKee & Ostriker 1977; Adams & Fatuzzo 1996).

- Feedback from massive stars are indicators to localise star forming regions. Due to the fact that massive stars are few and have short life-times, their

presence implies regions of ongoing star formation, where smaller stars with larger life-times are also being created.

The interaction of SF feedback with the ISM is observed in X-rays (gas heated by SN remnants and stellar winds), optical (recombination lines of H, e. g. in HII regions), the infrared (reprocessed radiation by dust absorption) and radio (bremsstrahlung and synchrotron radiation). On the theoretical side, feedback is modelled with non-relativistic and relativistic hydrodynamics, magneto-hydrodynamics and radiative transfer, with numerical and analytic calculations.

In the next subsections we briefly introduce some of the basic physics of HII regions (which are the first manifestation of the birth of a massive star), SN blast waves (which indicate the end of the lifetime of massive stars) and radiation pressure (which is an important mechanism of momentum deposition in the ISM).

2.3.1 HII regions

Photoionised regions are always associated with the presence of massive stars, since these stars emit radiation capable of ionising hydrogen. These regions around massive stars are commonly known as HII regions. In a photoionised medium, electrons and positively charged particles coexist. Therefore, the electrons' trajectories are deflected by protons and positive ions, and thus HII regions emit *bremsstrahlung* radiation.

Since massive stars release ionising radiation, matter in HII regions is continuously photoionised and recombined. The recombinations depend on the cross sections of the capturing particles, being protons the dominant ions. Once an electron is captured by a positive particle, it undergoes bound transitions before arriving at the ground state. Thus, HII regions are also associated with emission of atomic transitions, being the hydrogen 6563 Å and 4861 Å lines some of the most prominent, which correspond to $3 \rightarrow 2$ (H_α), and $4 \rightarrow 2$ (H_β) transitions of hydrogen levels.

Much less abundant than hydrogen, other elements as nitrogen (N), oxygen (O), sulphur (S) and their ions are also detected through their characteristic line emissions due to collisional excitations by free photo-electrons. The photons emitted by these species have very low probability of being absorbed by gas and dust. Therefore, the

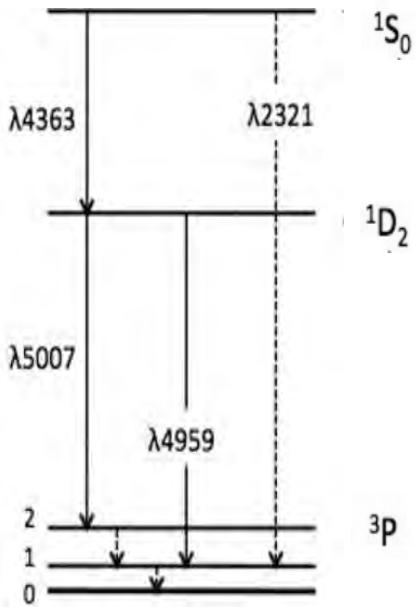

Figure 2.2: Line emissions due to electronic transitions of OIII (doubly ionised oxygen).

emission of O, N and S is very useful to measure the temperature T_e and density n_e of electrons within HII regions.

For instance, consider electronic transitions of the OIII ion (doubly ionised oxygen, or O^{++}) shown in Figure 2.2. In spectroscopic notation, ${}^3P_0$,${}^3P_1$,${}^3P_2$ comprise the ground state triplet and ${}^1D_2$ and ${}^1S_0$ the exited states. In particular, the intensity of the 4363 Å line, produced in ${}^1S_0 \rightarrow {}^1D_2$ transitions, depends on the number density $n_{^3P}$ of OIII ions in the ground state, the number density of electrons n_e and the electronic temperature T_e as

$$I(4363) \propto \left[\frac{n_e}{T_e^{1/2}} \exp\left\{-\frac{h\nu(4363)}{kT_e}\right\} n_{^3P} \Omega({}^3P,\ {}^1S)\right] \left[h\nu(4363)\frac{A_{^1S,^1D}}{A_{^1S,^1D} + A_{^1S,^3P}}\right]. \tag{2.18}$$

The factors in the first brackets take into account the rate of collisional exitations of the ${}^1S_0$ state, where $\Omega({}^3P,\ {}^1S_0)$ is its quantum mechanical collision strength. The factors in the second brackets take into account the emission in the ${}^1S_0 \rightarrow {}^1D_2$ transition, where the $A_{i,j}$ numbers are the Einstein coefficients of spontaneous decay.

Analogously, the intensity of the 5007 and 4959 Å lines corresponding to the ${}^1D_2 \rightarrow {}^3P_2$ and ${}^1D_2 \rightarrow {}^3P_1$ transitions respectively (see Figure 2.2), depend on the

$n_{^3P}$, n_e and T_e parameters of the nebula. However, the ratio of line intensities

$$\frac{I(5007)+I(4959)}{I(4363)} = \frac{\Omega(^3P,^1D)}{\Omega(3^P,^1S)}\frac{A_{^1S,^1D}+A_{^1S,^3P}}{A_{^1S,^1D}}\frac{\bar{\nu}(^3P,^1D)}{\nu(^1S,^1D)}\exp\left\{\frac{\Delta E}{kT_e}\right\}, \quad (2.19)$$

where

$$\bar{\nu}(^1D,^3P_2) = \frac{\nu(^1D,^3P_2)A_{^1D,^3P_2}+\nu(^1D,^3P_1)A_{^1D,^3P_1}}{A_{^1D,^3P_2}+A_{^1D,^3P_1}}, \quad (2.20)$$

only depends on the electron temperature T_e of the plasma. Therefore, if the intensity of the 4363, 4959 and 5007 Å lines are known (by spectroscopic observations), the electronic temperature T_e of an HII region can be measured. The intensity line ratio given by equation (2.19) is valid for electron number densities $n_e < 10^5$. For nebulae with higher densities (as ultra and hyper compact HII regions), the electrons also contribute to "de-excite" the $^1D_2$ state, and the line ratio (2.19) will also depend on the electron number density n_e (see e.g. the book of Osterbrock & Ferland 2006).

It turns out that HII regions from ultracompact to giant have temperatures of $\sim 10^4$ K. For these temperatures, the ionised gas can be considered as isothermal and we will assume this condition in the models of HII regions discussed along this thesis.

Now, consider the simplified case of a point-like, isotropic source of ionising radiation, surrounded by a uniform environment composed of hydrogen and dust. Setting a spherical coordinate system with the origin at the ionising source, the beams of radiation undergo absorption by hydrogen atoms and dust particles, along their paths on the radial coordinate R.

Then, the *specific intensity* I_ν of the beams at the radius R, defined as $dE = I_\nu dt d\nu d\Omega dA$ (energy per unit time, frequency, solid angle, and area), being E the energy of the central source of ionising photons, is described by the radiative transfer equation

$$\frac{dI_\nu}{dR} = -\kappa_\nu I_\nu + j_\nu, \quad (2.21)$$

where j_ν is the emission coefficient, and

$$\kappa_\nu = \sigma_\nu n_{HI} + \sigma_d n, \quad (2.22)$$

is the absorption coefficient. The absorption coefficient gives the attenuation of the

beam due to photoionisation of H and dust absorption. In equation (2.22), σ_ν is the photoionisation cross section of the H atoms, n_{HI} is the number density of neutral H atoms, σ_d is the cross section of dust grains per H nucleon, and n is the total number density of H (ions+neutral hydrogen). Assuming that neutral H atoms are photoionised from their ground states, the photoionisation cross section is given by

$$\sigma_\nu \simeq 7.9 \times 10^{-18} \left(\frac{\nu_H}{\nu}\right)^3 g(\nu) \simeq 6.3 \times 10^{-18} \mathrm{cm}^2, \tag{2.23}$$

where $g(\nu) \sim 0.9$ is the quantum *Gaunt factor* for ν close to the Lymann frequency ν_H. $\sigma_d \sim 10^{-21}$ cm^2 H^{-1} is the typical cross section of dust grains per H nucleon in neutral ISM. According to Draine (2011), the value of σ_d is likely to be reduced inside HII regions.

The emission coefficient j_ν should include the contribution of of photons emitted in recombinations of H with enough energy to ionise other H atoms as well as non-ionising cooling radiation. In the following we will neglect the "diffuse" j_ν coefficient in equation (2.21), by assuming that recombination and cooling radiation escape freely.

Putting $j_\nu = 0$ in equation (2.21), the specific intensity is

$$I_\nu(R) = I_\nu(0) \exp\left\{-\int_0^R \kappa_\nu dR'\right\}, \tag{2.24}$$

and the flux F_i of ionised photons (ionising photons per unit time per unit area) at a radius R inside the nebula can be approximately obtained as

$$\begin{aligned} F_i = \int_{\nu_H}^\infty \frac{1}{h\nu} \oint I_\nu d\Omega d\nu &= \int_{\nu_H}^\infty \frac{L_\nu}{h\nu 4\pi R^2} \exp\left\{-\int_0^R \kappa_\nu dR'\right\} d\nu \\ &= \frac{S_*}{4\pi R^2} \exp\left\{-\int_0^R \kappa_\nu dR'\right\}, \end{aligned} \tag{2.25}$$

where L_ν is the luminosity per unit frequency of the central star, $h\nu_H = 13.6$ eV is the ground state binding energy of the H atom and $S_* = \int_{\nu_H}^\infty L_\nu/(h\nu) d\nu$ is the rate of ionising photons of the star. In the last equality of (2.25), we have applied the *grey approximation* of the ISM, in which one takes a constant average value of the photoionisation and dust absorption cross sections. In this way the factor involving the absorption coefficient κ_ν (see equation 2.22), is taken out of the frequency

integral. This approximation is accurate where the density of neutral H atoms is very short in comparison to the density of ionised H, and therefore the the nebula is optically thin to the flux of ionising photons. Close to the ionisation front, the nebula is optically thick and the number of the available ionising photons rises with ν. However, this optically thick zone occupies a small, outer volume of the nebula (see e.g. Raga & Lora 2015), and the grey approximation is appropriate at most radii.

The basic assumption of the photoionisation-equilibrium model for HII regions is to consider the balance between the rate of photoionisations and recombinations in every volume element of the nebula. For the problem of the central source of ionising photons, this condition depends only on the radial coordinate R and can be written as

$$\alpha_B(T) n_e n_{HII} = F_i \sigma_H n_{HI}, \tag{2.26}$$

where in the RHS of equation (2.26) F_i the impinging flux of ionising photons given by equation (2.25), and σ_H the constant average of the photoionisation cross section (considering the grey approximation as we mention above). The LHS of equation (2.26) is the rate of recombinations being n_e the number density of electrons, n_{HII} the number density of protons, and $\alpha_B(T)$ is the "case B" recombination coefficient which basically depends on the temperature T of the nebula (which typically is uniform along the nebula extent). The $\alpha_B(T)$ coefficient is calculated as

$$\alpha_B = \sum_{n=2}^{\infty} \alpha_n, \tag{2.27}$$

where each α_n is the recombination coefficient to the n energy level of H given by

$$\alpha_n = \int_0^{\infty} \sigma_n(v) v f(v,T) dv, \tag{2.28}$$

with $f(v,T)$ the Maxwell-Boltzmann distribution, and $\sigma_n(v)$ is the effective cross section of the radiative recombination process, which is related to the photoionisation cross section through *Milne's relation*.

Note that the case B recombination coefficient does not consider the $n = 1$ transition. In this way, the fact of neglecting the j_ν coefficient in equations equation (2.21), is partially justified.

Equation (2.26) can be applied to find the size of the HII region as follows. Consider the available ionising photons per unit second S inside the nebula, which is S_* at the source and zero at the boundary radius R_S. Then, the gradient of S is given by

$$\frac{dS}{dR} = -4\pi R^2 F_i \kappa, \tag{2.29}$$

where the RHS is the absorption of ionising photons in a shell of radius R. Then, using equations (2.25) and (2.26) we obtain

$$\frac{dS}{dR} = -4\pi \alpha_B R^2 n_e n_{HII} - n\sigma_d S. \tag{2.30}$$

Consider now that the transition from the ionised region to the fully neutral zone takes place in a very thin region. In this idealised situation the internal gas is fully ionised and then $n_e = n_{HII} = n$. Furthermore, assuming a uniform density n in the nebula, the solution of equation (2.30) is

$$S = \exp\{-n\sigma_d R\} \left(S_* - 4\pi \alpha_B n^2 \int_0^R R'^2 \exp\{n\sigma_d R'\}\, dR' \right), \tag{2.31}$$

and the condition that $S(R_s) = 0$ implies that

$$S_* = 4\pi \alpha_B n^2 \int_0^{R_s} R^2 \exp\{n\sigma_d R\}\, dR. \tag{2.32}$$

From this equation, one can obtain the external radius R_s of a dusty nebula with uniform density, by giving fixed values of S_*, n and σ_d. For the dustless case, i.e. for $\sigma_d = 0$, the the solution of equation (2.32) for the external radius is

$$R_{s,0} = \left(\frac{3S_*}{4\pi \alpha_B n^2} \right)^{1/3}, \tag{2.33}$$

which is the so-called Strömgren radius of a dustless photoionised sphere.

We can see from the integral in equation (2.32), that the size of dusty nebula, is smaller than the size of a dustless one. This result has been discussed by Petrosian (1972), Franco et al. (1990) and Raga & Lora (2015). However, if we take into account *radiation pressure* due to the absorption of dust grains and photoionisation of H, the reduction effect in dusty nebulae disappear, for certain configurations of

the parameters of the system. We will discuss this effect in Chapter 3.

2.3.2 Supernova remnants

A Supernova Remnant (SNR) is an extended structure of gas, which results from the explosion of a star, when it reaches the end of its life. This occurs, as far as we know, when a star with mass $M \geq 7M_{\odot}$ cannot release enough mass during its lifetime, such that it ends above the Chandrasekhar mass limit (1.4 $M_{\odot}$). Therefore, the star collapses due to gravity when its nuclear fuel is exhausted. As a result of the collapse, a huge amount of energy (typically $\sim 10^{51}$ erg) is released into the surrounding medium.

This explosion produces a blast wave, sweeping up the ISM through a hydrodynamic shock. The simplest model of the blast wave, is a sphere of hot gas expanding into an ambient medium with a uniform density ρ_e. Behind the shocked material a *contact discontinuity* is formed, which is the interface between the shocked material and the ejected material. The evolution of the remnant undergoes generally (i) an initial free expansion phase, followed by (ii) the so-called *Taylor-Sedov phase* (T-S phase), followed eventually by (iii) the radiative phase.

In the free phase the mass and pressure of the expelled material are much larger than the mass and pressure of the swept-up environment, which therefore has no influence on the expansion of the ejected material. Thus, the radius of the contact discontinuity R_c expands linearly with time as $R_c = v_{sn}t$, where v_{sn} is the initial ejecta velocity which can be estimated as $v_{sn} = \sqrt{10\alpha E/(3M_{sn})}$ (see Section 5.1), where α is the fraction in the form of kinetic energy of the total explosion energy (the complement is thermal energy).

The T-S phase begins when eventually the swept-up material is massive enough to slow down the expansion of the ejecta. Conventionally, this phase begins when $M_{sn} = 4\pi\rho_e R_{ST}^3/3$, i.e., when the swept-up environment material equals the ejected material at the radius R_{ST}.

In a medium with uniform density, after the T-S phase, the ejected material piles up behind the contact discontinuity (since the expansion of this interface is being slowed down by the ambient material) and at the same time the pressure of the expanding ejecta drops. This pressure gradient drives a *reverse shock* back to centre of the explosion (a study of the forward and reverse shocks can be found

in Truelove & MacKee 1999). This rise significantly the temperature of the ejecta, which becomes a *hot bubble* with approximately uniform pressure and from this moment onwards, the expansion of the SNR is determined by the thermal pressure of the bubble.

Due to the typical temperatures of the T-S phase, the energy dissipation due to radiation is negligible in comparison with the explosion energy. Under these conditions the hot bubble expands adiabatically.

The standard and widely used model of the T-S expansion is the thin layer approximation of the expansive blast wave (see Taylor 1950, Sedov 1959, Chernyi 1957, Zel'dovich & Raizer 1967 and the review by Bisnovatyi-Kogan & Silich 1995). However this approximation eventually breaks down when the external shock is no longer in the strong regime (see e. g. Tang & Wang 2005).

An improved model is given by Raga et al. (2012c) who introduce a *thick shell formalism* and derive an analytic solution for the blast wave evolution. This solution is appropriate for the T-S phase and allows a strong/weak transition for the outer shock. The analytic solution gives evolved time t and the radius of the outer shock R_S parametrised by the radius of the hot bubble R as

$$\frac{R_S}{R_f} = -\left(\frac{\gamma-1}{2}\right)\left(\frac{R}{R_f}\right) + \frac{\gamma}{\sqrt{3}}\text{atan}\left(\frac{\sqrt{3}R/R_f}{2+R/R_f}\right) + \frac{\gamma}{6}\log\left[\frac{1+R/R_f+(R/R_f)^2}{(1-R/R_f)^2}\right], \tag{2.34}$$

$$t = \frac{R_f}{c_0\gamma^{1/3}}\left(\frac{\gamma+1}{2}\right)^{4/3}\frac{2}{5}r^{5/2} \times F_1\left(\frac{5}{6},-\frac{1}{2},1,\frac{11}{6},-\left(\frac{\gamma-1}{2\gamma}\right)r^3,\left(1-\frac{\gamma-1}{2\gamma}\right)r^3\right) \tag{2.35}$$

where F_1 is the Appell hyper-geometric function of two variables,

$$r \equiv \left(\frac{2\gamma}{\gamma+1}\right)\frac{R}{R_f},\;\; R_f \equiv \left(\frac{\gamma E}{\Gamma\rho_e c_0^2}\right),\;\; \Gamma \equiv \frac{8\pi}{3}\frac{\gamma}{\gamma^2-1}, \tag{2.36}$$

being R_f the final radius to which the hot bubble converges and c_0 is the adiabatic sound speed of the environment. This model recovers as a particular case, the classic self-similar T-S solution, in the $R << R_f$ limit of equations (2.34)-(2.35) (see Raga et al 2012 c).

The analytic solution given by equations (2.34)-(2.35) is plotted with black lines in Figure 2.2, taken from Raga et al. (2012 c). This is compared with the classical Taylor-Sedov solution (the strong shock, thin shell model), in white lines. A spherically symmetric gas dynamic simulation of the same problem is also included. The top graph shows the pressure stratification obtained from the simulation together with the analytic solutions for the outer shock of the blast wave. The bottom graph shows the temperature stratification of the simulation together with the analytic solutions for the hot bubble radius. In the top graph it can be seen that the strong/weak transition for the outer shock takes place when the white curve deviates from the black one, which follows very well the numerical simulation.

In the context of star forming regions, Type II supernovae are likely to occur (with ejected mass of $\sim 5M_{\odot}$ see Pérez-Rendón et al. 2009) in preexisting photoionised environments (HII regions) or collective winds produced by neighbouring massive stars. In this context the *thick shell* formalism of Raga (2012c) can be modified to include a non-uniform environment in which the blast wave evolves. Observations of X-ray emission from this dense stellar clusters have been compared with theoretical models of cluster winds. In some cases the models produce lower temperatures or underestimate the observed X-ray emission (Chu & Mac Low 1990, Stevens & Hartwell 2003) and supernovae events have been proposed to explain these discrepancies.

To model a SN blast wave in this context, the collective the wind model of Cantó et al. (2000) is appropriate to describe the pre-existent environment. This is a spherical, stationary model which considers a continuous and uniform distribution of mass loading sources, representing the stellar winds of the stars in a cluster. This model gives an analytic solution for the velocity field and the density of the outflow, given by

$$u_e \left[1 + \frac{5\gamma + 1}{\gamma - 1} u_e^2\right]^{-(3\gamma+1)/(5\gamma+1)} = A_\gamma r, \tag{2.37}$$

for the wind velocity inside the cluster, and

$$u_e (1 - u_e^2)^{1/(\gamma-1)} = \frac{B_\gamma}{r^2}, \tag{2.38}$$

for the wind velocity outside the cluster, A_γ and B_γ are two constants which depend

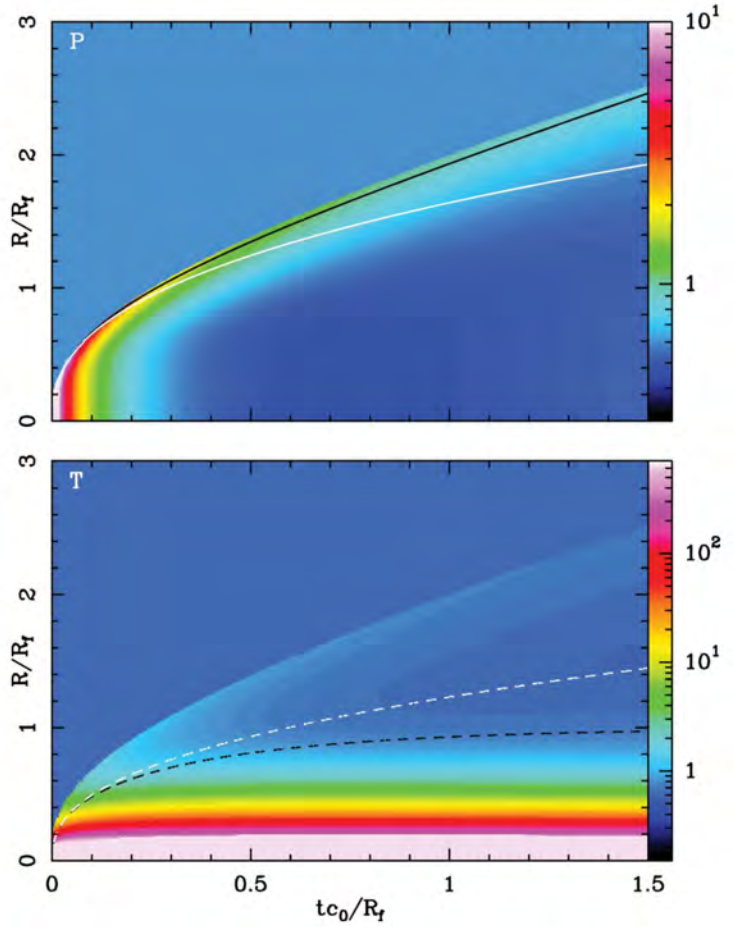

Figure 2.3: Pressure (upper panel) and temperature (bottom panel) stratifications of a spherical simulation of a blast wave evolved in a initially uniform environment, taken from Raga et al. (2012, c). In the upper panel the black curve is the analytic solution for the outer shock of the blast wave with strong-weak transition (see equations 2.34-2.35) and the the white curve is the corresponding strong shock approximation. Analogously, in the bottom panel it is shown the analytic models for the hot bubble radius.

on the specific heat ratio $\gamma = c_p/c_v$:

$$A_\gamma = \left(\frac{\gamma-1}{\gamma+1}\right)^{1/2} \left(\frac{\gamma+1}{6\gamma+2}\right)^{(3\gamma+1)/(5\gamma+1)}, \tag{2.39}$$

$$B_\gamma = \left(\frac{\gamma-1}{\gamma+1}\right)^{1/2} \left(\frac{2}{\gamma+1}\right)^{1/(\gamma-1)}, \tag{2.40}$$

where r is the radius in units of the cluster radius R_c, and u_e the flow velocity in units of the terminal wind velocity v_w of a single star. According to this model, the density profile ρ_e of the outflow is given in terms of the velocity field as

$$\frac{\rho_e}{\rho_c} = \begin{cases} A_\gamma r/u_e & \text{for } r < 1, \\ A_\gamma/\left(r^2 u_e\right) & \text{for } r > 1\,. \end{cases} \tag{2.41}$$

where ρ_c is the central density of the outflow given by

$$\rho_c = \frac{N\dot{M}_w}{4\pi A_\gamma R_c^2 v_w}. \tag{2.42}$$

Figure 2.3 shows these solutions with thin grey curves, which are compared with a 3-D gas dynamic simulation with 30 "discrete" massive stars (see details in Cantó et al. 2000), shown with the thick black curves. Naturally, the analytic solution is more accurate if the number of massive stars in the cluster is larger.

In Chapter 5 we study a Type II supernova blast wave that goes off in the centre of a star cluster of massive stars. To do this we modify the "thick shell" formalism of Raga et al (2012c), to obtain the evolution of the expanding blast wave that sweeps up the material of a pre-existent cluster wind described by equations (2.37)-(2.42) (the model of Cantó et al. 2000). We obtain a semi-analytic model for the blast wave evolution which we compare with numerical simulations of the spherically symmetric version of the gas dynamic equations (2.1)-(2.3). Also in Chapter 5 we apply our models to calculate the predicted X-ray luminosity of the flow as a function of time, and obtain its dependence on the outer radius and the number of stars of the cluster.

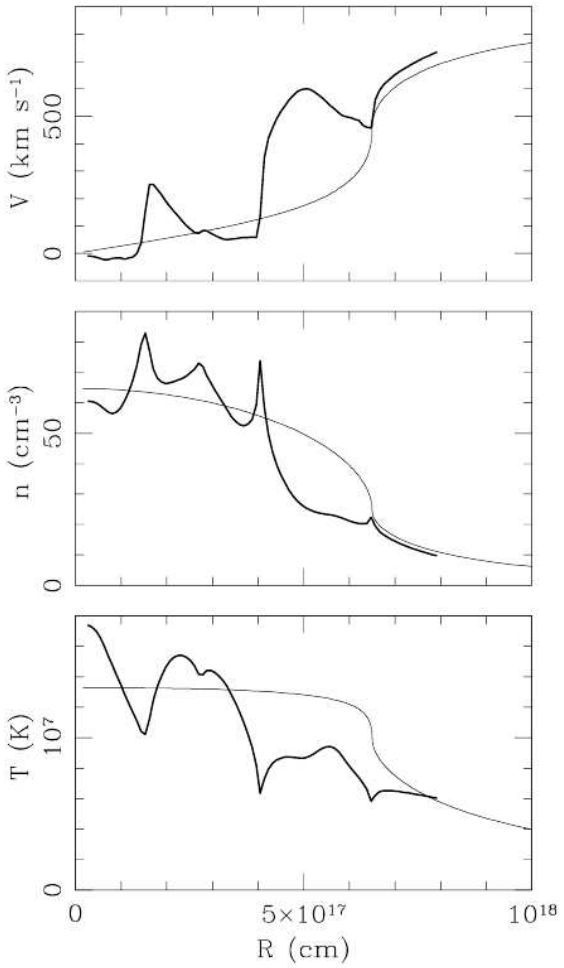

Figure 2.4: Plots of the analytical solution (thin-grey lines) and numerical simulation (thick-black lines) taken from Cantó et al. (2000), which gives the velocity (top), density (centre) and temperature (bottom) as function of the spherical radius of a stationary cluster outflow.

2.3.3 Radiation pressure

The transfer of momentum from the photon field to matter is known as *radiation pressure* and is one of the basic processes in astrophysics. This concept has been applied to explain the acceleration of gas in stellar winds from massive stars and more recently, to explain large-scale winds driven by galaxies.

In the "small scale" case, the mass outflow occurs when the radiation field coming from the nucleus, impacts the stellar atmosphere, accelerating the hot material due to *Thompson scattering* (or to more complex line absorption processes). An outwards acceleration of gas takes place when the radiation pressure force overcomes the inwards gravitational force. The standard criterion to evaluate this process is the *Eddington Luminosity*:

$$L_{Edd} = \frac{4\pi G M m_p c}{\sigma_T}, \tag{2.43}$$

with m_p the proton mass and σ_T the cross section of electrons for Thompson scattering.

In larger scales, *galaxy winds* are explained by the expansion of the ISM heated by the collective contribution of multiple supernovae together with stellar winds of massive stars in clusters or star forming regions (Larson 1974, Chevalier & Clegg 1985, Dekel & Silk 1986). These models apply for hot X-ray emitting galactic winds. However, observations also reveal cold molecular gas in these outflows (see e.g. Walter et al. 2002 and Veilleux et al. 2009).

Cold outflows are better explained by considering a wind-driving mechanism based on the absorption of photons from the galaxy by dust grains. The grains are found to be dynamically coupled to the gas and then the momentum absorbed by grains results in the production of a global outflow (Murray et al. 2005). Also, absorption by dust is capable of expelling gas of early times before multiple SNe occur in a star forming region. Thus, radiation pressure on dust is a significant component of feedback (in addition to SNe and stellar winds) for driving galactic winds, as suggested by Thompson et al. (2005) and Murray et al. (2010).

In the context of HII regions, the presence of dust inside the nebula has been observed through the reprocessed radiation by dust, as IR emission (see Natta & Panagia 1976, Kraemer et al. 2001, Dopita et al. 2003). Absorption of ionising radiation by dust has been considered in models of HII regions by Petrosian (1972),

Franco et al. (1990) and Raga & Lora (2015). These models do not consider the momentum of photons transferred to the grains of dust, and describe nebulae with uniform densities (see section 2.1), with a reduced size due to dust absorption.

However, taking into account the momentum transferred to dust and assuming a strong dust-gas coupling, the density structure of the nebula is substantially modified. Draine (2011) study the effects of radiation pressure on static HII regions, and calculates numerical models in which the force on dust grains creates central cavities in the nebulae. Also, Matzner & Krumholz (2009) develop an analytic model of expanding HII regions, driven by the photons trapped by dust in the external shell, together with the gas pressure of the inner HII region. They find a regime in which the expansion is determined by the radiation pressure component.

The injected momentum associated to dust absorption, in a volume element of gas at a radius R inside a spherical HII region can be computed as

$$f_d(R) = \int_0^\infty \frac{L_\nu}{h\nu 4\pi R^2} \exp\left\{-\int_0^R \kappa' dR'\right\} \sigma_d n \frac{h\nu}{c} d\nu, \tag{2.44}$$

where the factor multiplying the $h\nu/c$ term in the integral is the rate of photon absorption by dust grains per unit frequency. Stellar photons with frequencies $\nu > \nu_H$ are also absorbed by H atoms, which is included the absorption coefficient $\kappa = \sigma_d n + \sigma_\nu n_{HI}$ (see section 2.1). Thus the frequency integral in equation (2.44) can be split in two components:

$$f_d(R) = \frac{n}{4\pi c R^2} \left[\int_0^{\nu_H} L_\nu \exp\left\{-\int_0^R \sigma_d n' dR'\right\} \sigma_d d\nu \right. \tag{2.45}$$

$$\left. + \int_{\nu_H}^\infty L_\nu \exp\left\{-\int_0^R \kappa' dR'\right\} \sigma_d d\nu \right]. \tag{2.46}$$

Since the photoionization and dust cross sections do not depend strongly on the photons frequency in comparison with the luminosity spectrum L_ν, we take the factors involving σ_d and σ_ν out of the frequency integrals, giving

$$f_d(R) = \frac{\sigma_d n}{4\pi c R^2} \left[L_n \exp\left\{-\tau_d\right\} + L_i \exp\left\{-\tau_d - \tau_H\right\}\right] \tag{2.47}$$

where

$$\tau_d = \int_0^R \sigma_d n' dR', \quad \tau_H = \int_0^R \sigma_\nu n'_{HI} dR' \tag{2.48}$$

are the dust absorption and photoionisation optical depths, and $L_n = \int_0^{\nu_H} L_\nu d\nu$ and $L_i = \int_{\nu_H}^{\infty} L_\nu d\nu$ are the non-ionising and ionising components of the total stellar luminosity L_*, i. e., $L_n + L_i = L_*$.

The photoionisation absorption coefficient depends on the number density of neutral H n_{HI} in the nebula, as we can see in equation (2.48). However, from section 2.1 we can straightforwardly note that the attenuation factor $\mathrm{e}^{-\tau_d - \tau_H} = S/S*$ of the ionising luminosity follows the differential equation

$$\frac{d(S/S_*)}{dR} = -\frac{4\pi\alpha_B}{S_*} R^2 n^2 - \sigma_d n (S/S_*), \tag{2.49}$$

which is given in terms of the total number density n and the radial coordinate R.

To derive the radiation pressure force in equation (2.47), we assumed that the momentum absorbed by dust grains, is directly transmitted to the gas through the absorption cross section σ_d. However, this coupling depends on the conditions of the gas, the grains, and the radiation field.

Consider the idealised case in which a dust grain is a sphere of radius a. Then, at a distance R from the star, the grain receives a radiation force $\pi a^2 L(r)/(4\pi c R^2)$ where $L(R) < L_*$ is the stellar luminosity at a radius R. On the other hand, the gas atoms and ions of the ISM apply a *drag force* F_d on the grain, opposed to the motion. This drag force occurs due to direct collisions and Coulomb interactions between the moving dust grain and the gas particles. Ignoring other interactions (such as gravitational and magnetic forces), the equation of motion for the dust grain can be written as

$$\frac{d}{dt}(m_d v_d) = \pi a^2 \frac{L(R)}{4\pi c R^2} - F_d, \tag{2.50}$$

where m_d and v_d are the mass and velocity of the grain. According to Draine & Salpeter (1979), and Draine (2011), the drag force in the ionised gas can be approximated as:

$$F_d = \pi a^2 2nkT \left[G_1(s) + G_2(s)\right], \tag{2.51}$$

where

$$s = \frac{v_d}{\sqrt{2kT/m_H}}, \tag{2.52}$$

and v_d is the relative velocity between the dust and the gas, called the "drift velocity". The function

$$G_1(s) = 1.5s\left(1 + \frac{9\pi}{64}s^2\right)^{1/2}, \tag{2.53}$$

takes into account the collisional drag, and the function

$$G_2(s) = \frac{69.5s}{1 + \frac{4}{3\sqrt{\pi}}s^3}, \tag{2.54}$$

is the contribution of the Coulomb drag, due to the interaction of a charged dust grain and the ions in the HII region.

When a dust grain reaches the terminal velocity (in a time of $\sim 10^2$ yr, see Draine 2011), the absorbed radiation is completely transmitted to the gas through the drag force. For the dusty HII regions discussed in this subsection, dust grains can be considered strongly coupled to the gas if the time in which they arrive at the external boundary R_s, is larger than the life-time of the HII region. This crossing time can be estimated as

$$t_d = \frac{R_s - R}{v_d}, \tag{2.55}$$

where R is the radius at which the dust grain absorbs the radiation.

The drift velocity v_d at a radius R can be obtained by balancing the RHS of equation (2.50) (when the grain has terminal velocity). In this case one has to solve the equation

$$\frac{L(R)}{8\pi ckTn(R)R^2} = G_1(s) + G_2(s), \tag{2.56}$$

for s.

On the other hand, since HII regions are being continuously photoionised, the absorption of photons due to photoionisation of H also gives an outwards effective force to the gas. Haehnelt (1995), Draine(2011) and Raga et al. (2015) incorporate radiation pressure due to photoionization of H, on the internal gas of spherical HII regions. They use similar expressions for this force in their HII region models, which can be obtained as follows.

Consider an ionising photon with frequency ν, captured by an H atom at a radius

R in the nebula. This photon then transmits a momentum $h\nu/c$ to the gas. Thus, the total momentum due to photoionisation in a volume element at a radius R is the photoionization rate $\times h\nu/c$ integrated over all the ionising frequencies ($> \nu_H$, the photoionization frequency of H):

$$f_H = \int_{\nu_H}^{\infty} \frac{L_\nu}{h\nu 4\pi R^2} \exp\left\{-\int_0^R \kappa' dR'\right\} n_{HI}\sigma_\nu \frac{h\nu}{c} d\nu, \tag{2.57}$$

where the photon flux per unit frequency also takes into account the absorption of ionising photons by dust grains, through the absorption coefficient κ (see section 2.1). We note that the product $\sigma_\nu \nu$ depends on the frequency as $\propto \nu^{-2}$ and then the *grey ISM approximation* can be applied, giving

$$f_H = n_{HI}\sigma_H \frac{\langle h\nu \rangle_i}{c} \frac{S_*}{4\pi R^2} \exp\left\{-\int_0^R \kappa' dR'\right\} = \alpha_B \frac{\langle h\nu \rangle_i}{c} n^2, \tag{2.58}$$

where in the second equality of equation (3.4) we consider the condition of photoionisation-recombination equilibrium discussed in Section 2.1. The radiation pressure per unit volume due to photoionization of H obtained with this approach, depends basically on the square of the density of the nebula.

Haehnelt (1995) consider the radiation pressure due to photoionisation to discuss the concentration of gas during galaxy formation. This author considers a sphere with a central ionising source and estimates that inside a radius

$$R_{ph} = \frac{3\alpha_{tot} h\nu_0}{4\pi c G m_p} \simeq 100 - 150\text{pc} \tag{2.59}$$

the force due to photoionisation of H dominates the inwards self-gravity force. In equation (2.59), α_{tot} is the total recombination coefficient, and ν_0 is the ionising frequency of H. This R_{ph} radius is obtained by Haehnelt (1995) by considering a self-gravitating HII region with an "averaged uniform density".

Raga et al. (2015) calculate with more detail the photoionization radiation pressure on self-gravitating HII regions, by solving a *modified Lane-Emden equation* with an additional term corresponding to the photoionisation radiation pressure (radiation pressure on dust is not considered). These authors find that radiation pressure has a noticeable effect on the density structure of the nebula if it has a central density greater than 10 cm^{-3}. Also, if the central source has a photon rate

of ionising photons equivalent to ~ 100 O stars, the resulting HII region extends from a radiation pressure-dominated regime to a gravity-dominated regime (see Figure 1 of Raga et al. 2015).

Therefore, in HII regions powered by a single or a few massive stars (e. g. from ultracompact to classical HII regions) self-gravity is completely negligible and the model equations of Draine (2011) (which include, radiation pressure due to photoionisation and dust absorption with no self-gravity) could be applied.

In the next chapter we develop an analytic model of HII regions with radiation pressure which we compare with the numerical solutions of Draine's equations. In Chapter 4 we extend our study to a planar configuration, where we include self-gravity, since the application of this configuration is for starbursts in galactic disks.

Chapter 3

Radiation Pressure in Spherical HII Regions

In this chapter we revisit Draine's (2011) problem: a spherical, dusty, hydrostatic H II region in which the radiation pressure (associated with photoionisation and dust absorption) is important. This model do not consider the gas self-gravity and is appropriate for HII regions powered by a single star as, ultracompact, compact and classical. In this regime where self-gravity is negligible, we surprisingly find a simple, approximate analytic solution for the nebular density structure, which agrees very well with Draine's numerical model. Being analytic, this solution provides a relatively simple way for evaluating the conditions under which the radiation pressure has an important effect on the nebular structure. Most of the content of this chapter can be found in the paper by Rodríguez-Ramírez et al. (2016).

3.1 The model equations

The equation of hydrostatic balance for the gas within an isothermal H II region can be written as:

$$2kT\frac{dn}{dR} = f_d + f_H\,; \tag{3.1}$$

where k is Boltzmann's constant, $T = 10^4$ K the typical temperature of photoionized regions, n the atom/ion number density (assumed to be dominated by Hydrogen), R the spherical radius, and f_d and f_H representing the effect of radiation pressure due to dust absorption and photoionization (respectively).

Assuming a position- and frequency-independent dust absorption cross section σ_d (per H atom/ion), the radiation pressure on dust grains can be written as:

$$f_d = \frac{n\sigma_d L_*}{4\pi c R^2} e^{-\tau_d} \,, \tag{3.2}$$

where L_* is the stellar luminosity, c is the speed of light and τ_d is the dust optical depth given by

$$\tau_d = \sigma_d \int_0^R n(R')dR' \,. \tag{3.3}$$

Draine (2011) divides the dust absorption radiation pressure term into two terms, treating separately the photons with energies above and below the Lyman limit. However, in equation (3.2), we have neglected the contribution of the optical depth due to photoionization processes τ_H, present at frequencies such that $h\nu > 13.6$ eV (see equation 2.47-2.48). Raga & Lora (2015) have shown that neglecting the contribution of photoionization to the optical depth has a surprisingly small effect on the resulting structures.

For a gas in photoionization equilibrium, the photoionization radiation pressure term is given by equation (2.58) (derived in Section 2.3 of last Chapter):

$$f_H = n^2 \alpha_B \frac{\langle h\nu \rangle_i}{c} \,, \tag{3.4}$$

where c is the speed of light, α_B ($= 2.60 \times 10^{-13} \mathrm{cm^3 s^{-1}}$ for a $T = 10^4$ K gas) is the H case B recombination coefficient, and $\langle h\nu \rangle_i = 18$ eV is the mean energy of the ionising photons. We have assumed that the H gas is almost fully ionised, and that the ionising photons have frequencies close to the Lyman limit. This radiation pressure term is discussed in more detail by Draine (2011) and by Raga et al. (2015).

A fundamental point is that the density stratifications described by equations (3.1)-(3.3) end at the "Strömgren radius" R_S, determined by the balance between the recombination rate of the material within R_S, the dust absorption, and the ionising photon rate S_* produced by the central star.

This "Strömgren's relation" can be obtained by integrating both sides of equation (2.49) from the $R = 0$ to $R = R_S$ giving

$$S_* = 4\pi\alpha_B \int_0^{R_S} n^2(R) R^2 dR + S_* \sigma_d \int_0^{R_S} n(R) e^{-\tau_d(R)} dR \,, \tag{3.5}$$

where τ_d is given by equation (3.3), and we have again neglected the photoionisation optical depth τ_H and used the boundary conditions $S(0) = S_*$, $S(R_S) = 0$.

Equation (3.5) was also derived by Raga & Lora (2015) under the assumption that in the bulk of the interior of the photoionized region the optical depth is dominated by the dust absorption (i.e., with only a small contribution due to photoionization processes). These authors show that the Strömgren radius obtained under this approximation is in very close agreement with the one obtained considering the contribution of photoionization to the optical depth.

If we now consider the differential $d\tau_d = \sigma_d n dR$ (see equation 3.3) in the second integral of the RHS of equation (3.5), we obtain

$$S_* \sigma_d \int_0^{R_s} n \mathrm{e}^{-\tau_d}\, dR = S_* \int_0^{\tau_s} \mathrm{e}^{-\tau_d}\, d\tau_d = S_* \left(1 - \mathrm{e}^{-\tau_s}\right), \tag{3.6}$$

where

$$\tau_s = \sigma_d \int_0^{R_s} n(R) dR, \tag{3.7}$$

is the optical depth evaluated at the Strömgren radius R_s. Furthermore, combining equations (3.5), (3.6) and (3.7), the Strömgren relation can be written in the simpler form

$$\exp\left\{-\sigma_d \int_0^{R_s} n\, dR\right\} S_* = 4\pi\alpha_B \int_0^{R_s} R^2 n^2\, dR. \tag{3.8}$$

Equation (3.5) (or alternatively equation 3.8) requires a specified ionising photon rate of the central star S_*, which can take a wide range of possible values. However, for massive main-sequence stars the ionising photon rate S_* can be calculated as a function of its luminosity L_* as

$$\frac{S_*}{S_{\mathrm{O9.5}}} = k_1 \left(\frac{L_*}{L_\odot}\right) \exp\left\{-k_2 \left(\frac{L_\odot}{L_*}\right)\right\}, \tag{3.9}$$

where $S_{\mathrm{O9.5}} = 10^{47.88}$ s^{-1} is the ionising photon rate of a O9.5V star and $k_1 = 8.9 \times 10^{-5}$ and $k_2 = 7 \times 10^4$ are numerical constants that gives the best fit of the analytical form of equation (3.9) to the data points in Figure 3.1. These data points are the stellar luminosity and ionising photon rate associated to each spectral type from O9.5V to O3V stars, obtained from Table 4 of Martins et al. (2005).

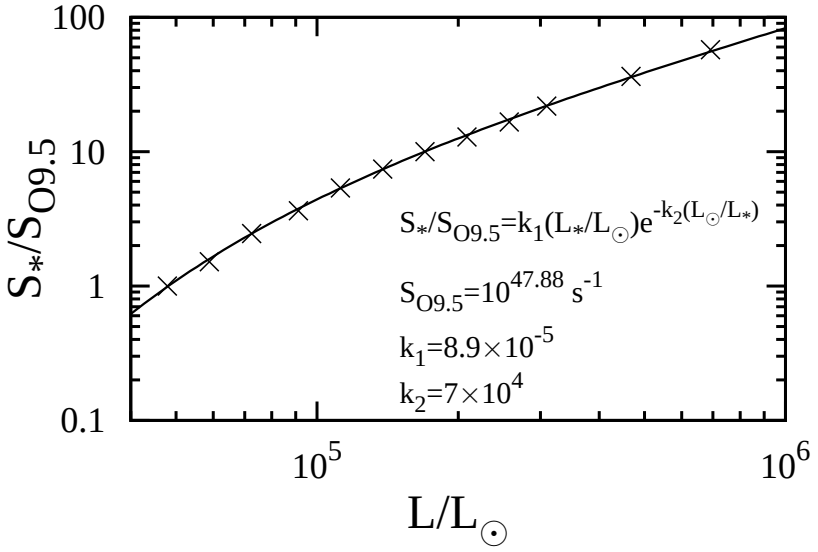

Figure 3.1: The ionising photon rate as a function of the stellar luminosity for main sequence stars. The data points correspond to the spectral types from O9.5 to O3 stars, taken from Martins et al. (2005). The curve is our best analytical fit.

3.2 The approximate analytic solution

Equation (3.1) has probably no exact analytic solution for the number density n as a function of the spherical radius R. However, we can obtain an approximate analytic solution as follows.

We first write equation (3.1) as

$$\frac{dn}{dR} = \frac{\sigma_d L_*}{8\pi ckT}\frac{n}{R^2} + \delta, \tag{3.10}$$

where

$$\delta = \frac{\sigma_d L_*}{8\pi ckT}\frac{n}{R^2}\left(\exp\left\{-\sigma_d\int_0^R n\,dR'\right\} - 1\right) + \frac{\alpha_B\langle h\nu\rangle_i}{2kTc}n^2. \tag{3.11}$$

We now assume that, for $R < R_s$ (being R_s the outer boundary of the nebula, see subsection 2.2) the value of $|\delta|$ is negligible in comparison with the first term in RHS of equation (3.10). This assumption can be understood as follows. The first term in the RHS of equation (3.11), which is the contribution of the optical depth to the density gradient, always takes negative values. On the other hand, the radiation pressure due to photoionization of H, which is the second term in the RHS of equation (3.11), takes small positive values. Thus, there is a partial "cancelling effect" which results in small values of $|\delta|$.

Ignoring the last term in equation (3.10) and considering the nebula to have a density n_s at the external radius R_s, we trivially integrate equation (3.10), obtaining

$$n = n_s \exp\left\{-R_{ch}\left(\frac{1}{R} - \frac{1}{R_s}\right)\right\}, \tag{3.12}$$

with

$$R_{ch} \equiv \frac{\sigma_d L_*}{8\pi ckT}, \tag{3.13}$$

the characteristic radius. The solution (3.12) gives a vanishing small density for $R \to 0$. This central "hole" (which is clearly seen in the numerical solutions of Draine 2011), is well defined for $R < R_{ch}$. On the other hand, if the dust abundance in the HII region is not important, $R_{ch} \to 0$ giving $n \to n_s$, and we recover an HII region with uniform density.

If we now combine the solution (3.12) with the Strömgren relation (3.8), we obtain

$$S_* \exp\left[-\sigma_d \exp\left\{\frac{R_{ch}(\sigma_d, L_*)}{R_s}\right\} I_2\, n_s\right] = 4\pi\alpha_B \exp\left\{\frac{2R_{ch}(\sigma_d, L_*)}{R_s}\right\} I_1\, n_s^2, \tag{3.14}$$

where

$$I_1(R_s, \sigma_d, L_*) \equiv \int_0^{R_s} R^2 \mathrm{e}^{-R_{ch}/R} dR$$

$$= \frac{R_s}{3}\mathrm{e}^{-2R_{ch}/R_s}\left(2R_{ch}^2 - R_{ch}R_s + R_s^2\right) - \frac{4R_{ch}^3}{3}\mathrm{E}_1\left(2R_{ch}/R_s\right), \tag{3.15}$$

$$I_2(R_s, \sigma_d, L_*) \equiv \int_0^{R_s} \mathrm{e}^{-R_{ch}/R} dR = R_s \mathrm{e}^{-R_{ch}/R_s} - R_{ch}\mathrm{E}_1\left(R_{ch}/R_s\right), \tag{3.16}$$

where E_1 is the exponential integral function and $R_{ch}(\sigma_d, L_*)$ the characteristic radius given by equation (3.13). In the limit where

$$\frac{R_{ch}}{R_s} << 1,$$

we obtain that

$$I_1 \to \mathrm{e}^{-2R_{ch}/Rs}\frac{R_s^3}{3}, \quad I_2 \to \mathrm{e}^{-R_{ch/Rs}} R_s,$$

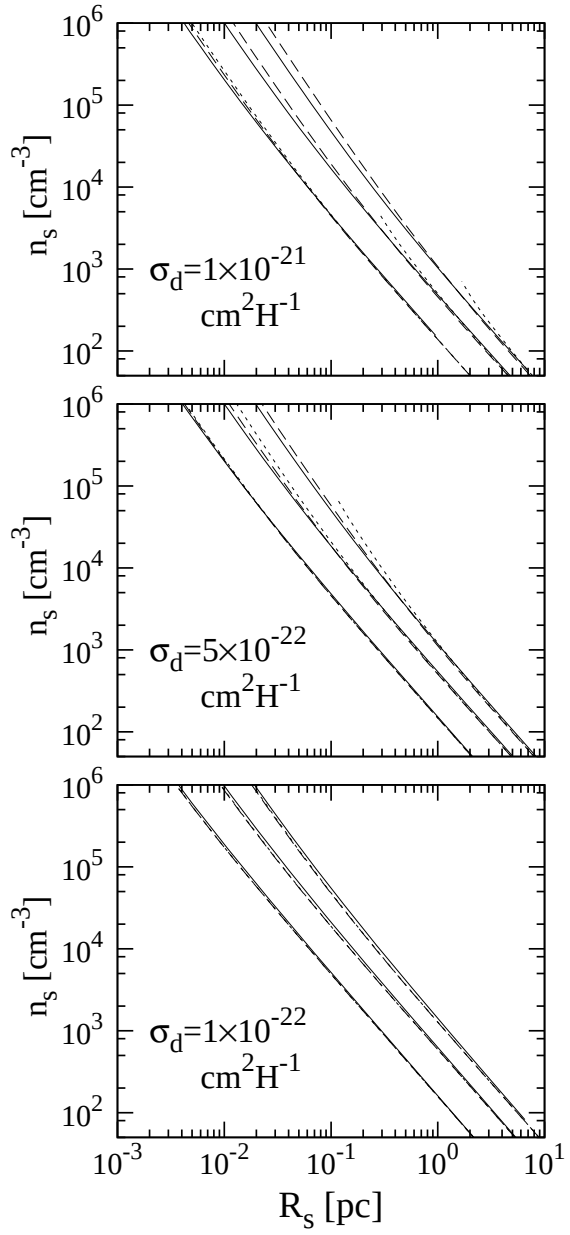

Figure 3.2: External density n_s of an HII region as a function of the external radius R_s. The solid curves are obtained by solving numerically equations (3.20-3.22), the long dashed curves are obtained with the implicit analytic solution (3.14) and the short dashed curves with the explicit analytic solution (3.19). In each graph all the curves corresponds to the same value of σ_d (which we specify with a label in each graph) and the different curves correspond to $L_* = 5 \times 10^4$, 2.5×10^5 and 10^6 $L_\odot$, from the lower to the upper curves.

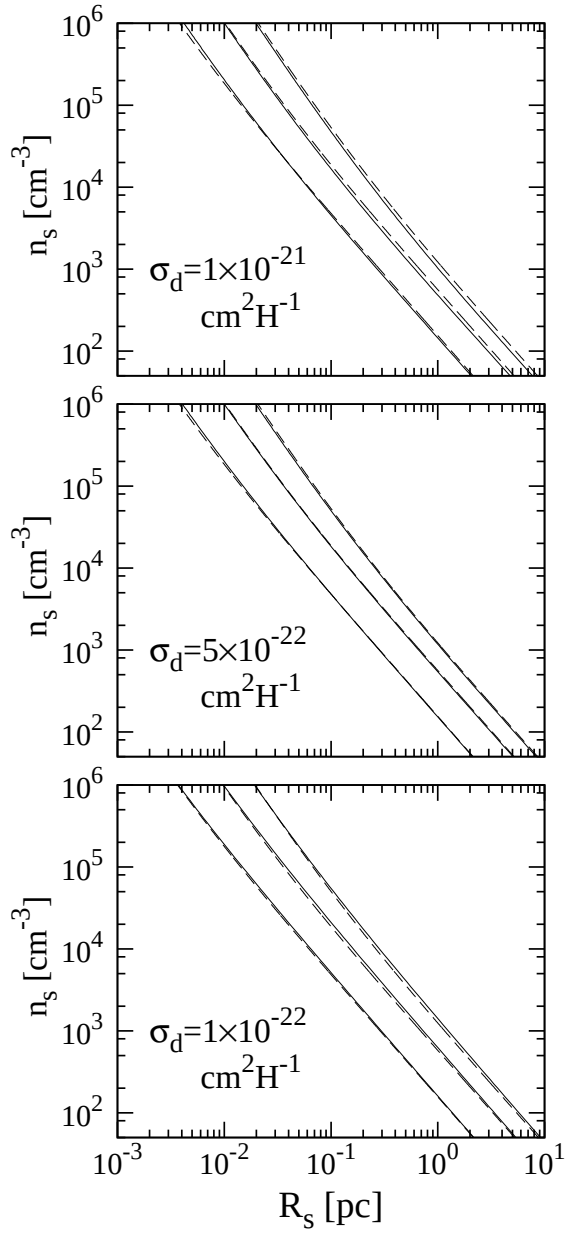

Figure 3.3: External density n_s of an HII region as a function of the external radius R_s. The solid curves are the same numerical solutions plotted in Figure 3.2. The dashed curves are obtained with the analytic solution (3.25), and correspond to the same values of σ_d and L_* used in Figure 3.2.

and therefore equation (3.14) takes the form

$$R_s = \mathrm{e}^{-\sigma_d n_s R_s/3} R_{s,0}\,, \tag{3.17}$$

being

$$R_{s,0} = \left(\frac{3S_*}{4\pi\alpha_B n_s^2}\right)^{1/3}, \tag{3.18}$$

the Strömgren radius of a dustless HII region with uniform density n_s. Equation (3.17) is the result discussed by Franco et al. (1990) and Raga & Lora (2015), which relates the radius R_s of a dusty, fully ionised, non stratified, HII region with the radius $R_{s,0}$ of the corresponding dustless model (the standard Strömgren radius).

Returning to the stratified case, if one specifies the values of R_s, σ_d and L_*, equation (3.14) gives the outermost density n_s in implicit form. However, we can also obtain n_s in an approximate explicit form by considering a second order expansion of the LHS of equation (3.14), which gives

$$n_s(R_s,\sigma_d,L_*) = \frac{\exp\left\{-R_{ch}(\sigma_d,L_*)/R_s\right\}}{8\pi\alpha_B I_1/S_*(L_*) - (\sigma_d I_2)^2}\left[\sqrt{\frac{16\pi\alpha_B I_1}{S_*(L_*)} - (\sigma_d I_2)^2} - \sigma_d I_2\right]. \tag{3.19}$$

In summary, given specific values of the σ_d and L_* parameters, one obtains with equation (3.14) (or alternatively with equation 3.19), the outermost density n_s as a function of the external radius R_S. Once n_s and R_s are defined, one obtains the internal density structure of the HII region analytically using equation (3.12). In the next section we compare this analytic approximated solutions with the corresponding numerical integrations of equations (1)-(3) of Draine (2011), which we consider to be the complete equations of the problem discussed in this chapter.

3.3 Comparison of the analytic solution with Draine's model

In order to evaluate the accuracy of the approximate analytic solutions derived in the previous section (equations 3.12-3.14 and 3.19), we compare them with numerical

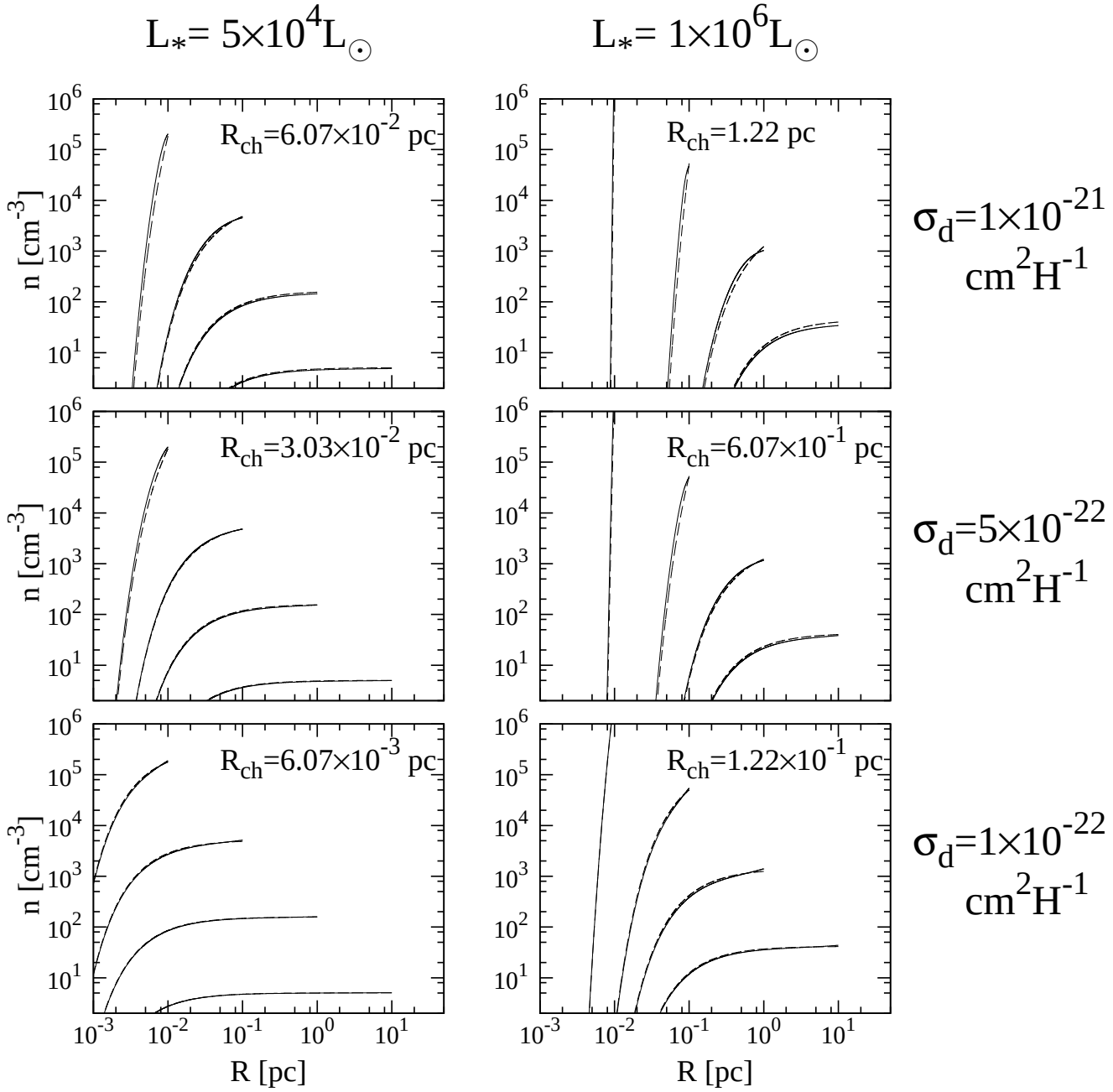

Figure 3.4: Models of the internal density structure n of HII regions as a function of its spherical radius R. The different solutions in each graph correspond to external boundaries $R_s = 10, 1, 0.1$ and 0.01 pc and all of them are calculated with the same values of the σ_d and L_* parameters. The different graphs take the configuration of the σ_d and L_* parameters as indicated at the end of each row and at the top of each column, respectively. The solid curves are the numerical solutions of equations (3.20)-(3.22), and the dashed curves are the analytical solutions obtained with equations (3.25)-(3.27).

integrations of the model equations of the problem without the simplifications done in sections 2 and 3. These equations are those of Draine (2011):

$$2kT\frac{dn}{dR} = \sigma_d n \frac{L_n \mathrm{e}^{-\tau} + L_i \phi}{4\pi c R^2} + \frac{\alpha_B \langle h\nu \rangle_i}{c} n^2, \tag{3.20}$$

$$\frac{d\phi}{dR} = -\frac{\alpha_B 4\pi R^2 n^2}{S_*} - \sigma_d \phi n, \tag{3.21}$$

$$\frac{d\tau}{dR} = \sigma_d n, \tag{3.22}$$

where L_n and L_i are the luminosities of non-ionising and ionising photons respectively. We write these luminosity components as functions of the total luminosity L_* as

$$L_i = S_*(L_*)\langle h\nu \rangle_i, \tag{3.23}$$

$$L_n = L_* - L_i, \tag{3.24}$$

where S_* is given by equation (3.9) and we take the mean energy of the ionising photons as $\langle h\nu \rangle_i = 18$ eV. The functions τ and ϕ must satisfy the boundary conditions and $\tau(0) = 0$, $\phi(0) = 1$ and the integrations stop at the boundary radius R_s satisfying the condition $\phi(R_s) = 0$.

However, we should choose boundary conditions displaced from the origin in order to avoid the singularity of equation (3.20) (the pressure balance) at $R = 0$. Choosing fixed values of σ_d and L_*, we generate numerical solutions with different external radius R_s (and associated densities n_s), by initialising the integrations at the fixed low density $n_{ini} = 10^{-3}$ cm^{-3} and varying the initial radius $R_{ini} > 0$. In this way the conditions $\tau(R_{ini}) = 0$ and $\phi(R_{ini}) = 1$ are approximately satisfied.

In Figure 3.2 we show (with solid lines) the outermost density n_s as a function of the external radius R_s, obtained from the numerical solutions of equations (3.20)-(3.22), corresponding to fixed values of the σ_d and L_* parameters. The curves in each graph share the same value of the dust absorption cross section σ_d. In the bottom, middle and top graphs, the solutions correspond to $\sigma_d = 0.1, 0.5$ and 1×10^{-21} cm^2 H^{-1}, respectively. The different curves in the same graph correspond to stellar luminosities of $L_* = 5 \times 10^4$, 2.5×10^5 and 10^6 L$_\odot$, from the lower to the upper curves.

We also include in Figure 3.2 the analytical solutions for n_s vs R_s obtained in

Section 3. We plot (with long dashed lines) the implicit analytic solution given by equation (3.14) and (with short dashed lines) the explicit analytic solution given by equation (3.19). We can see that for the relatively low dust abundance $\sigma_d = 10^{-22}$ cm^2 H^{-1} the implicit and explicit analytic solutions are practically indistinguishable and are in very good agreement with the numerical solutions, for all the luminosity values considered in Figure 3.2.

However, for larger values of σ_d the difference between the implicit and the explicit analytical solutions is noticeable, and both analytic approaches loose accuracy (in following the numerical solutions) as R_s decreases. Also, the explicit analytic solution is not defined in all the R_s domain, since equation (3.19) has critical values of R_s below which the involved root square is not defined, and also has problems when its denominator is zero. We can see these critical points where the short dashed curves end as R_s decreases, in the central and top panels of Figure 3.2.

If we look at the numerical solutions only (the solid curves), we note that the effect of increasing the value of σ_d (for any value of L_*) is a "small rotation" of the n_s vs R_s curves in the clockwise direction. On the other hand, the explicit analytic solutions (short dashed curves) undergo the same effect but in a more pronounced manner. This makes the explicit analytic solutions with $\sigma_d = 2 \times 10^{-22}$ cm^2 H^{-1} fit very well the numerical solutions with $\sigma_d = 10^{-21}$ cm^2 H^{-1}. Also, equation (3.19) (which gives the explicit analytical solutions) is well defined for $\sigma_d < 3 \times 10^{-22}$ cm^2 H^{-1} (i. e., does not still acquire negative values inside its involved root square) in all the R_s domain.

Therefore, we propose an improved approximate analytic solution for the outermost density of the nebula as a function of R_s, σ_d and L_*, of the form

$$\widetilde{n}_s = n_s(R_s, \widetilde{\sigma}(\sigma_d), L_*), \tag{3.25}$$

where n_s is given by equation (3.19) and $\widetilde{\sigma}$ is a function that maps the value of σ_d as

$$\widetilde{\sigma} = \sigma_1 \exp\left\{-\sigma_2/\sigma_d\right\}, \tag{3.26}$$

with the constants $\sigma_{1,2} = 2.1, 0.4 \times 10^{-22}$ cm^2 H^{-1}.

In Figure 3.3 we plot the curves given by equations (3.25) and (3.26) (with long dashed lines) together with the numerical n_s vs R_s (with solid lines) corresponding

to the same values of σ_d and L_* used in Figure 3.2. The comparison between both approaches show that the explicit analytic solution (3.25) is more accurate than the previous (3.14) and (3.19) solutions, in following the curves given by the numerical integrations.

Therefore, we substitute the outermost density function $\widetilde{n}_s$ instead of n_s in equation (3.12) to obtain analytically the internal density stratification of the nebula as

$$n = \widetilde{n}_s \exp\left\{-\frac{\sigma_d L_*}{8\pi ckT}\left(\frac{1}{R} - \frac{1}{R_s}\right)\right\}. \tag{3.27}$$

We plot this analytic solution in Figure 3.4, where we also plot the numerical solutions of equations (3.20)-(3.22) for the internal density n of the HII region as a function of the spherical radius $R < R_s$. We present an array of graphs with several models. In each graph we show four solutions, all of them sharing the same fixed value of the σ_d and L_* parameters, but with different outer boundaries $R_s = 10, 1, 0.1$ and 0.01 pc. These values of R_s cover the characteristic radii from classical to hyper-compact HII regions (see Kurtz & Franco 2002).

The graphs in the same column (of Figure 3.4) show solutions with the same value of the luminosity of the central star, and we consider $L_* = 5 \times 10^4$ and 1×10^6 $L_\odot$ in the left and right column, respectively (as indicated on the top of each column). The graphs in the same row share the same value of the cross section of dust absorption, and we consider the values of $\sigma_d = 10^{-21}$, 5×10^{-22} and 10^{-22} cm^{2}H^{-1} from top to bottom.

Figure 3.4 shows that the analytic density stratifications closely follow the numerical solutions in the cases with relatively low dust absorption cross sections $\sigma_d = 10^{-22}$ cm^2 H^{-1}, for both considered values of L_*. As σ_d takes larger values, the analytic solutions loose accuracy in following the numerical curves, with the largest deviations being obtained for the configurations with $\sigma_d = 10^{-21}$ cm^2 H^{-1}, $L_* = 10^6$ $L_\odot$. We therefore conclude that the analytic solution (3.27), works very well for HII regions with dust abundances in the interval 10^{-22}-10^{-21} cm^2 H^{-1}, and with luminosities of the central star $L_* < 1 \times 10^6$ $L_\odot$.

3.4 Discussion

3.4.1 The astrophysical parameters

According to Draine (2011), the hydrostatic state of an HII region under the effect of the radiation pressure due to photoionization of H and dust absorption, is determined by seven physical parameters. Three parameters correspond to the central star: L_n, S_* and $\langle h\nu \rangle_i$, and four parameters correspond to the ionised gas: T, α_B, σ_d and p_{edge} (the confining pressure of the nebula).

In this chapter we limit our study to HII regions with a single central star (as HII regions powered by a stellar cluster are likely to be affected by gravity, as discussed in Subsection 5.3). Thus, the rate of ionising photons S_* is considered as a derived parameter which depends on the total stellar luminosity L_* (see equation 3.9).

On the other hand, due to the simplifications considered in Sections 2 and 3, the $\langle h\nu \rangle_i$ parameter is not present explicitly in our analytic solution (3.27). When evaluating this parameter for the numerical solutions of the complete equations (3.20)-(3.22), we considered that $L_n = L_* - S_*(L_*)\langle h\nu \rangle_i$, depending only on the total luminosity of the central star (since we considered the fixed value of $\langle h\nu \rangle_i$=18 eV). This quantity is actually a function of the effective temperature of the central star, but only varies within a range from $\langle h\nu \rangle_i \sim 13.6$ (for the less massive photoionizing stars) to ~ 20 eV. This change does not introduce strong differences between our analytic models and the numerical solutions of the complete equations, as shown in Figures 3.3 and 3.4.

The ionised gas of HII regions always has a temperature $T \sim 10^4$K. Therefore, the recombination coefficient α_B has very similar values for all nebulae. Therefore, in this chapter we consider the T and α_B as fixed quantities.

The dust absorption cross section σ_d can take different values. In this chapter we considered that in HII regions σ_d is likely to be lower than the $\sigma_d = 10^{-21}$ cm^2 H^{-1} value corresponding to the average abundance of dust in the neutral ISM.

Finally, instead of p_{edge}, we alternatively consider the outer boundary R_s as a free parameter. R_s is related with p_{edge} through equation (3.25).

In summary, for the analytic model derived in this chapter, we only consider three free parameters (for determining the hydrostatic solution of an H II region): R_s, σ_d and L_*.

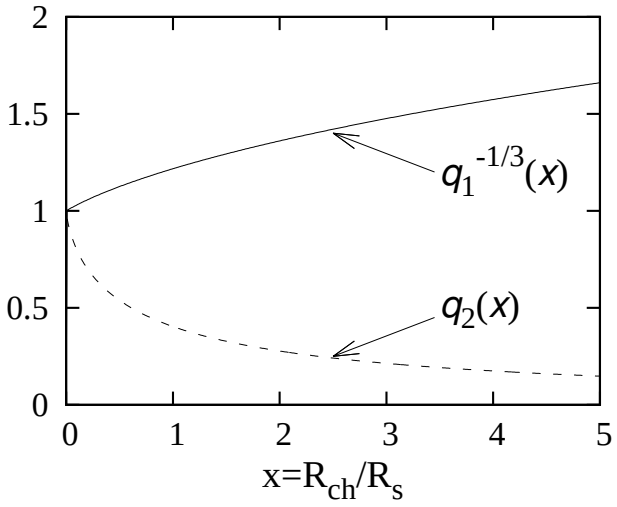

Figure 3.5: Functions $q_1^{-1/3}(x)$ and $q_2(x)$ defined by equations (3.29) and (3.30), respectively (see the text).

3.4.2 Characterisation of the analytic solutions

As we can see from Figure 3.4, the analytic solution given by equations (3.25)-(3.27) result in three main types of density distribution:

- solutions with $R_{ch}/R_s << 1$. In these solutions the extension of the central "density hole" is negligible in comparison with the outer boundary R_s of the nebula. These solutions correspond to HII regions with a practically homogeneous density;

- solutions with $R_{ch}/R_s >> 1$. The central hole of these solutions covers practically all of the volume of the HII region. There is a density jump in the external part of the nebula with a small radial extension (in comparison with the radius R_s of the HII region). This kind of nebula has the shape of a thin ring;

- solutions with $R_{ch}/R_s \sim 1$. These solutions are strongly stratified along all of their radial extension.

We show in Figures 3.6 and 3.7, the three regimes described above. We plot the ratio $R_{ch}/R_s = (\sigma_d L_*)/(8\pi ckT)$ as a function of L_*, for $R_s = 0.1$ in Figure 3.6, and for $R_s = 0.01$ in Figure 3.7. In each plot the configurations with $\sigma_d = 10^{-21}$ cm^2 H^{-1} are in the thick solid line, and the configurations with $\sigma_d = 10^{-22}$ cm^2 H^{-1} in

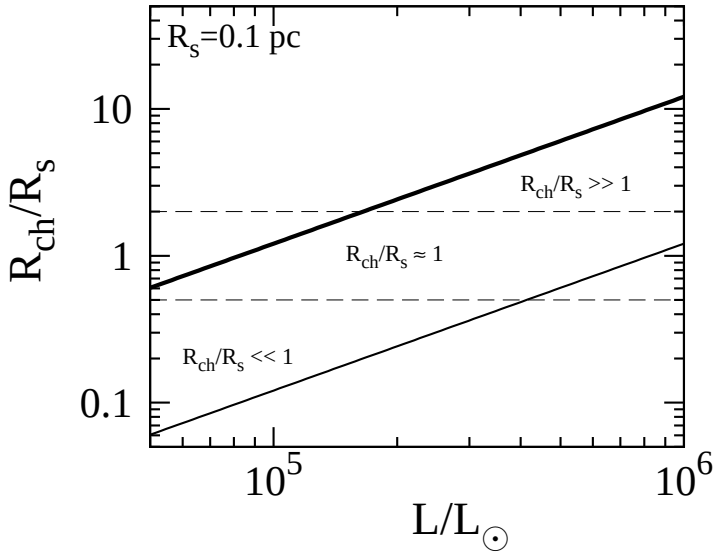

Figure 3.6: Values of the $R_{ch}/R_s = (\sigma_d L_*)/(8\pi ckT)$ ratio, for $R_s = 0.1$ pc. The configurations with $\sigma_d = 10^{-21}$ cm^2 H^{-1} are in the thick solid line, and the configurations with $\sigma_d = 10^{-22}$ cm^2 H^{-1} in the thin solid line. The dashed lines define the zones of the three types of solutions (see the text).

thin solid line. Therefore, all the solutions considered in Figure 3.4 are between the thick an the thin solid lines. The dashed lines define the zones for the different type of solutions mentioned above ($R_{ch}/R_s << 1$, $R_{ch}/R_s >> 1$ and $R_{ch}/R_s \sim 1$).

We note that for nebulae with $R_s \sim 0.1$ pc (Figure 3.6), the three type of density distributions are equally likely to occur. On the other hand, for nebulae with $R_s \sim 0.01$ pc (Figure 3.7), the $R_{ch}/R_s >> 1$ solution appears to be the most frequent.

An interesting point is how the radiation pressure affects the size of the nebula, in comparison with previous models where radiation pressure is not taken into account. Let us note that the stratified Strömgren relation given by equation (3.14) can also be written as

$$R_s = q_1^{-1/3}(x) \exp\left\{-\sigma_d n_s R_s q_2(x)/3\right\} R_{s,0}, \tag{3.28}$$

where

$$q_1(x) \equiv 1 - x + 2x^2 - 4x^3 \mathrm{E}_1(2x) \mathrm{e}^{2x}, \tag{3.29}$$

$$q_2(x) \equiv 1 - x \mathrm{E}_1(x) \mathrm{e}^{x}, \tag{3.30}$$

$$x \equiv \frac{R_{ch}}{R_s}, \tag{3.31}$$

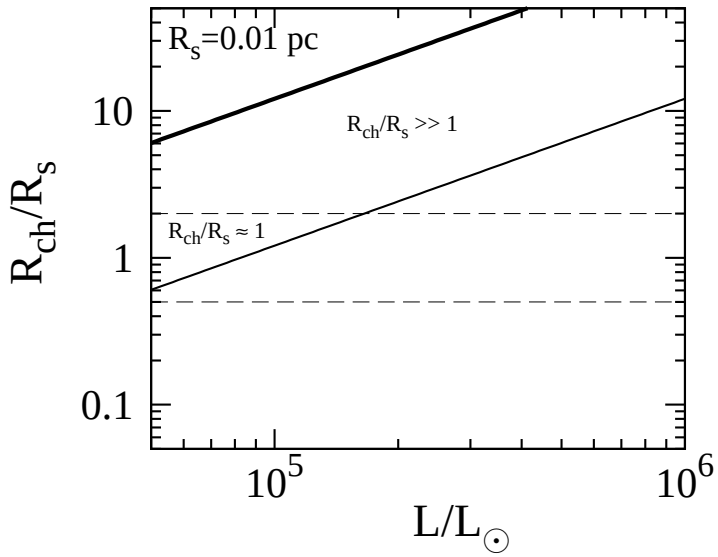

Figure 3.7: Values of the $R_{ch}/R_s = (\sigma_d L_*)/(8\pi ckT)$ ratio, for $R_s = 0.01$ pc. The configurations with $\sigma_d = 10^{-21}$ cm^2 H^{-1} are in the thick solid line, and the configurations with $\sigma_d = 10^{-22}$ cm^2 H^{-1} in the thin solid line. The dashed lines define the zones of the three types of solutions (see the text).

R_{ch} is given by equation (3.13) and $R_{s,0}$ is the standard (dustless) Strömgren radius given by equation (3.18).

In the uniform density case (which corresponds to q_1, $q_2 \to 1$ when $x \to 0$), the size of the nebula is reduced (in comparison with the standard $R_{s,0}$ radius) due to absorption of UV photons by dust (see Franco et al. 1990 and Raga & Lora 2015).

However, as $x = R_{ch}/R_s$ increases to non-negligible values in comparison with unity $q_1^{-1/3}(x) > 1$ and $q_2(x) \to 0$, (see Figure 3.5). Therefore R_s grows to a value of $R_{s,0}$ or larger (see equation 3.28). This means that the radiation pressure cancels out the size reduction effect due to dust absorption, found in the uniform density case (with no radiation pressure). Thus, a radiation pressure producing important stratifications ($R_{ch}/R_s \geq 1$), inflates the HII region back to a size comparable to the one of a dust-free nebula.

3.4.3 Models with important photoionization radiation pressure

In Section 3, we consider that the contribution of the photoionisation radiation pressure to the density gradient of the nebula, is partly cancelled by the effect of

the optical depth of dust absorption (see equations 3.10 and 3.11). This assumption is indeed correct for configurations of the σ_d and L_* parameters used to obtain the radial density stratifications plotted in Figure 3.4.

However, we can easily check from equations (3.10) and (3.11) that, as $\sigma_d \to 0$ the photoionization radiation pressure is the dominant effect on the stratification of the nebula. This corresponds to the dustless case studied by Raga et al. (2015), who also included the gas self-gravity to obtain the stratification of the nebula. These authors pointed out that it is necessary to have a central photon rate of $\sim$ 100 O stars, to power a spherical HII region to a radius where the effects of the photoionization radiation pressure and the self-gravity are noticeable.

We can see from Figure 1 in Raga et al. (2015) that stratifications in which photoionization radiation pressure is relevant, and at the same time self-gravity is still negligible, are nebulae with an external boundary $R_s \geq 50$ pc, reaching densities of $n_s > 50$ cm^{-3}. However, it is not likely to find neutral ISM regions with these dimensions, with a high enough pressure which could confine these giant HII regions.

The role of self-gravity in the models of Raga et al. (2015), is to produce an outwards decrease in the density of the nebula, (increased previously by the photoionization radiation pressure), resulting in low boundary densities which a standard neutral ISM is capable to confine.

We therefore conclude that models where photoionization radiation pressure is important without taking into account self-gravity, do not have clear astrophysical applications.

3.5 Cavities in compact HII regions

A common feature of the HII regions models shown in Figure 3.4 is a central cavity of gas density created by radiation on dust grains. Since we assumed a constant gas to dust ratio in the photoionised region (through the radially independent σ_d), gas cavities indicate dust cavities.

Dust cavities in compact nebulae have been measured by Inoue (2002) with a transfer model of Lyman continuum photons, together with the ratio of infrared fluxes of 13 Galactic HII regions (including compact and ultracompact types). This author reports the mean values of $r_d/r_i \sim 0.4$ and $r_d/r_i \sim 0.6$ for compact and

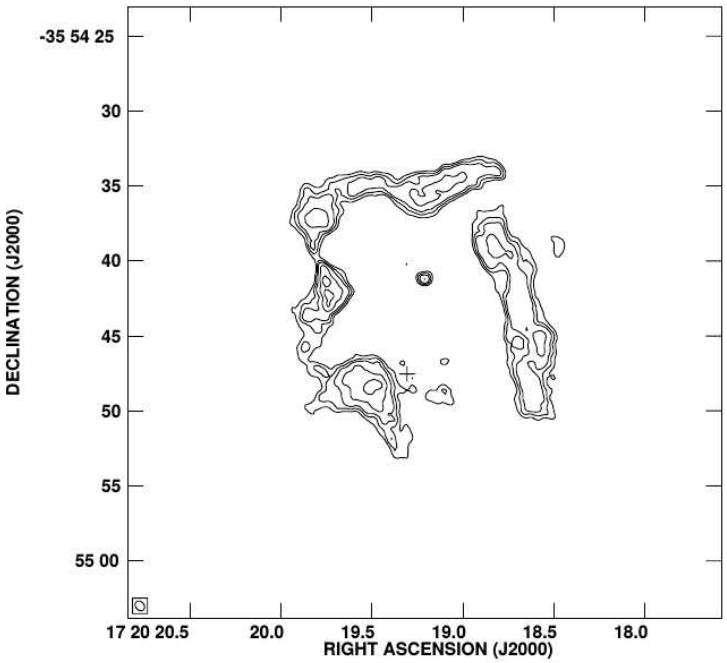

Figure 3.8: Radio image of the HII region NGC 6334A, taken from Carral et al. (2002).

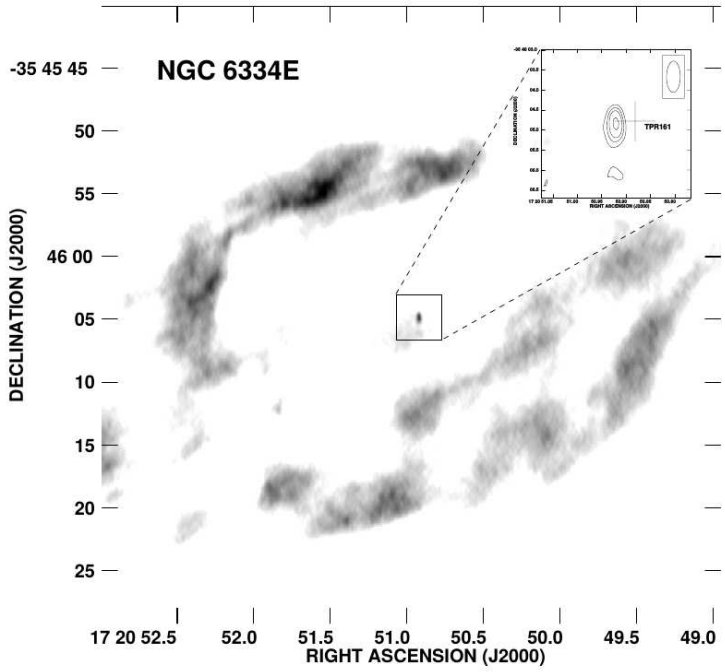

Figure 3.9: Grey-scale map of the HII region NGC 6334E, taken from Carral et al. (2002).

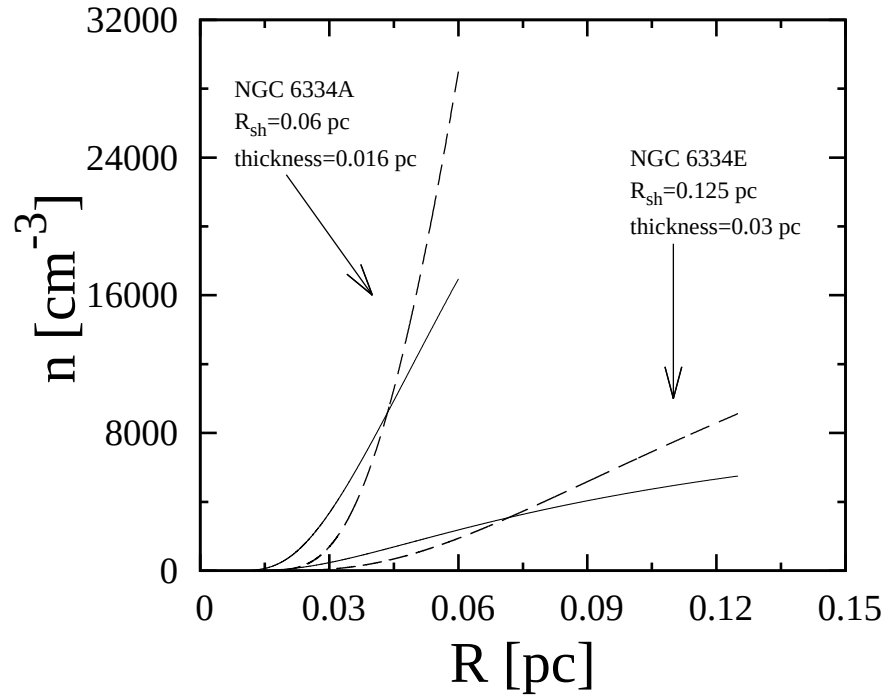

Figure 3.10: Density distributions as a function of the radius obtained from the analytic solution derived in this chapter given by equations (3.19) (3.25) and (3.27). The curves ending at 0.06 pc model the NGC 6334A nebula, and the curves ending at 0.125 pc model the NGC 6334E nebula (see the text). The size and the thickness of each nebula are taken from Carral et al. (2002).

ultracompact HII regions respectively, where r_d is radius of the cavity, and r_i the radius of the photoionised region (see his Table 3). These results agree with the trend of the models shown in Figure 3.4, where the ratio of the central cavity to the nebula boundary is larger as the HII region is more compact. Inoue (2002) points out that radiation pressure and/or stellar winds are the possible mechanisms that create dust cavities, ruling out dust sublimation which takes place in much smaller radii.

Carral et al. (2002) give observations of shell-like UC HII regions in the NGC 6334 star forming region. In particular, they analyse the NGC 6334A and NCG 6334E radio sources (see Figures 3.8 and 3.9), assuming that the central cavities are created by stellar winds. Applying the model of Castor et al. (1975) they find that the central star in each nebula should have a luminosity of $\sim 10^6$ $L_\odot$. However, from the observed ionisation, they obtain $\sim 8 \times 10^4$ L$\odot$ for the central star in each case. Furthermore, the wind-bubble model suggests that the compact HII regions mentioned above should be expanding at velocities of hundreds of kilometres per second, very high in comparison with ~ 10 km s^{-1} inferred from the recombination line ratios. To explain these over-estimations, Carral et al. (2002) suggest that the observed gaps in the ionised shells (see Figures 3.8 and 3.9) allow the wind gas to escape the HII regions, diminishing the the internal pressure of the nebulae and slowing down their expanding rates.

If the stellar winds escape, then radiation pressure on dust grains could be the dominant mechanism that creates the cavities in NGC 6334A and NGC 6334E. In Figure 3.10 we show density profiles of static HII regions with radiation pressure (the analytic solution obtained in this chapter), with boundary radii of 0.06 and 0.125 pc corresponding to NGC 6334A and NGC 6334E respectively (see Carral et al. 2002). We use the value of $\sigma_d = 10^{-21}$ cm^2 H^{-1} for all density profiles in Figure 3.10. The solid curves are obtained with $L_* = 8 \times 10^4$ $L_\odot$, which is the inferred luminosity from the ionisation of these regions (see Carral et al. 2002).

Additionally, we include density profiles with the same boundary radii, but with the enhanced luminosity of 1.5×10^5 $L_\odot$ with dashed lines. These last profiles have larger cavities and agree better with the thickness of the shells measured by Carral et al. (2002) (indicated in Figure 3.9) than the profiles with solid lines. Therefore, the static models of HII regions with radiation pressure derived in this chapter can

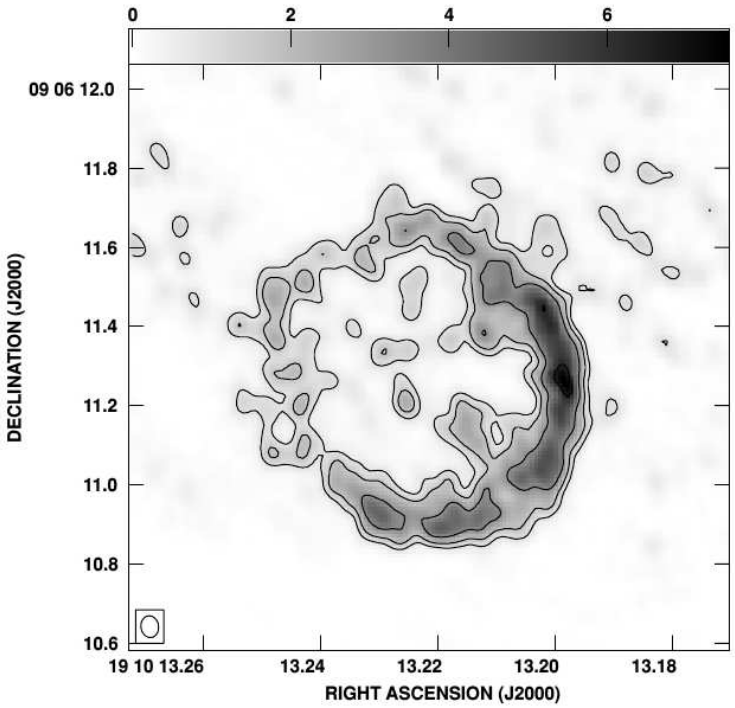

Figure 3.11: Observation of the W49A/D shell-like HII region, taken from De Pree et al. (2005).

reproduce the central cavities in shell-like UC HII regions with no need of stellar winds.

We then suggest that radiation pressure rather than stellar winds is the dominant mechanism that produce cavities in shell-like nebulae with gaps or leaky structure, and the analytic model derived in this chapter could be applied to interpret shell-like UC HII regions as e.g. NGC 6334A, NGC 6334E and W49A/D (see Figure 3.11 and De Pree et al. 2005).

3.6 Summary

Draine (2011) studied numerically the problem of a spherical, hydrostatic H II region considering the radiation pressure associated with dust absorption and with photoionization processes. In this chapter we consider the same problem and derive a simple, approximated analytic solution determined by three physical parameters of the system: the radius R_s of the nebula, the cross section of dust absorption σ_d, and the luminosity of the central star L_*. By specifying these parameters, our solution

gives the density n_s at the external boundary, and the internal density stratification as a function of the spherical radius.

Following Draine (2011) we consider two basic equations: one for the balance between gas pressure and radiation pressure due to dust absorption and photoionization of H (equation 3.1, which describes the density gradient of the HII region), and a second equation for the balance between the ionisation photon rate and the recombination rate of H and the dust absorption (equation 3.5, which determines the size of the nebula).

To proceed analytically we make two simplifications of the problem: (i) following Raga & Lora (2015) we consider that the optical depth of the photoionized region is dominated by the dust absorption, and (ii) we note that the effect of the optical depth, together with the radiation pressure due to photoionization of H, result in a negligible contribution to the balance equation that describes the density gradient of the nebula (see equations 3.10-3.11 and the associated text).

We compare our analytic solution with numerical integrations of the complete model equations of Draine (2011), and find that the analytic solution works very well when $L_* < 10^6$ L$\odot$ and σ_d takes values between 10^{-22} and 10^{-21} cm^2 H^{-1}.

Our analytic solution gives different kinds of stratifications, according to the chosen values of the parameters of the system. For example, we find that HII regions are strongly stratified along all of their radial extents when the condition $R_s \sim \sigma_d L_*/(8\pi ckT)$ is satisfied. We also find that the reduction effect in the external radius of dusty nebulae, found in previous models with no stratification, now disappears for $R_s < \sigma_d L_*/(8\pi ckT)$.

Chapter 4

Radiation Pressure in Planar HII Regions

In this Chapter we extend the study of the radiation pressure due to dust absorption and photoionization of H, to the case of a gaseous layer surrounding a planar distribution of stars. In the model, the gravity of the stars and the self-gravity of the diffuse gas are included.

Such a planar distribution is applicable for a star formation burst occurring in the disk of a spiral galaxy. Another possible application are dusty regions of dwarf irregular galaxies (which are believed to evolve into late spiral galaxies) which have masses dominated by the gaseous (rather than stellar) component (Banerjee et al. 2011). Also, planar distributions might be appropriate for modelling the extraplanar gas of spiral galaxies (Barnabè et al. 2006) and the levitating molecular clouds observed in some galaxies (Franco et al. 1991; Ferrara 1993).

The radiation pressure force initially pushes out the nebular gas, forming an expanding, dense shell (see, e.g., Krumholz & Matzner 2009). In the presence of a large enough external pressure, the expanding flow will eventually reach a hydrostatic configuration. This final configuration is determined from the balance between the radiation pressure (due to photoionization and dust absorption processes), the gravitational force (from the stellar and gaseous mass) and the gas pressure.

Assuming that the gas has a two-temperature structure (of $\approx 10^4$ K for an inner, photoionized region and of $\approx 10^3$ K for an outer, neutral region) we derive two dimensionless equations for the vertical stratification of the gas in plane-parallel

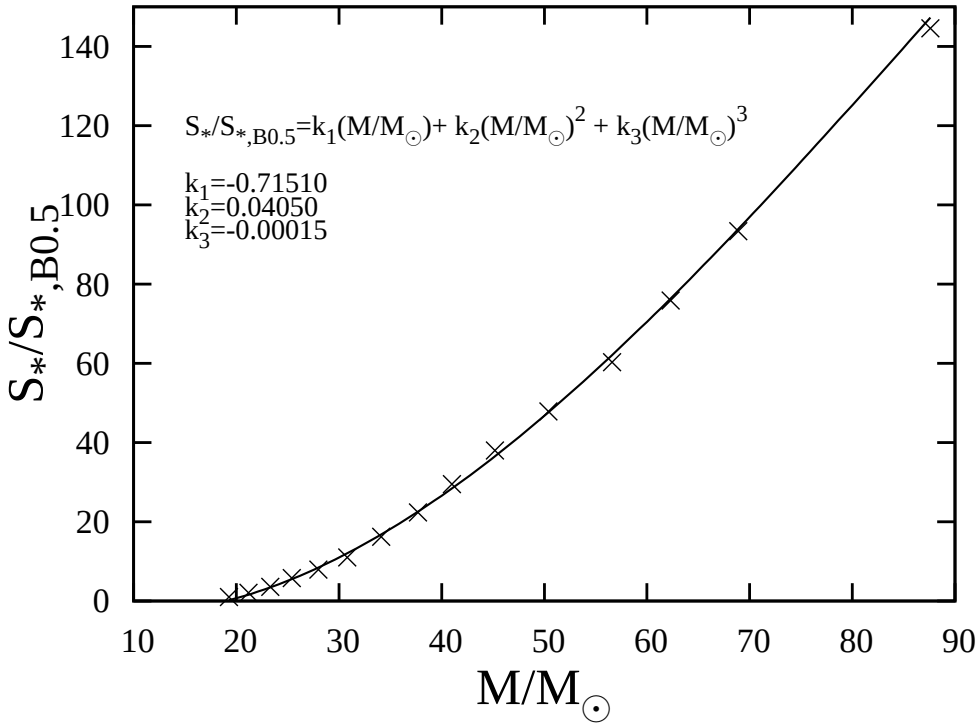

Figure 4.1: The ionising photon rate as a function of the stellar mass. The data points correspond to spectral types from B0.5 to O3 stars, taken from Sternberg et al. (2003). The curve is a cubic polynomial fit.

symmetry. The solutions to these equations give the vertical density and pressure profiles of the gaseous structure.

Most of the content of this chapter can be found in the paper by Rodríguez-Ramírez & Raga (2016).

4.1 The radiation pressure forces

4.1.1 Luminosity and ionising photon rate from a stellar population

In this subsection we present some general considerations on the luminosity and the ionising photon rate produced by a stellar population. These are then used in the following subsections to derive the radiation pressure force on the gas due to dust absorption and photoionization processes.

The total luminosity L_{tot} of a stellar population with lower and upper masses

M_1 and M_2 (respectively) is

$$L_{tot} = \int_{M_1}^{M_2} L(M)\xi(M)dM, \tag{4.1}$$

where

$$\frac{L}{L_\odot} = \left(\frac{M}{M_\odot}\right)^p, \tag{4.2}$$

is the mass-luminosity relation for a single star, with $p = 3.5$ normally used for main sequence stars, and $\xi(M)$ is the Salpeter initial mass function

$$\xi(M) = \xi_0 M^{-\alpha}, \tag{4.3}$$

with $\alpha = 2.35$ (Salpeter 1955), which gives the number of stars as a function of mass, for a stellar population. Given the total mass M_{tot} of the stellar population, the factor ξ_0 in the mass function of equation (4.3) can be obtained through the normalisation condition

$$M_{tot} = \int_{M_1}^{M_2} M\,\xi(M)dM. \tag{4.4}$$

Then, from equations (4.1)-(4.4) we obtain the total luminosity as a function of the total mass and the lower and upper masses of the stellar population:

$$L_{tot} = M_{tot} L_\odot \Omega_1(M_1, M_2), \tag{4.5}$$

where

$$\Omega_1\left(M_1, M_2\right) = \left(\frac{\alpha - 2}{p + 1 - \alpha}\right) \frac{\left(M_1 M_2\right)^{\alpha-2}}{M_\odot^p} \left(\frac{M_2^{p+1-\alpha} - M_1^{p+1-\alpha}}{M_2^{\alpha-2} - M_1^{\alpha-2}}\right). \tag{4.6}$$

If we consider an upper mass $M_2 = 56.6$ $\mathrm{M}_\odot$ (corresponding to O5 stars), and a lower mass $M_1 = 0.1$ $\mathrm{M}_\odot$ (corresponding to M8 stars), we then obtain

$$\Omega_1(M_1, M_2) = 4.788 \times 10^2\,\mathrm{M}_\odot^{-1}. \tag{4.7}$$

The total rate of ionising photons $S_{*,tot}$ of the stellar population can be calculated

as

$$S_{*,tot} = \int_{M_1}^{M_2} S_*(M)\xi(M)dM, \tag{4.8}$$

where $S_*(M)$ is the ionising photon rate (of a single star) as a function of stellar mass. We obtain this function through a cubic fit to the data of Sternberg et al. (2003) for the ionising photon rates of B0.5 to O3.5 stars:

$$\frac{S_*}{S_{*,B0.5}} = k_1\left(\frac{M}{M_\odot}\right) + k_2\left(\frac{M}{M_\odot}\right)^2 + k_3\left(\frac{M}{M_\odot}\right)^3, \tag{4.9}$$

where

$$k_1 = -0.7151, \quad k_2 = 0.0405, \quad k_3 = -0.00015. \tag{4.10}$$

and $S_{*,B0.5} = 5.128 \times 10^{47}$ s^{-1} is the ionising photon rate of a B0.5 star. The values obtained by Sternberg et al. (2003) and our polynomial fit are shown in Figure 4.1. From this Figure we see that stars later than B0.5 have negligible ionising photon rates. Therefore, in equation (4.8) we use the mass $M_{B0.5} = 19.3$ M$_\odot$ as a lower limit. Together with equations (4.3), (4.4) and (4.9), we then obtain

$$S_{*,tot} = M_{tot} S_{*,B0.5} \Omega_2(M_1, M_2), \tag{4.11}$$

where

$$\begin{aligned}
&\Omega_2(M_1, M_2) = \\
&(\alpha - 2)\left[\frac{(M_1 M_2)^{\alpha-2}}{M_2^{\alpha-2} - M_1^{\alpha-2}}\right]\left[\frac{k_1}{M_\odot}\frac{M_2^{2-\alpha} - M_{B0.5}^{2-\alpha}}{2-\alpha} + \right. \\
&\left.\frac{k_2}{M_\odot^2}\frac{M_2^{3-\alpha} - M_{B0.5}^{3-\alpha}}{3-\alpha} + \frac{k_3}{M_\odot^3}\frac{M_2^{4-\alpha} - M_{B0.5}^{4-\alpha}}{4-\alpha}\right].
\end{aligned} \tag{4.12}$$

Using the values of M_1, M_2 and α given above, we finally obtain:

$$\Omega_2(M_1, M_2) = 2.554 \times 10^{-2} \mathrm{M}_\odot^{-1}. \tag{4.13}$$

We apply the results obtained in equations (4.5) and (4.11) to calculate the momentum fluxes associated with the total luminosity and with the ionising photon flux for a stellar distribution. Let us consider an ensemble of stars uniformly dis-

tributed in an infinite plane (the xy-plane), with a constant mass per unit area Σ_*. In this idealised configuration, the momentum flux F_L (momentum per unit time per unit area) due to the light of the stars points in the z-direction. Therefore, we assume that the momentum flux satisfies a Gauss law:

$$\oint_{\delta S} F_L \hat{z} \cdot d\hat{a} = \frac{L_{tot}}{c}, \tag{4.14}$$

which means that the total momentum flux integrated over a surface δS (enclosing a volume V) is equal to the total stellar light momentum rate produced inside the volume V. If we now consider a control box enclosing an area A of the stellar plane, with top and bottom faces parallel to the plane, we can trivially integrate equation (4.14) to obtain (together with equation 4.5)

$$F_L = \frac{\Sigma_*}{2c} L_\odot \Omega_1(M_1, M_2), \tag{4.15}$$

where we have substituted $A\Sigma_*$ in equation (4.5) as the total stellar mass inside the box. In the same way we calculate the flux of ionising photons F_i over the stellar plane by using the condition

$$\oint_{\delta S} F_i \hat{z} \cdot d\hat{a} = S_{*,tot}, \tag{4.16}$$

where $S_{*,tot}$ is the total rate of ionising photons produced inside the enclosing surface. Applying again the control box, together with equation (4.11) we obtain

$$F_i = \frac{\Sigma_*}{2} S_{*,B0.5} \Omega_2 \left(M_1, M_2\right). \tag{4.17}$$

In the next subsection we apply the fluxes obtained in equations (4.15) and (4.17) for deriving the radiation pressure forces on the gas layer surrounding the plane of the stellar distribution.

4.1.2 Radiation pressure by dust absorption

Cosmic dust grains present in the ISM absorb the stellar radiation field, receiving a deposition of outward directed momentum. If the dust is dynamically coupled with the gas, this momentum is transferred to the gaseous component. Under this

assumption of perfect coupling, the radiation pressure resulting from dust absorption of the radiation emitted by a stellar (point) source can be written as:

$$\bar{f}_{d,r} = n(R)\sigma_d \frac{L}{4\pi c R^2}\ \hat{r}, \tag{4.18}$$

where R is the distance from the star, $n(R)$ is the (radially dependent) total H density, σ_d is the cross section of the dust grains per H nucleon (which we consider to be frequency-independent) L is the stellar luminosity, c is the speed of light and $\hat{r}$ is the radial unit vector. For deriving this equation, we have assumed that the dust is optically thin (so that only the geometrical dilution of the stellar radiation field has to be considered).

We can see in equation (4.18) that the radiation pressure is the product of the momentum flux at a radius R, with the gas number density n and with the dust cross section σ_d. For a planar distribution of stellar sources, the radiation pressure at a height z (above the planar stellar distribution) is

$$\bar{f}_{d,z} = n(z)\sigma_d F_L\ \hat{z}, \tag{4.19}$$

i.e., the product of the momentum flux F_L of the radiation from the stars on the plane (see equation 4.15), with the dust cross section per unit H nucleon σ_d, and with the gas density $n(z)$.

Substituting equation (4.15) into (4.19) we then obtain the radiation pressure due to dust absorption in planar geometry:

$$\bar{f}_{d,z} = \frac{\Sigma_*}{2c} L_\odot \Omega_1(M_1, M_2)\sigma_d n(z)\ \hat{z}, \tag{4.20}$$

where $\Omega_1(M_1, M_2)$ is given by equation (4.6).

In Section 4.2 we will use this approximation for the radiation pressure due to dust absorption as a component of the hydrostatic balance equation of the gas.

4.1.3 Radiation pressure due to photoionization processes

The ionisation state of the gas in HII regions is generally very close to photoionization equilibrium. In photoionization processes, the atoms receive momentum from the ionising photons, resulting in an outward directed radiation pressure on the

gas. Raga et al. (2015a) have included this radiation pressure term in models of self-gravitating, isothermal spheres. These authors use a "grey approximation" (i.e., setting the photoionization cross section of H equal to the Lyman limit cross section) to obtain:

$$\bar{f}_{H,r} = n_{HI}\phi_H \frac{h\nu_0}{c}\,\hat{r}, \tag{4.21}$$

where n_{HI} is the neutral H number density, h is the Planck constant, ν_0 is the Lyman limit frequency and

$$\phi_H = \sigma_{\nu_0} F \tag{4.22}$$

is the H photoionization rate, with F being the flux (number of photons per unit time) of the impinging, ionising photons.

In a plane-parallel configuration, the radiation pressure associated with the photoionization processes will then be

$$\bar{f}_{H,z} = n_{HI}(z)\phi_H \frac{h\nu_0}{c}\,\hat{z}, \tag{4.23}$$

which is independent of the x, y coordinates and points outwards from the $z = 0$ plane.

We now write the photoionization equilibrium for H:

$$n_{HI}\phi_H = n_e n_{HII}\alpha_B(T_i) \simeq n^2(z)\alpha_B(T_i), \tag{4.24}$$

where $\alpha_B(T_i)$ is the case B recombination coefficient of H (evaluated at the temperature $T_i \simeq 10^4$ K of the ionised gas), and n_{HII} and n_e are the ionised H and the electron number densities, respectively. For the second equality, we set $n_{HII} \simeq n_e \simeq n$, as appropriate for the almost fully ionised H within the H II region. Finally, combining equations (4.22)-(4.24) we obtain the radiation pressure due to photoionization of H,

$$\bar{f}_{H,z} = \frac{h\nu_0}{c}\alpha_B(T) n^2(z)\,\hat{z}, \tag{4.25}$$

which depends on the square of the total H number density. This expression is basically the same as that obtained for the spherical case (see Raga et al. 2015a), with the difference that in the plane-parallel case the number density depends on the vertical coordinate z, and the force points in the z-direction.

It should be pointed out that the radiation pressure force given in equation (4.25) could be only applied inside the zone where the gas is fully ionised, i. e., within the "Strömgren height" z_S. This outer boundary of the photoionized region can be calculated through the balance of ionising photons and recombinations (per unit area and time) within the slab:

$$\int_0^{z_S} \alpha_B(T) n^2(z) dz = F_i, \tag{4.26}$$

where F_i is the flux of ionising photons from the stellar plane (see equation 4.17). Therefore, the Steömgren height satisfies the condition

$$\int_0^{z_S} n^2(z) dz = \frac{\Sigma_*}{2\alpha_B(T)} S_{*,B0.5} \Omega_2(M_1, M_2)\,. \tag{4.27}$$

In the following section we derive a hydrostatic balance equation, considering the radiation pressure forces given by equations (4.20) and (4.25), the gravitational forces and the pressure gradient force of the gas. This equation has to be integrated to obtain the $n(z)$ density stratification needed to calculate the Strömgren height (see equation 4.27).

4.2 The model equations

To model the density and pressure structure of the gas surrounding the stellar plane, we assume planar symmetry. Therefore, the solution only depends on the z coordinate, and is symmetric with respect to the xy-plane (i.e., the plane of the stellar distribution). We first consider the layer where the gas is fully photoionized by the stars in the plane, within which dust can also be present.

In this region, the gas pressure gradient is balanced by the inward gravitational force and the outwards radiation pressure gradient force:

$$\begin{aligned} \frac{dP}{dz} = &- \left(\frac{d\Phi}{dz} + 2\pi G \Sigma_* \right) \rho \\ &+ \frac{\sigma_{d,i} \Sigma_* L_\odot \Omega_1(M_1, M_2)}{2c\mu m_H} \rho + \frac{h\nu_0 \alpha_B(T)}{c(\mu m_H)^2} \rho^2, \end{aligned} \tag{4.28}$$

where P is the pressure, ρ the density, G the gravitational constant, m_H the mass of

H, $\mu = 1.3$ (for a gas with a H abundance of 0.9 and a He abundance of 0.1) and $\sigma_{d,i}$ is the cross section of the dust grains in this photoionized zone (which we will consider with lower values than the cross section of the dust grains in the covering neutral layer). The terms in parentheses in the RHS of this equation are the gravitational components, being Φ the gravitational potential of the self-gravitating gas, which satisfies the Poisson equation

$$\frac{d^2\Phi}{dz^2} = 4\pi G\rho\,. \tag{4.29}$$

The $2\pi G\Sigma_*$ term (see equation 4.28) is the constant gravitational field due to the mass of the stars on the plane, being Σ_* the stellar mass per unit area. The two last terms in the RHS of equation (4.28) are the radiation pressure forces due to dust absorption and photoionization of H given by equations (4.20) and (4.25), respectively.

We assume that the photoionized region is approximately isothermal, so that

$$P = a_i^2\rho, \tag{4.30}$$

being a_i the isothermal speed of sound of the ionised gas given by

$$a_i = \sqrt{\frac{2kT_i}{\mu m_H}}, \tag{4.31}$$

where k is the Boltzmann constant, and we take $T_i \approx 10^4$ K for the temperature of the ionised zone. We combine equations (4.28)-(4.30) to obtain a second order equation for the gas density:

$$\frac{d}{dz}\left(\frac{1}{\rho}\frac{d\rho}{dz}\right) = -\frac{4\pi G}{a_i^2}\rho + \frac{h\nu_0\alpha_B(T)}{a_i^2 c(\mu m_H)^2}\frac{d\rho}{dz}, \tag{4.32}$$

with the boundary conditions at $z = 0$:

$$\rho(0) = \rho_c, \tag{4.33}$$

$$\frac{d\rho}{dz}(0) = \left(\frac{\sigma_{d,i}L_\odot\Omega_1(M_1,M_2)}{2c\mu m_H} - 2\pi G\right)\frac{\Sigma_*\rho_c}{a_i^2} + \frac{h\nu_0\alpha_B(T)}{a_i^2 c(\mu m_H)^2}\rho_c^2, \tag{4.34}$$

where ρ_c is the gas density on the stellar plane. Also,

$$\frac{d\Phi}{dz}(0) = 0\,.$$

The forces due to the gravity of the stellar mass and the radiation pressure on dust disappear when deriving the second order equation (4.32), since both are proportional to the gas density. Their effect appears only in the boundary condition of equation (4.34).

The model equation (4.32) is valid when the radiation pressure due to photoionization of H is present, i. e., inside the Strömgren height z_S given by equation (4.27). Beyond the Strömgren height z_S, the gas is neutral, the flux of ionising photons is close to zero, and there is no radiation pressure due to photoionization of H. However, photons with frequencies lower than the Lyman limit penetrate the neutral region, so that we still have the radiation pressure associated with dust absorption. Therefore, for $z > z_s$ the hydrostatic balance equation is:

$$\frac{dP}{dz} = -\left(\frac{d\Phi}{dz} + 2\pi G\Sigma_*\right)\rho + \frac{\Sigma_* L_\odot \sigma_d \Omega_1(M_1, M_2)}{2c\mu m_H}\rho \tag{4.35}$$

where σ_d is the cross section (per atom) of the dust grains in the neutral environment. In equation (4.35), the pressure and density follow the relation

$$P = a_n^2 \rho, \tag{4.36}$$

where a_n is the isothermal sound speed

$$a_n = \sqrt{\frac{kT_n}{\mu m_H}}\,, \tag{4.37}$$

where $T_n \approx 10^3$ K is the temperature of the neutral medium.

In equation (4.35) we are assuming that the stellar flux producing radiation pressure on dust is still optically thin (see equation 4.18 and section 2.2). This is clearly not the case for the photons with frequencies larger than the Lyman limit (i.e., the ionising photons), which have all been absorbed by the $z < z_S$ region (see above). However, the ratio of non-ionising to ionising luminosity in a cluster of O and B stars is $L_n/L_i \sim 5$ (see Draine 2011), and the ratio of ionisig luminosity to

the total luminosity is $L_i/L_* \sim 1/6$. Thus, we can assume that the ionising photons have a small contribution to the total stellar luminosity (which acts on the dust grains).

Combining (4.35) with equation (4.29), we then write the model equation for the $z > z_S$ zone:

$$\frac{d}{dz}\left(\frac{1}{\rho}\frac{d\rho}{dz}\right) = -\frac{4\pi G}{a_n^2}\rho. \tag{4.38}$$

The boundary conditions of equation (4.38), are determined by the pressure balance between the ionised and neutral components at $z = z_S$:

$$\rho(z_S) = \rho_{S,n} = \left(\frac{a_i}{a_n}\right)^2 \rho_{S,i} = 2\frac{T_i}{T_n}\rho_{S,i}, \tag{4.39}$$

where $\rho_{i,S}$ is the gas density of the photoionized zone given by the solutions of equation (4.32) at z_S, and ρ_{n_S} is the density of the neutral zone at z_S. The boundary condition on the derivative of equation (4.38) at z_S is

$$\begin{aligned}\frac{d\rho}{dz}(z_S) = &\left(\frac{L_\odot \sigma_d \Omega_1(M_1, M_2)}{2c\mu m_H} - 2\pi G\right)\frac{\Sigma_* \rho_{n,S}}{a_n^2} \\ &- \frac{4\pi G \rho_{n,S}}{a_n^2}\int_0^{z_S} \rho\, dz,\end{aligned} \tag{4.40}$$

which is obtained by taking the $z \to z_S^+$ limit of equation (4.35). The integral of equation (4.40) corresponds to the integration from 0 to z_s of the Poisson equation (4.29) for the gravitational potential, where the density ρ inside the integral operator is the solution of the model equation (4.32) for $z \leq z_S$.

If we consider the gas density on the stellar plane ($z = 0$)

$$\rho_c = \rho(0), \tag{4.41}$$

as the characteristic density, and define the characteristic height

$$z_0 = \frac{a_i}{\sqrt{8\pi G \rho_c}}, \tag{4.42}$$

where a_i is the isothermal sound speed of the ionised region given by equation (4.31), we can write the model equations (4.32) and (4.38) with their corresponding

boundary conditions in dimensionless form as

$$\frac{d}{ds}\left(\frac{1}{\varrho}\frac{d\varrho}{ds}\right) = -\frac{1}{2}\varrho + \lambda\frac{d\varrho}{ds}, \tag{4.43}$$

$$\varrho(0) = 1, \tag{4.44}$$

$$\frac{d\varrho}{ds}(0) = \lambda + \varepsilon_i, \tag{4.45}$$

$$\int_0^{s_S} \varrho^2\, ds = \delta, \tag{4.46}$$

for $0 \leq s \leq s_S$, and

$$\frac{d}{ds}\left(\frac{1}{\varrho}\frac{d\varrho}{ds}\right) = -\frac{T_i}{T_n}\varrho, \tag{4.47}$$

$$\varrho(s_S) = 2\frac{T_i}{T_n}\varrho_{S,i}, \tag{4.48}$$

$$\frac{d\varrho}{ds}(s_S) = \left(2\frac{T_i}{T_n}\right)^2 \varrho_{S,i}\left(\varepsilon - \frac{1}{2}\int_0^{s_S} \varrho\, ds\right), \tag{4.49}$$

for $s > s_S$, where $s = z/z_0$, $\varrho = \rho/\rho_c$, $s_S = z_S/z_0$, $\varrho_{i,S} = \rho_{i,S}/\rho_c$ and λ, δ, ε, and ε_i are dimensionless parameters defined by

$$\lambda = \frac{\alpha_B(T_i) h\nu_0}{a_i c(\mu m_H)^2}\sqrt{\frac{\rho_c}{8\pi G}}, \tag{4.50}$$

$$\delta = \frac{(\mu m_H)^2 S_{*,B0.5}\Omega_2(M_1, M_2)}{2a_i\alpha_B(T)}\Sigma_*\sqrt{\frac{8\pi G}{\rho_c^3}}, \tag{4.51}$$

$$\varepsilon = \left(\frac{\sigma_d L_\odot \Omega_1(M_1, M_2)}{2c\mu m_H} - 2\pi G\right)\frac{\Sigma_*}{a_i\sqrt{8\pi G\rho_c}}, \tag{4.52}$$

$$\varepsilon_i = k\varepsilon, \quad \text{with } k = \frac{\sigma_{d,i} L_\odot \Omega_1/(4\pi\mu m_H cG) - 1}{\sigma_d L_\odot \Omega_1/(4\pi\mu m_H cG) - 1}. \tag{4.53}$$

The dimensionless parameter λ characterises the effect on the density structure of the radiation pressure due to photoionisation of H. On the other hand, the dimensionless parameter ε characterises the effect of the radiation pressure due to dust absorption and the gravity due to the stellar mass (both of these forces being proportional to the gas density, see equation 4.28) in the neutral gas, and the ε_i parameter characterises the same effects but in the photoionized zone. Finally, the dimensionless parameter δ determines the dimensionless Strömgren height s_S through equation

(4.46), which gives the size of the photoionized region and the boundary conditions of the dimensionless model equation (4.47) for the neutral region.

To obtain the values of the dimensionless parameters (4.50)-(4.53), and the boundary conditions of equations (4.43) and (4.47), we consider as fixed the typical values of $T_i = 10^4$ K and $T_n = 10^3$ K for the temperatures of the photoionized and neutral regions, giving isothermal sound speeds $a_i = 11$ km s^{-1} and $a_n = 2.5$ km s^{-1} from equations (4.31) and (4.37), respectively. We also take the typical value for the dust absorption cross section of $\sigma_d = 10^{-21}$ cm^2 H^{-1} for the neutral gas (see Draine 2011). Finally, we consider the values given in section 2.1 for the lower and upper masses M_1 and M_2 of the stellar population, which determine the values of Ω_1 and Ω_2 (see equations 4.6 and 4.12).

Therefore, the λ parameter basically depends on the central density ρ_c (see equation 4.50) and the δ parameter depends on ρ_c and Σ_* (see equation 5.37). The ε parameter depends basically on the values of ρ_c and Σ_* (see equation 4.52), and the ε_i parameter depends on the ε parameter (see equation 4.53). In this way, only two of the dimensionless parameters given in equations (4.50)-(4.53) are independent. Combining equations (4.50)-(4.52), we can write the ε parameter as

$$\varepsilon = \left(\frac{\sigma_d L_\odot \Omega_1}{2c\mu m_H} - 2\pi G\right)\left(\frac{2}{S_{*,B0.5}\Omega_2\alpha_B}\right)\left(\frac{a_i c\mu m_H}{h\nu_0}\right)^2 \delta\lambda^2, \tag{4.54}$$

where it can be seen that this parameter depends only on the possible values of λ and δ, since we consider all the factors in parentheses of RHS of equation (4.54) as fixed quantities, given by the typical values that we mention above.

Finally, to obtain the ε_i parameter as a function of the ε parameter, we set up the values of the constant k in equation (4.53) as follows. We consider three possible cross sections $\sigma_{d,i}$ for the dust grains in the photoionized region, of the form

$$\sigma_{d,i} = \ell\sigma_d, \quad \ell = \begin{cases} 1 \\ 1/2 \\ 0, \end{cases} \tag{4.55}$$

i. e., that $\sigma_{d,i}$ is the same as the cross section of dust grains of the neutral layer, half of this value, or zero. Therefore, combining equations (4.55) and (4.53) we obtain

three values of the k constant:

$$k = \begin{cases} k_1 = 1 \\ k_{1/2} = 0.469 \\ k_0 = -0.061. \end{cases} \tag{4.56}$$

In this way we build a model for the structure of a photoionized slab covered by a neutral layer where, by specifying the values of the free dimensionless parameters λ and δ, we can obtain three associated solutions of the dimensionless equations (4.43) and (4.47), labelled as

$$(\lambda, \delta) \rightarrow \left(\varrho_{\lambda\delta}^{k_1}(s),\ \varrho_{\lambda\delta}^{k_{1/2}}(s),\ \varrho_{\lambda\delta}^{k_0}(s) \right). \tag{4.57}$$

In order to estimate the range of the possible values of the λ and δ parameters we first consider a central number density of the photoionized zone of $n_c = \rho_c/(\mu m_H) = 10$ cm^{-3}, corresponding to supergiant HII regions observed in external galaxies, which are the mature state of expanding HII regions (see Kurtz & Franco 2002). We also consider a stellar mass per unit area of the galactic plane of $\Sigma_* = 20$ M$_\odot$ pc^{-2}, which is the typical stellar surface density beyond the middle radius of the galaxies measured by Leroy et al. (2008). Then, we obtain the following values for our λ and δ dimensionless parameters:

$$\lambda = 0.126 \left(\frac{n_c}{10 \text{ cm}^{-3}} \right)^{1/2}, \tag{4.58}$$

$$\delta = 2.851 \left(\frac{\Sigma_*}{20 \text{ M}_\odot \text{pc}^{-2}} \right) \left(\frac{10 \text{ cm}^{-3}}{n_c} \right)^{3/2}. \tag{4.59}$$

Using these values in equation (4.54) we obtain $\varepsilon = 4.183$.

If we now consider an enhanced value for the central number density $n_c = 100$ cm^{-3}, (which corresponds to classical HII regions, see Kurtz & Franco 2002), we obtain $\lambda = 0.401$ and $\delta = 0.09$, which gives $\varepsilon = 1.322$ for the neutral covering layer.

Of course, we could also consider different values of Σ_* from which one could obtain more combinations of the λ and δ parameters. Therefore, in the following section we will explore the solutions of equations (4.43) and (4.47) corresponding to the possible combinations of the free dimensionless parameters in the parametric

domain $\lambda \in [0.1, 0.5]$ and $\delta \in [0.1, 10]$.

4.3 Solutions of the model equations

To obtain the density distribution of gas above the stellar plane we integrate equations (4.43) and (4.47) as follows. Given fixed values of the λ and δ parameters, we first calculate the value of the ε parameter with equation (4.38), and then we obtain the values of the three associated parameters ε_i through equations (4.53) and (4.56). Therefore we set up three pairs of boundary conditions, given by equations (4.44)-(4.45). We then integrate numerically equation (4.43) obtaining three curves for the dimensionless density ϱ as a function of the dimensionless height s, for the photoionized layer. Each numerical integration is performed until the corresponding condition (4.46) is satisfied, when we attain the dimensionless Strömgren height s_S and the corresponding density ϱ_S.

We are then able to set up three pairs of boundary conditions, given by equations (4.48)-(4.49), in order to integrate equation (4.47), corresponding to the neutral region ($s > s_S$), in which the radiation pressure due to dust absorption is still present. We obtain the solutions for this neutral zone analytically as follows.

Integrating equation (4.47) from s_S to s ($> s_S$) together with conditions (4.48) and (4.49) we obtain

$$\frac{1}{\varrho}\frac{d\varrho}{ds} = \left(2\frac{T_i}{T_n}\right)\left(\varepsilon' - \frac{1}{2}\int_{s_S}^{s} \varrho\, ds\right), \tag{4.60}$$

where

$$\varepsilon' \equiv \varepsilon - \frac{1}{2}\int_{0}^{s_S} \varrho\, ds. \tag{4.61}$$

If we now define the column density m as

$$m = \int_{s_S}^{s} \varrho\, ds, \tag{4.62}$$

the differential operator becomes $d/ds = \varrho\, d/dm$, and we can write equation (4.60) in the form

$$\frac{d\varrho}{dm} = \left(2\frac{T_i}{T_n}\right)\left(\varepsilon' - \frac{1}{2}m\right), \tag{4.63}$$

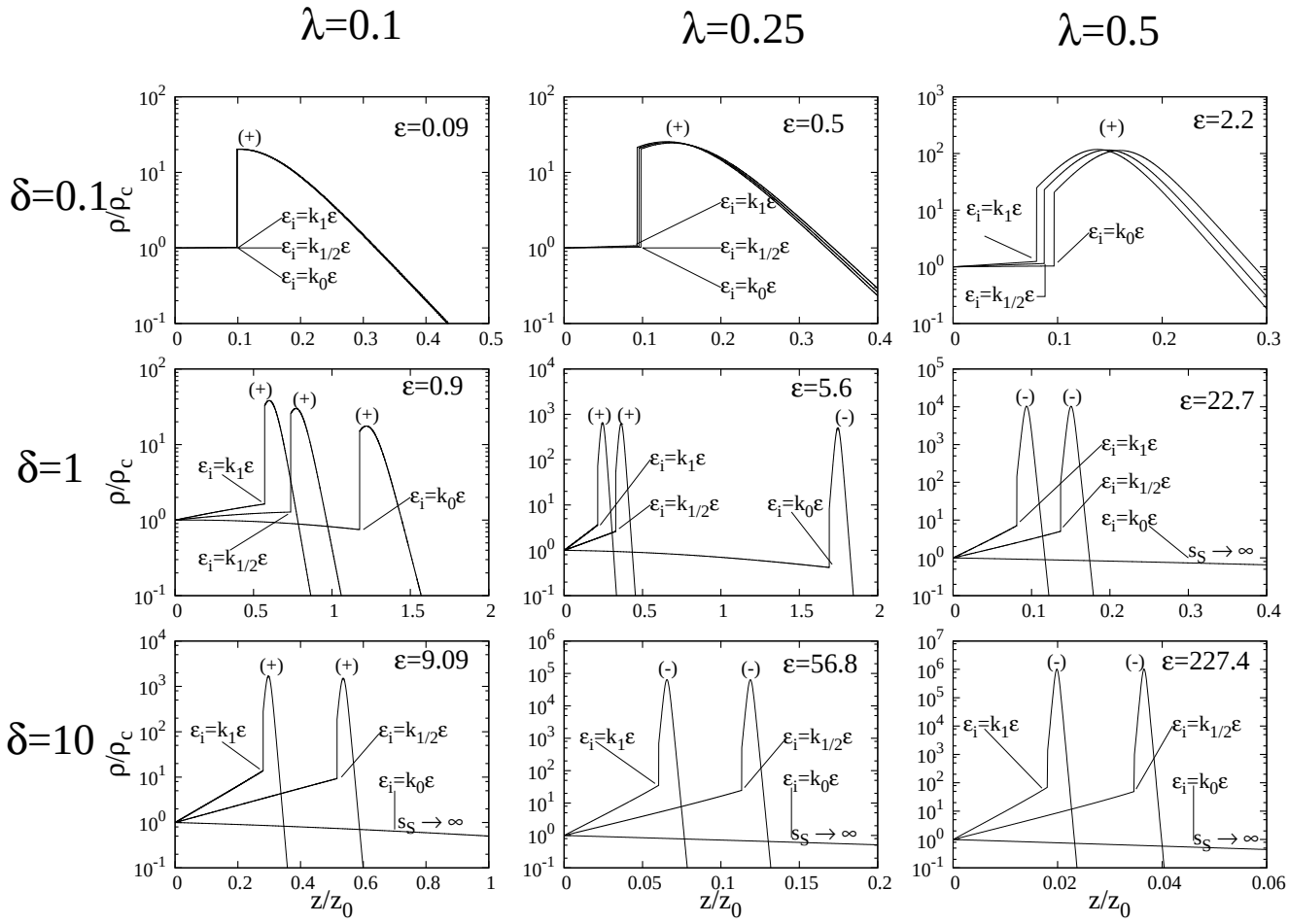

Figure 4.2: Stratifications of the dimensionless gas density as a function of the dimensionless height above the stellar plane. The stratifications are solutions of equations (4.43) and (4.47), which model the structure a planar HII region covered by a neutral gas layer. In each graph, the solutions are calculated by specifying the values of the free dimensionless parameters λ and δ of the model developed in the text. The value of the λ parameter is given in the top of its corresponding column, and the value of the δ parameter is given at the beginning of the corresponding rows. For each model, we obtain a triad of solutions, associated to the specific values of λ and δ. Each curve of the triad corresponds to a different fraction (0, 1/2 and 1) of the dust cross section in the photoionized layer, relative to the dust cross section of its corresponding neutral covering layer (see equations 4.53, 4.55 and 4.56). We label each curve with its corresponding fraction with a line that indicates the limit of the photoionized region, where there is a "jump" in the density. In some curves this limit is not finite, and these cases are indicated with a " $s_S \to \infty$" label. We also label the solutions with gravitationally unstable neutral layers with a "(-)" and the stable solutions with a "(+)" (see section 5).

which can be integrated to obtain

$$\varrho = \left(2\frac{T_i}{T_n}\right)\left(\varrho_{S,i} + \varepsilon' m - \frac{1}{4}m^2\right), \tag{4.64}$$

where $\varrho_{S,i}$ is the density of the ionised gas at the Strömgren height obtained by solving equations (4.43)-(4.46). From equation (4.64) we obtain m as a function of s by substituting the derivative with respect to s of equation (4.62) and integrating from s_S to s, obtaining

$$\begin{aligned} m =& 2\sqrt{\varrho_{S,i} + \varepsilon'^2} \\ & \times \tanh\left\{\left(\frac{2T_i}{T_n}\right)\frac{\sqrt{\varrho_{S,i} + \varepsilon'^2}}{2}(s - s_S) - \beta\right\} + 2\varepsilon', \end{aligned} \tag{4.65}$$

where

$$\beta \equiv \tanh^{-1}\left(\frac{\varepsilon'}{\sqrt{\varrho_{S,i} + \varepsilon'^2}}\right). \tag{4.66}$$

Finally, to obtain ϱ as a function of s, we just take the derivative with respect to s of equation (4.65), obtaining

$$\begin{aligned} \varrho =& \left(\frac{2T_i}{T_n}\right)\left(\varrho_{S,i} + \varepsilon'^2\right) \\ & \times \operatorname{sech}^2\left\{\left(\frac{2T_i}{T_n}\right)\frac{\sqrt{\varrho_{S,i} + \varepsilon'^2}}{2}(s - s_S) - \beta\right\}. \end{aligned} \tag{4.67}$$

In Figure 4.2 we show an array of nine graphs where we plot the solutions of equations (4.43) and (4.47) described above. The solutions in each graph are obtained for particular values of the λ and δ parameters, according to their position in the array. The graphs in each row share the same value of the δ parameter (δ = 0.1, 1, and 10). The graphs in each column share the same value of the λ parameter (λ = 0.1, 0.25 and 0.5).

In each graph we show the value of the corresponding ε parameter (which measures the importance of the radiation pressure on dust grains relative to the gravitational forces in the neutral layer, see equation 4.52), calculated as a function of λ and δ (see equation 4.54). The three curves in each graph correspond to the three values of the ε_i parameter, as fractions of the ε parameter, given by equation (4.56)

(which considers three different dust cross sections for the photoionized layer, see equations 4.53 and 4.55).

The outer boundary of the photoionized region, given by condition (4.46), can be seen as a discontinuity in the solutions, with a finite jump in the dimensionless density ϱ at the Strömgren height s_S. We indicate this limit with a line, connected to the value of its corresponding ε_i parameter.

However, we also find some solutions which do not exhibit such a discontinuity because $s_S \to \infty$. In these solutions, the stars in the plane are able to photoionise all of the surrounding gas. This is the case of the $\delta = 10$ row, and the graph corresponding to $\lambda = 0.5$, $\delta = 1$. In these solutions we observe a transition where the Strömgren height of the curves is finite as $\varepsilon_i \to \varepsilon$, i. e., as the cross section of dust grains in the photoionized zone tends to the standard dust cross section (i.e. σ_d, see equations 4.53, 4.55 and 4.56).

A different behaviour of the solutions is observed in the $\delta = 0.1$ row of Figure 4.2. The density distributions of the photoionized zones of the solutions in this row are practically flat, and the neutral zones of these solutions are spatially dominant. Also, there is no significant difference between the curves with different fractions k_0, $k_{1/2}$ and k_1 of the corresponding ε parameter.

Finally, the families of solutions given by the combination of parameters ($\lambda = 0.5, \delta = 1$), ($\lambda = 0.25, \delta = 10$) and ($\lambda = 0.5, \delta = 10$) (below the central diagonal of the array), are beyond the validity of the planar approximation assumed in this model. This is simply because these pairs of parameters imply a stellar surface density $\Sigma_* > 400$ $\mathrm{M}_\odot$ pc^{-2}, which can be found only in the centre of typical spiral galaxies (see Leroy et al. 2008), for which a spherical model would be more appropriate.

4.3.1 The full neutral solution

If we consider a low Σ_* for the stellar population (e.g., in a low-mass star formation region), we can see from equation (4.17) that the flux of ionising photons produced by the stars in the plane is not an important effect to be considered in the hydrostatic model of the gas slab. Therefore, we can assume that the gas slab is completely neutral, but is still under the effects of the radiation pressure due to dust absorption, the gravity of the stars and the self-gravity of the gas. This regime is modelled by

the analytical solutions of equation (4.67) in the $s_S \to 0$ limit, which can be written as

$$\frac{\rho}{\rho_{c,n}} = \left(1+\tilde{\varepsilon}^2\right) \operatorname{sech}^2 \left\{ \frac{\sqrt{1+\tilde{\varepsilon}^2}}{2} \left(\frac{z}{z_{0,n}}\right) - \tilde{\beta} \right\} \tag{4.68}$$

where $\rho_{c,n}$ is the density of the neutral gas at $z = 0$ and

$$z_{0,n} = \frac{a_n}{\sqrt{8\pi G \rho_{c,n}}} \tag{4.69}$$

$$\tilde{\varepsilon} = \left(\frac{\sigma_d L_\odot \Omega_1(M_1, M_2)}{2c\mu m_H} - 2\pi G \right) \frac{\Sigma_*}{a_n \sqrt{8\pi G \rho_{c,n}}}, \tag{4.70}$$

$$\tilde{\beta} = \tanh^{-1} \left\{ \frac{\tilde{\varepsilon}}{\sqrt{1+\tilde{\varepsilon}^2}} \right\}. \tag{4.71}$$

The density profiles given by equation (4.68) are determined by the $\tilde{\varepsilon}$ dimensionless parameter, which characterises the effect of the radiation pressure due to dust absorption and the gravity of the stellar population in the plane. If we consider a $\Sigma_* = 1$ M$_\odot$ pc^{-2} stellar surface density and a central number density $n_{c,n} = 10$ cm^{-3} of the HI gas, we obtain

$$\tilde{\varepsilon} = 0.935 \left(\frac{\Sigma_*}{1 \text{ M}_\odot \text{ pc}^{-2}} \right) \left(\frac{n_{c,n}}{10 \text{ cm}^3} \right)^{-1/2}, \tag{4.72}$$

and if we do not consider the presence of dust grains (i. e., $\sigma_d = 0$), the $\tilde{\varepsilon}$ parameters only characterises the gravitational field due to the stars, giving $\tilde{\varepsilon} = -0.057$.

If we substitute $\tilde{\varepsilon} = 0$ in equation (4.68), we obtain the standard solution for the isothermal Lane-Emden equation in planar geometry (see Ledoux 1951), which models the density of a slab under the effect of the self-gravity of the gas.

In Figure 4.3, we plot the resulting curves given by the solution of equation (4.68), for different values of the $\tilde{\varepsilon}$ parameter enclosing the values estimated above. For $\tilde{\varepsilon} > 0$, the solutions are density profiles that reach a maximum above the stellar plane, of the same order of magnitude as the central density. In the region where the self-gravity of the gas dominates the solutions, the density decays exponentially. For $\tilde{\varepsilon} < 0$ the solutions have their highest value at $z = 0$ and rapidly acquire an exponentially decaying behaviour.

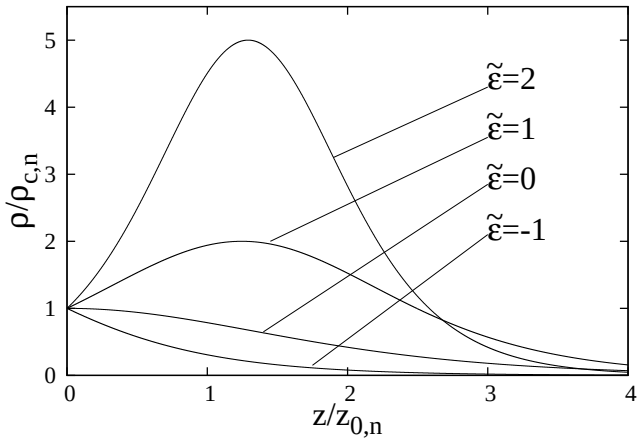

Figure 4.3: Dimensionless density as a function of the dimensionless height above the stellar plane of the fully neutral regime described in subsection 4.1. Each curve is obtained with the analytical solution (4.68), characterised by a particular value of the dimensionless parameter $\tilde{\varepsilon}$, which measures the effect of the radiation pressure on dust grains, relative to the gravity of the stars in the plane.

4.4 The gravitational stability of the neutral layers

For some configurations of the λ and δ parameters, the resulting density profiles generate highly dense neutral covering layers. As we can see from Figure 4.2, these solutions have density peaks several orders of magnitude larger than the central density ρ_c of their corresponding ionised region. This behaviour is found in solutions where the ionised region is more extended than the neutral layer. The question therefore arises of whether or not such hydrostatic configurations are likely to occur, since they could be unstable to gravitational collapse.

To assess the stability of the neutral regions, we consider them to be unstable to gravitational collapse if

$$Q \equiv \frac{\lambda_c}{\Delta z} = \frac{a_n}{\Delta z}\sqrt{\frac{2\pi}{\rho_{peak} G}} < 1, \tag{4.73}$$

where λ_c is the critical Jeans wavelength for a self-gravitating gas slab (see Ledoux 1951), a_n is the speed of sound of the neutral material, ρ_{peak} its maximum density, and Δz is the width of the neutral layer.

From the solution given by equation (4.67), the density peak is

$$\frac{\rho_{peak}}{\rho_c} = \left(\frac{2T_i}{T_n}\right)\left(\varrho_{S,i} + \varepsilon'^2\right), \tag{4.74}$$

where $\varrho_{S,i}$ is the density in units of ρ_c of the corresponding ionised region at the Strömgren height, T_i and T_n are the temperatures of the ionised and neutral media (respectively) and the ε' parameter is given by equation (4.61).

To define the width of the neutral layer, we consider it to begin at the Strömgren height and to end where the density of the neutral layer takes the value $\varrho_{S,i}$. With these considerations, from equation (4.67) we obtain

$$\begin{aligned}\frac{\Delta z}{z_0} =& \frac{2}{\sqrt{\varrho_{S,i} + \varepsilon'^2}}\left(\frac{T_n}{2T_i}\right) \\ & \times \left(\beta + \tanh^{-1}\left\{\sqrt{1 - \left(\frac{T_n}{2T_i}\right)\frac{\varrho_{S,i}}{\varrho_{S,i} + \varepsilon'^2}}\right\}\right),\end{aligned} \tag{4.75}$$

where z_0 is the characteristic height given by equation (4.42) and β is given by equation (4.66). Finally, combining equations (4.73), (4.74) and (4.75), we write the condition (4.73) as

$$Q = 2\pi\left[\beta + \tanh^{-1}\left\{\sqrt{1 - \left(\frac{T_n}{2T_i}\right)\frac{\varrho_{S,i}}{\varrho_{S,i} + \epsilon'^2}}\right\}\right]^{-1} < 1. \tag{4.76}$$

One could obtain a better stability criterion, e. g. by performing a linear analysis on the density profile given by equation (4.67). However, for a first estimation of the stability of our solutions, the criterion derived in (4.76) appears to be reasonable.

Solutions giving $Q < 1$ (which are the unstable ones), are labelled with a "(−)" in Figure 4.2. Analogously, we indicate the stable solutions (with $Q > 1$) with a "(+)".

Almost all of the solutions corresponding to configurations where the planar approximation is valid (as we pointed out in section 4, the solutions associated to ε =22.7, 56.8 and 227.4 in Figure 4.2, are not valid in the planar approximation) are gravitationally stable.

The "most stable" neutral layers, are those in the triad of curves associated to the

$\lambda = 0.1$, $\delta = 0.1$ configuration, having $Q \approx 2.8$. The triad of solutions corresponding to the $\lambda = 0.25$, $\delta = 1$ configuration have $Q \sim 1$, with the only one unstable solution being the $\varepsilon_i = k_0\varepsilon$ curve with $Q = 0.9$. This unstable solution represents a plane of stars of $\Sigma_* \sim 60$ $\mathrm{M_\odot pc^{-2}}$ surrounded by an ionised region with a central number density of $n_c \sim 40$ $\mathrm{cm^{-3}}$, having very low dust abundance, covered by a neutral layer with dust cross section $\sigma_d \sim 10^{-21}$ $\mathrm{cm^2\ H^{-1}}$. We conclude that any configuration close to these parameters might lead to the formation of new stars as a result of the gravitational collapse of the neutral layer.

Finally, the solutions corresponding to the configurations $\lambda = 0.25$, $\delta = 0.1$ and $\lambda = 0.1$, $\delta = 1$ give $Q \approx 2.3$, and are therefore gravitationally stable.

4.5 Summary and discussion

In this chapter we studied the effect of the radiation pressure on the hydrostatic structure of gas surrounding a planar distribution of stars. We present solutions of the plane-parallel hydrostatic balance between the gas pressure gradient, the radiation pressure (associated with the photoionization and dust absorption processes) and the gravitational force provided by the stellar slab and the gas.

We found that the solutions depend on a set of four dimensionless parameters and we obtained three different gas distributions:

- solutions in which the photoionized region extends to infinite heights,
- solutions with a photoionized region which is bounded by a narrow, high density neutral cap,
- solutions with a stratified neutral structure (with a small or non-existent photoionized region).

The first of these types of solutions occurs when massive stars are embedded into a low-density gaseous medium. The second one is found the in cases when the stars are surrounded by a denser ISM. The third solution (with no photoionization) could be used in the case when only low mass stars are formed. Our models are useful for evaluating which of these gas configurations one has to adopt in the case of disk-like star-forming galaxies with different characteristics.

We consider our models to be valid for stellar surface densities lower than $\Sigma_* \sim 100$ M$\odot$ pc^{-2}. Stellar distributions with higher surface densities are likely to be found in the central zones of spiral galaxies, where the planar approximation is not valid.

The combined effects of radiation pressure on dust grains together with self-gravity, make the neutral covering layers of some configurations unstable to gravitational collapse. However, most of the solutions for which the planar approximation is valid are stable, and therefore the hydrostatic structures obtained from our models are likely to persist in time.

Flattened starbursts and the feedback they inject on its surrounding medium have applications, e.g., in the study of proto-galaxies and in the interpretation of the star formation history of spiral galaxies.

The main assumption of the models obtained in this chapter was the consideration of an infinitely extended distribution of massive stars, which is an idealised configuration. Although it is true that starbursts at galactic scales are plane, they are not likely to adopt a uniform and very extended configuration that resembles an infinite starburst plane.

To move towards more realistic configurations, 2D axi-symmetric models with finite extension could be appropriate. This improvement clearly introduce new features in the models, for instance, the gravitational potential due the gas and the mid-plane stars would be z and r-dependent (in cylindrical coordinates), as well as the direction and strength of the radiation pressure.

Another strong limitation of the models presented in this chapter is that we considered the flux of photons to be constant with z, i.e., we neglected the attenuation of the radiation due to absorption. This approximation is correct in the photoionised region where the column density is small in comparison with the stellar surface density Σ_*. Also, at the ionisation front, the flux of photons does not have a considerable attenuation, since for stellar populations including O-B stars, the ratio of non-ionising to ionising photons is ~ 5 (Draine 2011).

However, the optical depth in the neutral zone is far from being negligible. For this reason, we obtained very high peaks in the neutral gas density, for some parameter configurations. Incorporating the optical depth, the heights of the density peaks within the neutral regions will be reduced. Clearly our model equations could

be extended to include the dust optical depth, but this will not change the general properties of our solutions.

Chapter 5

Supernova Blast Wave in a Star Cluster Outflow

In this chapter we present a model of a SN blast wave that goes off in the centre of a "cluster wind" flow generated by the interacting winds from the cluster stars. We consider the exact analytic solution of Cantó et al. (2000) for the wind flow (which is obtained assuming a spherical cluster of uniformly distributed stellar wind sources). We derive a semi-analytic model for the evolution of the SN blast wave and compare it with spherical symmetric, gas dynamic simulations.

In the next section we give some general considerations of the conditions for which we derive our model. The semi-analytical model is developed in Section 5.2, and the numerical simulations are described in Section 5.3 The prediction of the free-free emission luminosity is presented in Section 5.4, Finally, our results are summarised in Section 5.5

Most of the content of this chapter can be found in the paper by Rodríguez-Ramírez et al. (2014).

5.1 General considerations

We model the expansion of a blast wave in the Taylor-Sedov (T-S) phase. This phase begins after a free expansion of the material ejected by the SN, when the mass of the environmental material, which is swept up by the blast wave, is of the order of the mass ejected by the supernova. Therefore, if the SN goes off in the centre of a

cluster wind flow, then the initial radius of the bubble R_0 of the Taylor-Sedov phase satisfies the condition

$$M_{sn} \simeq 4\pi \int_0^{R_0} R'^2 \rho_e(R') dR', \tag{5.1}$$

where M_{sn} is the mass ejected by the supernova and $\rho_e(R)$ is the density of a spherically symmetric pre-existent environment. Cantó et al. (2000) showed that for a cluster with a homogeneous distributions of stellar wind sources this density is given by

$$\frac{\rho_e}{\rho_c} = \begin{cases} A_\gamma r/u_e & \text{for } r < 1, \\ A_\gamma/\left(r^2 u_e\right) & \text{for } r > 1\,, \end{cases} \tag{5.2}$$

where

$$\rho_c = \frac{N\dot{M}_w}{4\pi v_w R_c^2 A_\gamma} \tag{5.3}$$

is the central density of the cluster wind flow, $r \equiv R/R_c$ is the radius in units of the cluster radius R_c, $u_e \equiv v_e/v_w$ the cluster wind velocity in units of the terminal velocity v_w of each star of the cluster, $\dot{M}_w$ is the mass loss rate of each star of the cluster, N is the number of the stars inside the cluster radius and A_γ is an integration constant. which depends of the specific heat ratio $\gamma = c_P/c_V$. The dimensionless velocity u_e is found as an exact solution in implicit form in the model of Cantó et al. (2000), however we give an analytic approximation of u_e as a function of the dimensionless radius r in the Appendix B.

From equations (5.1)-(5.3), we find that the T-S radius R_0 must satisfy the equation

$$I(R_0/R_c) = \frac{M_{sn} v_w A_\gamma}{N\dot{M}_w R_c} \tag{5.4}$$

where

$$I(r) \equiv \int_0^r r'^2 \varrho(r')\, dr', \tag{5.5}$$

is an analytic function, built with analytic fits to the implicit exact solution for the density of the cluster wind of Cantó et al. (2000) (see appendix B). If we introduce an ejected mass of 5 $M_\odot$ (which is a typical value for a type II SN, expected in young stellar populations, see Pérez-Rendón et al. 2009) inside a cluster of 5×10^3 O stars within a radius $R_c = 0.5$ pc, with mass loss rate and wind velocities

$\dot{M}_w = 10^{-6}\mathrm{M}_\odot\mathrm{yr}^{-1}$ and $v_w = 1000$ kms^{-1}, from equation (5.4) we obtain

$$r_0 \equiv \frac{R_0}{R_c} = 1.56. \tag{5.6}$$

Alternatively, if we choose a cluster radius $R_c = 5$ pc, we obtain

$$r_0 = 0.49. \tag{5.7}$$

From equations (5.6)-(5.7) we see that the T-S phase of the SN remnant could begin inside or outside the cluster radius. We then apply a T-S phase model of the SN blast wave after the radius R_0 has been reached. Either in the $R_0 < R_c$ or in the $R_0 > R_c$ case, the time t_0 after the SN explosion at which the T-S radius R_0 is reached can be estimated as

$$t_0 = \frac{R_0}{v_{sn}}, \tag{5.8}$$

where v_{sn} is the initial velocity of the ejected material. Therefore, for estimating t_0 in equation (5.8) we assume that the ejected material preserves its initial velocity until the T-S radius is reached. We consider that this initial velocity (of an expanding, uniform density sphere) depends on the energy E and the ejected mass M_{sn} as:

$$v_{sn} = \left(\frac{10\alpha E}{3M_{sn}}\right)^{1/2}. \tag{5.9}$$

In equation (5.9) the α parameter is the initial fraction of the SN energy in the form of kinetic energy, and we consider a linear initial radial velocity profile for the ejected material, as described in detail in Section 5.3. This energy fraction changes as the interaction of the blast wave with the environment proceeds, but the parameter α corresponds to its initial value (see equation 5.8).

5.2 A semi-analytic model for the supernova blast wave

5.2.1 The kinematics of the hot bubble and the shock

Let us consider the expansion of the hot bubble. The outer radius of the bubble is a contact discontinuity that pushes a spherical shock into the surrounding environment. This environment is the cluster wind, and it therefore flows outwards (at a velocity v_e).

Let us call (ρ_1, v_1, p_1) and (ρ_2, v_2, p_2) the pre-shock and post-shock variables (respectively) in the rest frame of the outer shock. In this frame, the pre-shock velocity v_1 is

$$v_1 = \frac{dS}{dt} - v_e \,, \tag{5.10}$$

where dS/dt is the shock velocity and v_e is the velocity of the external environment, both measured in the cluster rest frame. In this cluster reference frame, the shock velocity follows the relation of a shock driven by a piston (the piston being the contact discontinuity at the outer radius R of the bubble):

$$\frac{dS}{dt} = \frac{dR}{dt} + v_2, \,, \tag{5.11}$$

where v_2 is the post-shock velocity in the rest frame of the shock. Combining equations (5.10) and (5.11) we obtain the velocity of the outer radius of the bubble in terms of the pre-shock, post-shock and environment velocity:

$$\frac{dR}{dt} = v_1 - v_2 + v_e \,. \tag{5.12}$$

We now consider the shock jump relations

$$v_2 = \frac{\gamma - 1}{\gamma + 1} v_1 + \frac{2}{\gamma + 1} \frac{c^2}{v_1} \,, \tag{5.13}$$

$$p_2 = \frac{2}{\gamma + 1} \rho_1 v_1^2 - \frac{\gamma - 1}{\gamma + 1} p_1 \,, \tag{5.14}$$

and combining them with equation (5.12), we obtain:

$$\frac{\mathrm{d}R}{\mathrm{d}t} = \frac{2}{\gamma+1}\left(v_1 - \frac{c^2}{v_1}\right) + v_e\,, \tag{5.15}$$

with

$$v_1 = \left(\frac{\gamma+1}{2\rho_e}P_b + \frac{\gamma-1}{2\gamma}c^2\right)^{1/2}\,, \tag{5.16}$$

and

$$c^2 = \frac{\gamma-1}{2}\left(v_w^2 - v_e^2\right)\,, \tag{5.17}$$

where we have introduced the adiabatic preshock sound speed $c^2 = \gamma p_1/\rho_e$, we have used the fact that the pre-shock density ρ_1 is the environmental density ρ_e, and that the post-shock pressure p_2 equals the bubble pressure (across the contact discontinuity), which we call P_b. Equation (5.17) is the environmental sound speed in terms of the cluster wind velocity v_e and the velocity of the stellar winds v_w, as obtained by Cantó et al (2000). In deriving equation (5.15) for the bubble radius, we have considered the general jump relations 5.13-5.14), allowing the appropriate strong/weak transition for the external shock driven by the SN bubble.

In the next subsection we find an expression for the pressure of the hot bubble as a function of its external radius R, which is useful for integrating the equations of motion for the external radius of the hot bubble and for the radius of the outer shock.

5.2.2 The energy of the bubble

We now consider that the pressure P_b inside the supernova bubble is uniform. We also assume that the evolution of the bubble is much faster than the timescales of the energy and mass injection due to the winds of the stellar cluster, after the supernova explosion (we justify this assumption in the next subsection). We can therefore assume that the energy E of the supernova explosion is equal to the thermal energy of the hot bubble plus the kinetic energy of an outer, thin shell containing the swept-up environment:

$$E = \frac{P_b V}{\gamma-1} + \frac{1}{2}M_s v_s^2, \tag{5.18}$$

with P_b the uniform pressure of the bubble, $V = 4\pi R^3/3$ the bubble volume, v_s the velocity of the shell and

$$M_s = 4\pi \int_0^R R'^2 \rho_e(R') \mathrm{d}R' \,, \tag{5.19}$$

the mass of the swept-up environment within the shell.

We now consider the thin shell of swept-up material, with a velocity $v_s \simeq dR/dt$. In addition, we consider the strong shock limit in equations (5.12) and (5.14), and assume that the pressure of the shell is equal to the pressure P_b of the hot bubble. We then obtain:

$$v_s^2 = \left(\frac{dR}{dt}\right)^2 = \frac{2}{\gamma+1}\frac{P_b}{\rho_e} \,. \tag{5.20}$$

Finally, from equations (5.18)-(5.20) we obtain that the pressure of the bubble P_b as a function of its external radius R is:

$$P_b(R) = \frac{E}{4\pi}\left(\frac{R^3}{3(\gamma-1)} + \frac{\int_0^R R'^2 \rho_e(R') \mathrm{d}R'}{(\gamma+1)\rho_e(R)}\right)^{-1} \,, \tag{5.21}$$

where the integral that appears in the right hand side has an analytical solution if we use the analytical fit (given in equations (B.5) and (B.6) of Appendix B) to the implicit density stratification of the cluster wind solution of Cantó et al. (2000).

We note that in the case of a constant environmental density (which is a good approximation for the density inside of the cluster) equation (5.21) reduces to the pressure-energy relation given in Raga et al. (2012c) for a SN bubble that expands into an uniform density medium. In deriving equation (5.21) we have considered the strong shock limit for the jump relations (5.14-5.13). This assumption of a strong shock (for calculating the fraction of the SN energy that goes into thermal energy of the hot bubble) is inconsistent with the fact that we have allowed a general (strong/weak) shock in the equation of motion for the outer, thin shell (see equation 5.12). This inconsistency is at the heart of the "thick shell " formalism developed in Raga et al. (2012 a,c,d, for the expansion of compact HII regions, wind-driven HII regions, and supernova blast waves in uniform environments), which we have followed here to derive our semi-analytical model. However, since the resulting models only show a weak dependence on the fraction of energy division (between

thermal energy of the hot bubble and kinetic energy of the shell) this inconsistency is unlikely to introduce appreciable effects on the model results.

In the next subsection we use the relation between the pressure and the radius (equation 5.21) to obtain an equation of motion for the expansion of the bubble.

5.2.3 Motion equations for the bubble radius and the shock

For obtaining an equation of motion for the outer radius of the hot bubble we combine equations (5.15)-(5.17) with (5.21). We also combine equations (5.10), (5.16) and (5.21) for obtaining an equation of motion for the shock pushed out by the hot bubble. In dimensionless form, the motion equations for the shock and the bubble radius are:

$$\frac{dr}{d\tau} = \frac{2}{\gamma+1}\left(u_1 - \frac{(\gamma-1)}{2}\frac{1-u_e^2}{u_1}\right) + u_e \tag{5.22}$$

$$\frac{ds}{d\tau} = u_1 + u_e, \tag{5.23}$$

with

$$u_1 = \left(\frac{(\gamma+1)}{2}A_\gamma \sigma \frac{p_b}{\varrho_e} + \frac{(\gamma-1)^2}{4\gamma}(1-u_e^2)\right)^{1/2}, \tag{5.24}$$

where $r \equiv R/R_c$ is the dimensionless radius of the hot bubble, $s \equiv S/R_c$ is the dimensionless radius of the outer shock, $\tau \equiv v_w t/R_c$, is the dimensionless time, $u_1 \equiv v_1/v_w$ the dimensionless preshock velocity, $u_e \equiv v_e/v_w$ and $\varrho_e \equiv \rho_e/\rho_c$ are the dimensionless velocity and density of the preexistent environment. In Appendix B, we have approximated u_e and ϱ_e by analytic explicit functions of r as fits to the exact implicit solutions of Cantó (2000).

The pressure of the bubble in units of $E/(4\pi R_c^3)$ is:

$$p_b(r) = \left[\frac{r^3}{3(\gamma-1)} + \frac{1}{(\gamma+1)\varrho_e(r)}\int_0^r r'^2 \varrho_e(r')dr'\right]^{-1}, \tag{5.25}$$

and finally, σ is the free dimensionless parameter

$$\sigma \equiv \frac{E}{N R_c \dot{M}_w v_w}\,. \tag{5.26}$$

As we have mentioned in the last subsection, our model equation is valid provided the energy E of the supernova is much larger than the energy input $E_w = \frac{1}{2}N\dot{M}_w v_w^2 t$ due to the stellar winds. This implies the condition

$$\tau << 2\sigma \tag{5.27}$$

for the dimensionless time. If we introduce the values of the physical parameters which give the initial radius of the T-S phase $r_0 = 1.56$ (see equation 5.4) for calculating the parameter σ we obtain

$$\sigma = 41.11 \left(\frac{E}{2\times 10^{51}\text{ergs}}\right)\left(\frac{5\times 10^3}{N}\right)\left(\frac{0.5\text{pc}}{R_c}\right)$$
$$\times \left(\frac{1\times 10^{-6}\text{M}_\odot\text{yr}^{-1}}{\dot{M}_w}\right)\left(\frac{1000\text{kms}^{-1}}{v_w}\right), \tag{5.28}$$

where we have chosen a SN energy $E = 2\times 10^{51}$erg, a typical value in core-collapse supernova, see Woosley&Janka(2005). Alternatively, if we choose a radius of $R_c = 5$ pc which gives the initial T-S radius $r_0 = 0.49$ (from equation 5.4) we obtain

$$\sigma = 4.11 \left(\frac{E}{2\times 10^{51}\text{ergs}}\right)\left(\frac{5\times 10^3}{N}\right)\left(\frac{5\text{pc}}{R_c}\right)$$
$$\times \left(\frac{1\times 10^{-6}\text{M}_\odot\text{yr}^{-1}}{\dot{M}_w}\right)\left(\frac{1000\text{kms}^{-1}}{v_w}\right). \tag{5.29}$$

Given a fixed value of σ we integrate numerically equations (5.22)-(5.23) together with its corresponding initial radius r_0, i.e. one integration for $r_0 = 0.49$, $\sigma = 4.11$ and another for $r_0 = 1.56$, $\sigma = 41.11$.

Given the initial S-T radius r_0, we obtain the corresponding initial time in units of R_c/v_w from equation (5.9) as

$$\tau_0 = \frac{r_0}{u_{sn}}, \tag{5.30}$$

with

$$u_{sn} = \frac{v_{sn}}{v_w} = \left(\frac{10\alpha A_\gamma \sigma}{3I(r_0)}\right)^{1/2}, \tag{5.31}$$

where v_{sn} is the velocity of the ejecta given in equation (5.9) and we have substituted the ejected mass M_{sn} from equation (5.4). In this way we write the ejected mass in terms of the T-S radius r_0 using equation (5.1). The numerical solutions for the

outer radius of the SN bubble and for the external SN shock as functions of the time τ are shown in Figure 5.1 together with the numerical simulations of the gasdynamic equations (with the corresponding σ and r_0 values), which are described in the next section.

5.3 Numerical simulations

We can describe the evolution of the supernova explosion without the restriction given by equation (5.27) by integrating numerically the 1D, spherically symmetric, time-dependent Euler equations with a mass and energy source terms $n\dot{M}_w$ and $\frac{1}{2}n\dot{M}_w v_w^2$ (respectively). These source terms represent the mass and energy per unit volume and time injected by the stellar winds (with a number density of n stars per unit volume) within the cluster (i.e., for $R \leq R_c$). In dimensionless form, the Euler equations take the form:

$$\partial_\tau \rho' + \partial_r(\rho' v') = 3A\delta - \frac{2\rho' v'}{r}, \tag{5.32}$$

$$\partial_\tau(\rho' v') + \partial_r\left(\rho' v'^2 + p'\right) = -\frac{2\rho' v'^2}{r}, \tag{5.33}$$

$$\partial_\tau E' + \partial_r\left(v'(E' + p')\right) = \frac{3A}{2}\delta - \frac{2v'(E' + p')}{r}, \tag{5.34}$$

where $E' = \rho' v'^2/2 + 3p'/2$ and the dimensionless density, velocity and pressure are defined in terms of the corresponding dimensional variables through:

$$\rho' \equiv \rho/\rho_c, \quad v' \equiv v/v_w, \quad p' \equiv p/(\rho_c v_w^2)\,. \tag{5.35}$$

The dimensionless radius r and time τ are defined in terms of the dimensional variables R and t as:

$$r \equiv R/R_c\,; \quad \tau \equiv t v_w/R_c\,. \tag{5.36}$$

The δ coefficient is defined as

$$\delta = \begin{cases} 1 & \text{for } r < 1 \\ 0 & \text{for } r > 1\,. \end{cases} \tag{5.37}$$

We set the initial conditions of our simulations as follows. Inside a small inner region $R < R_{sn}$ (where $R_{sn} \ll R_c$), we introduce a hot bubble of gas of constant density

$$\rho = \frac{3M_{sn}}{4\pi R_{sn}^3}, \tag{5.38}$$

where M_{sn} is the mass ejected by the supernova explosion. In this small region we also set a linear velocity profile (as has been done by Jun & Norman 1996 and Velázquez et al. 2006):

$$v = \frac{R}{R_{sn}} v_{sn}, \tag{5.39}$$

where v_{sn} is the velocity of the material at a radius R_{sn} (this is the maximum velocity of the profile). We calculate the velocity v_{sn} of the ejected material and its pressure p (which we consider uniform) by assuming that the supernova energy E is divided initially into a fraction of kinetic energy $E_K = \alpha E$ and thermal energy $E_{th} = (1-\alpha)E$ and using the energy conservation equation

$$E = 4\pi \int_0^{R_{sn}} R^2 \left(\frac{1}{2}\rho v^2 + \frac{p}{\gamma - 1} \right) \mathrm{d}r = E_K + E_{th}. \tag{5.40}$$

Then, from equations (5.38)- (5.40) we obtain the initial density, velocity and pressure, in dimensionless form (see equation 5.35) as

$$\rho' = \frac{3I(r_0)}{r_{sn}^3}, \tag{5.41}$$

$$p' = \frac{3(1-\alpha)(\gamma-1)A_\gamma \sigma}{r_{sn}^3}, \tag{5.42}$$

$$v' = \left(\frac{10\alpha A_\gamma \sigma}{3I(r_0)} \right)^{1/2} \frac{r}{r_{sn}}, \tag{5.43}$$

and we have set the ejected mass M_{sn} in terms of the mass of the pre-existent environment of the stellar cluster inside a radius R_0 (the T-S radius) by using equation (5.4). It should be noted that the value of the fraction of kinetic energy of the blast wave will change as the blast wave evolution proceeds, but in equations (5.41)-(5.43) we consider the parameter α as the initial fraction. Finally, σ is the dimensionless parameter of the analytical model described in the previous section.

For doing numerical integrations of the dimensionless equations (5.32)-(5.34) with the initial conditions given in (5.41)-(5.43), we considered the values of the parameters σ and r_0 corresponding to the integration of the semi-analytic model. Therefore we performed a numerical simulation by setting $\sigma = 41.11$ and $r_0 = 1.56$ (obtained with the physical parameters of equations 5.6 and 5.28) in the initial conditions. In this numerical simulation we set the initial radius of the ejecta $r_{sn} = 0.2$. Alternatively, we performed numerical simulations corresponding to the parameters $\sigma = 4.11$ and 0.49 of the semi-analytic model (obtained with the physical parameter of equations 5.7 and 5.29). In this numerical simulation we set the initial radius of the ejecta $r_{sn} = 0.1$. In both simulations we consider a fraction $\alpha = 0.7$ for the kinetic energy of the explosion. We integrate numerically equations (5.32)-(5.34) by using the "flux vector splitting" algorithm of Van Leer (1982) with second order in space, in a 1-D mesh of 4000 cells. We describe in Appendix A the this numerical algorithm.

In Figure 5.1 we show the density of the flow given by the numerical simulations compared with the corresponding solutions of equations (5.22)-(5.23) of the semi-analytic model for the temporal evolution of the bubble and the external shock.

5.4 Luminosity

In this section we calculate the X-ray luminosity of the SN remnant as a function of time. To do this, we approximate the X-ray emission as the free-free emission coefficient j_ν integrated over all frequencies and over a volume limited by an outer radius R_{max}, which could be the radius of the external shock S (if we use the semi-analytic model) or the size of of the computational grid (if we use the gas dynamic simulations). Then we have

$$L = 4\pi \int_0^{R_{max}} \int_0^{\infty} R'^2 4\pi j_\nu \, d\nu dR', \tag{5.44}$$

where

$$j_\nu = K \frac{\rho^2}{T^{1/2}} \exp\left(-\frac{h\nu}{kT}\right), \tag{5.45}$$

with

$$K = \frac{32 Z^2 e^4 h}{3 m_e^2 m_H^2 c^3 4\pi} \left(\frac{\pi \chi_{z-1}}{3k}\right)^{1/2}, \tag{5.46}$$

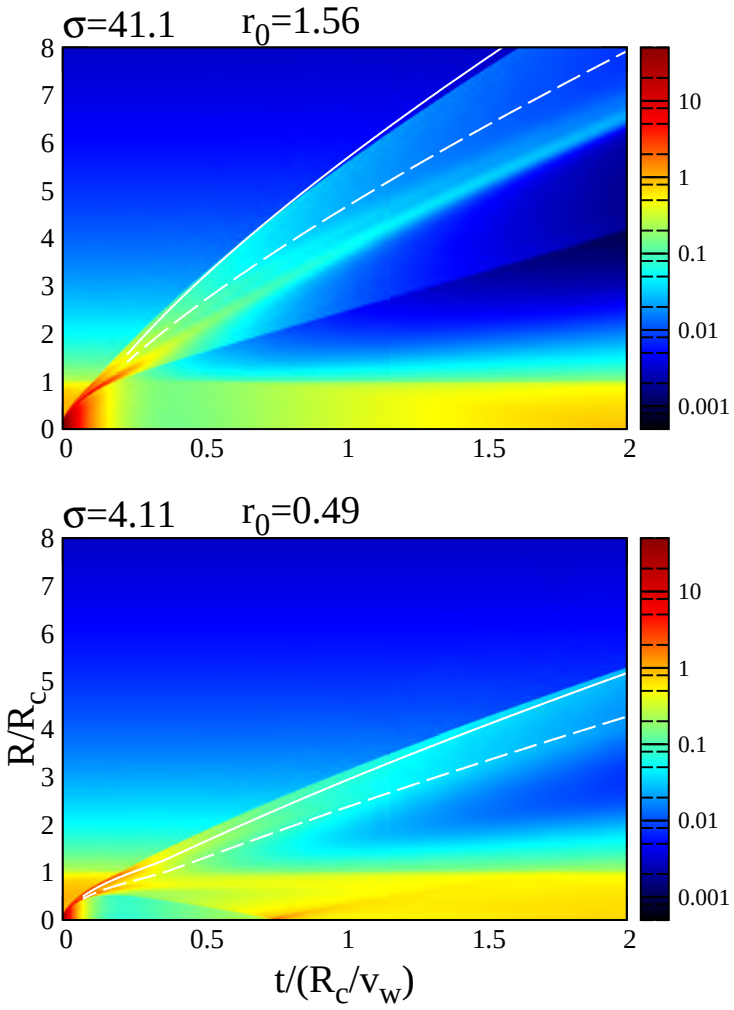

Figure 5.1: Evolution of the bubble and the driven shock by a SN which goes off in the centre of a stellar cluster wind. We show the model corresponding to a T-S radius $r_0 = 0.49$ and $\sigma = 4.11$ (bottom), obtained by inserting the typical physical parameters of equations (5.29) and (5.7). Alternatively in the top graph we show the model corresponding to $r_0 = 1.56$ and $\sigma = 41.11$ for the physical parameters of equations (5.6) and (5.28). The white curves are the radius (in units of R_c) of the bubble (dashed line), and the driven shock (solid line) as a function of the time (in units of the characteristic time R_c/v_w). These curves are numerical solutions of equations (5.22) and (5.23) of the semi-analytic model derived in Section 5.2. The colour stratification represents the density of the flow as a function of radius and time, obtained from the numerical simulations of the spherical gas dynamic equations (5.32)-(5.34). The simulations were performed with the values of the characteristic parameters r_0 and σ (see the initial conditions in equations 5.41-5.43) corresponding to the curves of the semi-analytic model. Both simulations have been performed with the value $\alpha = 0.7$, which is the contribution of the kinetic energy to the total energy of the explosion in the initial conditions, as we explain in Section 5.3.

is the free-free emission coefficient taken from the book of Osterbrock & Ferland Sausalito (2006). We consider an ideal equation of state in order to write the temperature in terms of the density and pressure of the ionised gas:

$$T = \frac{m_H}{2k}\frac{P}{\rho}, \tag{5.47}$$

and then, from equations (5.44-5.47) we obtain

$$L = \frac{4\pi k K}{h}\left(\frac{m_H}{2k_B}\right)^{1/2}\int_0^{R_{max}} R'^2\rho^{3/2}P^{1/2}dR'. \tag{5.48}$$

We can integrate equation (5.48) using the solutions of the semi-analytical model or from the numerical simulations of the full gasdynamic equations (5.32)-(5.34).

When applying the semi-analytical model we divide the emission into a "hot bubble" and a "shell" component:

$$\int_0^S R'^2\rho^{3/2}P^{1/2}dR' =$$

$$\int_0^R R'^2\rho_b^{3/2}P^{1/2}dR' + \int_R^S R'^2\rho_{sh}^{3/2}P^{1/2}dR', \tag{5.49}$$

where

$$\rho_b = \frac{3M_{sn}}{4\pi R^3}, \tag{5.50}$$

is the density of the SN bubble (which we consider to be uniform). We calculate the density of the shell of swept up material as

$$\rho_{sh} = \frac{3}{S^3 - R^3}\int_0^S R'^2\rho_e(R')dR', \tag{5.51}$$

and we also consider it as uniform. In both terms of the RHS of equation (5.49) we use equation (5.21) for setting an uniform pressure as a function of the external radius of the bubble, obtaining:

$$L = K_1\sigma^{1/2}L_0 p_b^{1/2}(r)\left[\left(\frac{I(r_0)}{r}\right)^{3/2} + \frac{I(s)^{3/2}}{(s^3 - r^3)^{1/2}}\right], \tag{5.52}$$

with

$$K_1 = \left(\frac{3m_H k}{2A_\gamma^3}\right)^{1/2} \frac{K}{4\pi h}, \tag{5.53}$$

and

$$L_0 \equiv \frac{\left(N\dot{M}_w\right)^2}{v_w R_c}, \tag{5.54}$$

for the luminosity of the SN remnant at a given time.

If we use the numerical simulations for calculating the luminosity (equation 5.48), we take the solutions for the density and pressure, and we add the contributions of all the computational cells:

$$L = K_2 L_0 \left(\Delta r\right)^3 \sum_i i^2 \rho_i'^{3/2} p_i'^{1/2}, \tag{5.55}$$

with

$$K_2 = \left(\frac{m_H k}{2A_\gamma^4}\right)^{1/2} \frac{K}{4\pi h} \tag{5.56}$$

for each time-step of the simulation.

Let us note that if we vary the values of the number of stars N and the cluster radius R_c in such a way that we keep the product NR_c constant, we obtain the same value for the parameters σ and r_0 (as can be seen from equations 5.4 and 5.26), but we obtain different luminosities as can be seen from equation (5.54).

In Figure 5.2, we plot the luminosities given by equations (5.52)-(5.55) and we have chosen the model of $\sigma = 41.11$ and $r_0 = 1.56$ given by the values of the physical parameters $E = 2 \times 10^{51}$ erg, $M_{sn} = 5$ M$_\odot$, $v_w = 1000$ km s^{-1}, $\dot{M}_w = 1 \times 10^{-6}$ M$_\odot$ yr^{-1}, $N = 5 \times 10^3$ and R_c =0.5 pc. Alternatively, if we choose the values $N = 10^3$ and $R_c = 2.5$ pc, we obtain a model of a luminosity diminished by a factor of 125 (as can be seen from equation 5.54), but this change gives the same values $\sigma = 41.11$ and $r_0 = 1.56$.

5.5 Summary and discussion

We have developed a semi-analytical model for a supernova blast wave which goes off in the centre of a stellar cluster outflow. We have then compared this model with numerical simulations with the full, spherically symmetric Euler equations (with

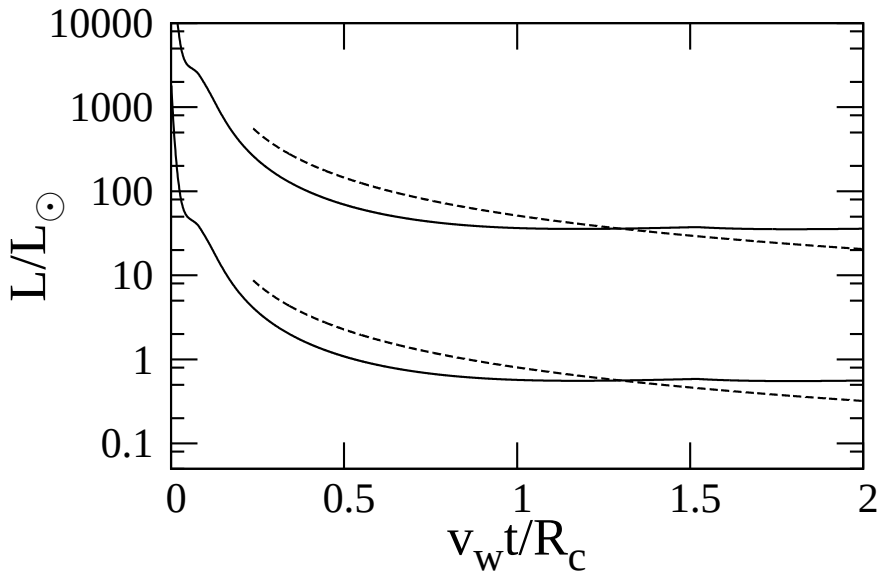

Figure 5.2: Comparison between the semi-analytic approach (dashed lines, see equation 5.52) and the computation obtained from the gasdynamic simulation (solid lines, see equation 5.55), for the X-ray luminosity (in units of the solar luminosity), as a function of time (in units of R_c/v_w) of the resulting flow due to the SN explosion within a cluster wind. The upper curves were calculated for a SN of $E = 2 \times 10^{51}$ erg, $M_{sn} = 5$ M$_\odot$ in a cluster wind of $\dot{M}_w = 10^{-6}$M$_\odot$yr^{-1}, $v_w = 1000$ kms^{-1} (of the individual stars), $N = 5 \times 10^3$ stars inside a radius of $R_c = 0.5$ pc which gives $\sigma = 41.11$ and $r_0 = 1.56$ (see equations 5.28 and 5.6). The lower curves are calculated with the same physical parameters but with $N = 1 \times 10^3$ and $R_c = 2.5$ pc, which gives the same value of σ and r_0.

appropriate mass and energy source terms).

From the semi-analytical approach we have derived dimensionless equations of motion for the external radius of the SN bubble (equation 5.22) and for the radius of the outer shock (equation 5.23). For deriving these equations we assumed that the blast wave is in the T-S phase, with an approximately uniform pressure inside the SN bubble. This phase has an initial radius R_0, which we have estimated as the point at which the mass M_{sn} of the SN ejecta is equal to the swept-up mass of the pre-existent cluster wind (see equations 5.1-5.4) given by the model of Cantó et al. (2000).

We found that for a massive cluster of ~ 1000 O stars each one with the typical values $\dot{M}_w = 1 \times 10^{-6} \mathrm{M}_\odot$ yr^{-1} and $v_w = 1000$ kms^{-1} inside a cluster of radius $R_c \sim 0.5$ pc, the T-S radius R_0 of a SN remnant with a typical ejected mass $M_{sn} \sim 5$ $\mathrm{M}_\odot$ is in the $R_0 > R_c$ regime (see equation 5.6). Alternatively, we found that the SN remnant is in the $R_0 < R_c$ regime for the same physical parameters but with a cluster of radius $R_c \sim 5$ pc. (see equation 5.7).

However it is often found that the mass of a core collapse SN ejecta can be several times greater than 5 $\mathrm{M}_\odot$. At the same time, the terminal wind velocities of O stars can be of $v_w = 4000$ km s^{-1}. Therefore from equation (5.4) we see that for massive clusters of O stars, it would be more likely to find SN blast waves in the $R_0 > R_c$ regime.

The model equations of our semi-analytic approach, which are characterised by the dimensionless parameter σ, have been derived with the general form of the Rankine-Hugoniot conditions and by following the formulation of Raga et al. (2012 a,c,d, see Section 5.2), which gives equations of motion which allow the appropriate strong/weak transition of the driven external shock. However we can see from equations (5.22) and (5.23) that in the $R > R_c$ region, the SN bubble always drives a strong shock, since in this region $u_e = v_e/v_w \to 1$ rapidly (see Figure 5.1) and then equations (5.22)-(5.23) remain in the strong shock limit.

We have solved numerically these equations for two different values of the parameter σ, one corresponding to the $R_0 < R_c$ regime, and the other to the $R_c > R_0$ case (see equations 5.28-5.29), and compared these solutions with the gas dynamic simulations (equations 5.32-5.34), which are also characterised by the corresponding value of the parameter σ in the initial conditions (see equations 5.41-5.43). These

solutions are shown in Figure 5.1, where we can see that the semi-analytical and fully numerical approaches give very similar positions for the outer shock as a function of time. However, the semi-analytical solution of the $R_0 > R_c$ regime overestimates the position of the SN bubble radius in comparison with the corresponding numerical simulation. This is due to the fact that in this $R_0 > R_c$ regime, the T-S phase is reached in a $\sim R^{-2}$ stratified environment and then the reverse shock of the ejected material always expands behind the bubble radius (as can be seen in the top graph of Figure 5.1). Therefore the SN bubble is far from having an uniform pressure even at early times, which is not consistent with the assumptions of the semi-analytic model (see section 5.2). This is not the case in the $R_0 < R_c$ regime (bottom graph of Figure 5.1), where the T-S phase is reached in an approximately flat density environment and then the reverse shock goes back to the origin of the explosion and the SN bubble has an approximately uniform pressure at least at early times (when the mass and energy injection from the stars of the cluster is negligible). The behaviour of the reverse shock has been described in Truelove & McKee (1999), who model the SN blast wave and reverse shock with different initial stratifications of the ejecta and the environment. However the cluster wind model which we take as the initial environment is a little more complex since it is accelerated until a terminal wind velocity and has a transition from "flat" to $\propto R^{-2}$ stratification density.

Finally, we have also calculated an estimate of the X-ray luminosity by integrating the free-free emission coefficient using the semi-analytic model (considering the emission of the bubble and the shell), and the numerical simulations. From Figure 5.2 we see that these two approaches give luminosities that decay as a function of the time. The semi-analytic model (which starts at the time in which the T-S phase begins) first overestimates and at later times underestimates the luminosity. The early overestimation of the luminosity (in the analytic model) is a result of the fact that the radius of the hot bubble is larger in the semi-analytic model (see Figure 5.2), leading to an enhanced density in the outer shell (which dominates the X-ray luminosity). At later times, the numerical simulations produce larger X-ray luminosities because the cluster wind flow begins to be regenerated. This effect is not present in the semi-analytic model, which does not include the energy and mass source terms necessary for regenerating the cluster wind.

We also show that the luminosity changes appreciably if we vary the number of

stars N, and the radius R_c of the cluster in such a way that the product NR_c remains constant (which fixes the values of the parameters σ and r_0). In Figure 5.2 we show this effect by showing two models with $r_0 = 1.56$ and $\sigma = 41.11$ (see equations 5.6 and 5.29), but with $(N = 5000, R_c = 0.5\,\mathrm{pc})$ and $(N = 1000, R_c = 2.5\,\mathrm{pc})$, respectively. We find that the luminosity differs by approximately two orders of magnitude between these two models.

As can be seen from Figure 5.2, a SN going off in the centre of a cluster wind flow increases its X-ray luminosity by ~ 3 orders of magnitude. This increased luminosity decays over a period of $\sim R_c/v_w$ (~ 500 yr for $R_c \sim 0.5$pc and $v_w \sim 1000$ km s^{-1}) to its undisturbed cluster wind value. Such increased luminosities might be seen in X-ray observations of massive stellar clusters. Therefore, the models developed in this paper could be applied in the context of the observations of Jaskot et al. (2011) of young super-shells (i.e. DEM L50, DEM L152 in the large Magallanic cloud) driven by the stellar wind and SN explosions, with soft X-ray luminosities around 10^{36} erg s^{-1}. These star clusters are immersed in their parental clouds. Our models could also be applied in super-shells without parental cloud gas but with evidence of supernova explosions, e.g. N70 (see Rodríguez-González et al. 2011), which presents total X-ray luminosities around 10^{35} erg s^{-1} as a result of the interaction between the supernova explosion and the super-shell formed by the stellar cluster.

In some objects, an appreciable amount of X-ray emission might be produced in the region of interaction between the cluster wind and the outer, swept-up shell of environmental material. The contribution from this region is likely to be important in the early stages of a cluster wind flow (when it is expanding into the dense environment out of which the cluster stars have formed), and would show a limb-brightened structure. Models in which the emission from this shell is included will be necessary for modelling objects with limb-brightened X-ray emission maps.

Chapter 6

Conclusions

This thesis studies feedback produced by massive stars, focusing on HII regions and SN remnants. In the case of HII regions we study the effect of radiation pressure in the nebular structure. In the case of SN remnants we study blast waves that expands in a pre-existing star cluster wind. The motivation for these studies are the difficulties that the standard models of wind-bubbles face to explain the properties of particular interstellar bubbles. For instance, to alleviate the over-estimations that the model of Castor et al. (1975) predicts (e.g. X-ray emission, expansion velocity), it has been suggested that the stellar winds escapes through gaps and leaky structure in the bubbles. In other cases SN events has been suggested to enhance the diffuse X-ray emission predicted by the cluster-wind models of Chevalier & Clegg (1985) and Cantó et al. (2000), and obtain a better agreement with observations (see the Introduction in Chapter 1 and reference therein).

In Chapter 3 we study spherical HII regions dominated by radiation pressure (based in previous works claiming that radiation pressure is an important source of feedback, see subsection 2.3.3 and references therein), where we include the outwardly directed forces on the gas due to the absorption of photons by (i) dust grains and (ii) photoionised processes. In this model we neglect the contribution of the stellar wind to the internal pressure of the nebula, assuming that the gas of this wind escapes through leaky structures or/and the wind is weak (as is found in B-type stars).

In our approach we discuss mathematical approximations that allow us to obtain an analytic solution for the density distribution, in terms of the total luminosity of

the central star L_*, the dust absorption cross section σ_d and the external boundary of the nebula R_s.

The general morphology of this solution is a photoionised sphere with maximum density at the boundary R_s, and a density cavity at the centre. In particular, radiation pressure creates significant central cavities and drive strong density stratifications when the parameters of the system are such that $R_s \lesssim \sigma_d L_*/(8\pi kT)$. Also, if the system is close to this configuration, the size reduction effect of dusty HII regions (found in previous models with dust absorption but not including radiation pressure) now disappears. We compare our solution with numerical integrations of the model equations of Draine (2011) (who studied the same problem numerically) and find a very good agreement between both models (see Figure 3.4). With the analytic solution we reproduce the central cavities of the shell-like compact HII regions NGC 6334A and NGC 6334E, without taking into account the stellar winds (see Figure 3.10).

Our analytic model does not include the effect of gravitational forces. Thus, this model is suitable for HII regions powered by a single massive star, since the mass of HII regions powered by an ionising source equivalent to several massive stars, produce a non-negligible gravitational potential. On the other hand, the static spherical model discussed in Chapter 3 does not apply for hyper-compact HII regions. This type of nebula has a size of ~ 0.001 pc and a photoionised gas with a typical mass of $\sim 10^{-3}$ $M_\odot$ see (Kurtz & Franco 2002). In this regime the gravitational field of the central star should be included (see Keto 2003).

In Chapter 4 we extend the radiation pressure forces discussed in Chapter 3 to a plane-parallel configuration, which corresponds to an ionised gas slab powered by a planar distribution of stars. This configuration is found in the context of extended star forming episodes in galactic disks (see Haehnelt 1995), or star formation triggered by cloud-cloud collisions (see the review of Elmegreen 1998 and reference therein). The radiation pressure then provides vertical support for the ISM against the gravitational potential, for which our model considers the stellar mass and the self-gravity of the gas.

We obtain hydrostatic profiles of a planar photoionised region in pressure balance with a covering neutral layer (see figure 4.2). This structure has different extensions (of the photoionised and neutral zones) according to the chosen parameter config-

uration of the system (see equations 4.58 and 4.59). Some solutions have narrow and dense neutral layers. This motivated us to apply the Jeans stability criterion for slabs (presented in section 2.2), to evaluate the gravitational stability of the solutions, resulting most of them in stable configurations. However, we find unstable cases which correspond to a configuration of dusty ISM with superficial stellar mass $\Sigma_* \sim 60$ M$_\odot$pc^{-2} and gas density $n_c \sim 40$ cm^{-3} on the stellar plane. In this configuration we would have star formation triggered by the combined effects of self-gravity and radiation pressure.

The main limitation to the models presented in Chapters 3 and 4 is that they are hydrostatic. Photoionised regions in galaxies are generally in an expansion phase, and do not reach a hydrostatic configuration before some of the stars begin to have supernova explosions. However, it is clear that models of expanding photoionised regions rapidly reach a regime of subsonic expansion (relative to the sound speed of the ionised gas, see, e.g., Raga et al. 2012). Our present, hydrostatic solutions are appropriate for describing the internal structure of such slowly expanding regions.

Finally, in Chapter 5 we developed a semi-analytic model for a SN blast wave that expands in the centre of a pre-existing cluster wind produced by the individual winds of the massive stars in the cluster (we adopt the model of Cantó et al. 2000 for this cluster wind). Our semi-analytic model gives the radius of the bubble of ejected material as well as the outer shock of the blast wave as a function of time in dimensionless form. This solution is determined by two dimensionless parameters; r_0 characterising the radius where the T-S phase begins, and σ characterising the energy of the SN with respect to the energy of the cluster wind (see equations 5.6 and 5.26). The model for the blast wave is based on the "thick shell" formalism of Raga et al. (2012c), which allows a strong/weak transition for the outer shock. However our solutions are always found in the strong shock regime.

We compare the semi-analytic model with spherical symmetric, gas dynamic simulations and obtain a satisfactory agreement between both models (see Figure 5.1). We find that blast waves produced by type II SNe are likely to begin the T-S phase outside the cluster radius. In this case the reverse shock of the SN remnant never goes back to the centre of the explosion and always expands behind the contact discontinuity of the ejected material (see the top panel of Figure 1). This is because the T-S phase is attained where the medium has a density stratification $\propto R^{-2}$.

We calculate the total X-ray luminosity of the resulting flow, and obtain for instance that in a cluster of 2.5 pc with 1000 O stars, the blast wave increases the X-ray luminosity of the cluster wind by ~ 3 orders of magnitude (see Figure 5.2). This increased luminosity decays over a period of $\sim$ 1000 yr to its undisturbed cluster wind value, and remain enhanced by two order of magnitude during $\sim$ 100 yr. Such increased luminosities could be applied to interpret X-ray observations of massive star clusters as e.g. NGC 3603 and the Quintuplet cluster, where SN events are likely to occur.

A direct application of the work presented in this thesis is the implementation of gravity and radiation pressure terms in the hydrodynamic code used in Chapter 5, to obtain the time dependent description of expanding HII regions when gravity and radiation pressure are important. In this manner, we could obtain results beyond the limitations of the analytic models of HII regions presented in this thesis.

Appendices

Appendix A

Numerical Method for Gas Dynamic Equations

In this appendix we describe the numerical method that we use to integrate equations (5.32)-(5.34), which is a non-linear partial hyperbolic system. These equations are proposed to study the temporal evolution of the flow resulting after a SN explosion that goes off in the centre of a stellar cluster wind (see subsection 2.4).

We use the Van Leer *Flux Vector Splitting* (Van Leer 1982) which gives the hydrodynamic variables ρ, v and p at each timestep, given the initial values of the flow. As we discussed in section 2.3, the problem can be studied with spherical symmetry, which results in a 1-D spatial problem.

The system of equations (5.32)-(5.34) can be written in vector form as

$$\partial_t \mathbf{U} + \partial_R \mathbf{F} = \mathbf{S}, \tag{A.1}$$

where

$$\mathbf{U} = \begin{pmatrix} \rho \\ \rho v \\ E \end{pmatrix}, \ \mathbf{F} = \begin{pmatrix} \rho v \\ \rho v^2 + p \\ v(p+E) \end{pmatrix}, \ \mathbf{S} = \begin{pmatrix} -\frac{2\rho v}{R} + n\dot{M}_w \\ -\frac{2\rho v^2}{R} \\ -\frac{2v(E+p)}{R} + \frac{1}{2} n\dot{M}_w v_w^2, \end{pmatrix}, \tag{A.2}$$

with $E = \rho v^2/2 + p/(\gamma - 1)$.

If we discretise the spatial domain, in N computational cells, we can define at a time t the matrix $U(t)$ of *conserved quantities*, with matrix elements U_{ij}^t; $i =$

$1, 2, ...N$, $j = 1, 2, 3$ as

$$U_{i1}^t = \rho_i, \tag{A.3}$$

$$U_{i2}^t = \rho_i v_i \tag{A.4}$$

$$\text{y } U_{i3}^t = \frac{1}{2}\rho_i v_i^2 + \frac{p_i}{\gamma - 1}. \tag{A.5}$$

Analogously, we define the elements of the matrices $F(t)$ y $S(t)$.

If the time t is the initial time $t = 0$, the matrices $U(t)$, $F(t)$ y $S(t)$ are defined with the values of the hydrodynamic variables ρ_i y v_i y p_i that we set up as initial condition of our problem This is the stationary cluster wind flow, for which we use the analytic fits given in Appendix B, (since the exact solution of the cluster wind flow is given in implicit form) together with the hot ball of ejected material, due to the SN explosion (see Section A.3 of appendix A).

Then, the elements of the evolved matrix $U(t + \Delta t)$ of conserved quantities is obtained as

$$U_{ij}^{t+\Delta t} = U_{ij}^t - \frac{\Delta t}{\Delta R}\left[(f_{ij}^+ + f_{i+1j}^-) - (f_{i-1j}^+ + f_{ij}^-)\right] + \Delta t S_{ij}, \tag{A.6}$$

where the elements of the flux matrices f_{ij}^+ y f_{ij}^- are calculated as

$$\mathbf{f}^+ = \begin{pmatrix} \frac{\rho c}{4}(M+1)^2 \\ \frac{\rho c^2}{4\gamma}(M+1)^2\left[(\gamma-1)M+2\right] \\ \frac{\rho c^3}{4}(M+1)^2\left[(\gamma-1)M+2\right]^2 / \left[2(\gamma^2-1)\right] \end{pmatrix}, \tag{A.7}$$

and $\mathbf{f}^- = \mathbf{F} - \mathbf{f}^+$ if $|M| < 1$.

$\mathbf{F}$ is the flux matrix given by (A.2) and equation (A.7) is written in terms of the sound speed $c = \sqrt{\gamma p/\rho}$ and the *Mach number* $M = v/c$.

For the supersonic case, there is no partition in the flux, and then

$$\mathbf{f}^+ = \mathbf{F} \quad \text{if } M > 1, \tag{A.8}$$

$$\mathbf{f}^- = \mathbf{F} \quad \text{if } M < -1. \tag{A.9}$$

ΔR is the spatial separation between successive computational cells, which we con-

sider as fixed. The size of the timestep Δt is calculated with the *Courant criterion*

$$\Delta t = \frac{C_0}{max_i\{(|v| + c)/\Delta R_i\}} \ , \tag{A.10}$$

where $C_0 < 1$ is the *Courant number*, and we use $C_0 = 0.6$.

This algorithm for calculating the matrices $\mathbf{f}^+$ y $\mathbf{f}^-$ is the so-called Van Leer *Flux Vector Splitting method*, which is obtained from 7 suitable mathematical criteria, for the propagation of shock in the gas dynamic equations (see Van Leer, 1982).

Appendix B

Analytic Fit to the Implicit Solution of the Cluster Wind

The analytic solution for the radial velocity of the cluster wind, given in the model of Cantó et al. (2000) for a spherical stellar cluster with a uniform distribution of stars is

$$u_e \left[1 + \frac{5\gamma+1}{\gamma-1} u_e^2\right]^{-(3\gamma+1)/(5\gamma+1)} = A_\gamma r, \tag{B.1}$$

for the wind flow inside the cluster, and

$$u_e (1 - u_e^2)^{1/(\gamma-1)} = \frac{B_\gamma}{r^2}, \tag{B.2}$$

for the wind flow outside the cluster, with A_γ and B_γ two constants which depend on the specific heat ratio $\gamma = c_p/c_v$:

$$A_\gamma = \left(\frac{\gamma-1}{\gamma+1}\right)^{1/2} \left(\frac{\gamma+1}{6\gamma+2}\right)^{(3\gamma+1)/(5\gamma+1)}, \tag{B.3}$$

$$B_\gamma = \left(\frac{\gamma-1}{\gamma+1}\right)^{1/2} \left(\frac{2}{\gamma+1}\right)^{1/(\gamma-1)}, \tag{B.4}$$

where r is the radius in units of the cluster radius R_c, and u_e the flow velocity in units of the terminal wind velocity of the single stars v_w. We have fitted these

implicit solutions for the velocity u_e with simple explicit functions of the radius r

$$u_e = \begin{cases} A_\gamma \left[r^{-1} + (2A_\gamma - 1)\, r^3 \right]^{-1} & \text{for } r < 1, \\ \frac{1}{2} + \frac{2}{5}(r-1)^{1/3} & \text{for } 1 < r < 2, \\ \left(1 + \frac{1}{3} r^{-3/2}\right)^{-1} & \text{for } r > 2\,. \end{cases} \tag{B.5}$$

This velocity as a function of radius is appropriate for building our semi-analytic model of the SNR evolution of section 3, and for setting up the initial conditions of the numerical simulations of the gasdynamic equations in section 4. In Figure C.1 we show a comparison of the exact implicit solutions given by equations (B.1), (B.2) with our fits of the velocity as a function of radius.

With the help of equation (B.5) we also obtain the cluster wind density ρ_e, in units of the central density ρ_c, as a function of radius r, according to the model of Cantó et al (2000)

$$\varrho_e \equiv \frac{\rho}{\rho_c} = \begin{cases} A_\gamma r / u_e & \text{for } r < 1, \\ A_\gamma / \left(r^2 u_e\right) & \text{for } r > 1\,. \end{cases} \tag{B.6}$$

By using the analytic fits given in equation (B.5) together with equation (5.2), the integral of equation (5.5), which also appears in the RHS of equation (5.25), has an analytic expression:

$$I(r) \equiv \int_0^r r'^2 \varrho(r') dr'$$

$$= \begin{cases} I_1(r) - I_1(0) & \text{for } r < 1, \\ I_1(1) - I_1(0) + I_2(r) - I_2(2) & \text{for } 1 < r < 2, \\ I_1(1) - I_1(0) + I_2(2) - I_2(1) + I_3(r) - I_3(2) & \text{for } r > 2\,. \end{cases} \tag{B.7}$$

with

$$I_1(r) = \frac{r^3}{3} + (2A_\gamma - 1)\, \frac{r^7}{7}, \tag{B.8}$$

$$I_2(r) = A_\gamma \frac{15}{32} \left[8(r-1)^{2/3} - 20(r-1)^{1/3} + 25 \ln\{4(r-1)^{1/3} + 5\} \right], \tag{B.9}$$

$$I_3(r) = A_\gamma \left(r - \frac{2}{3} r^{-1/2} \right). \tag{B.10}$$

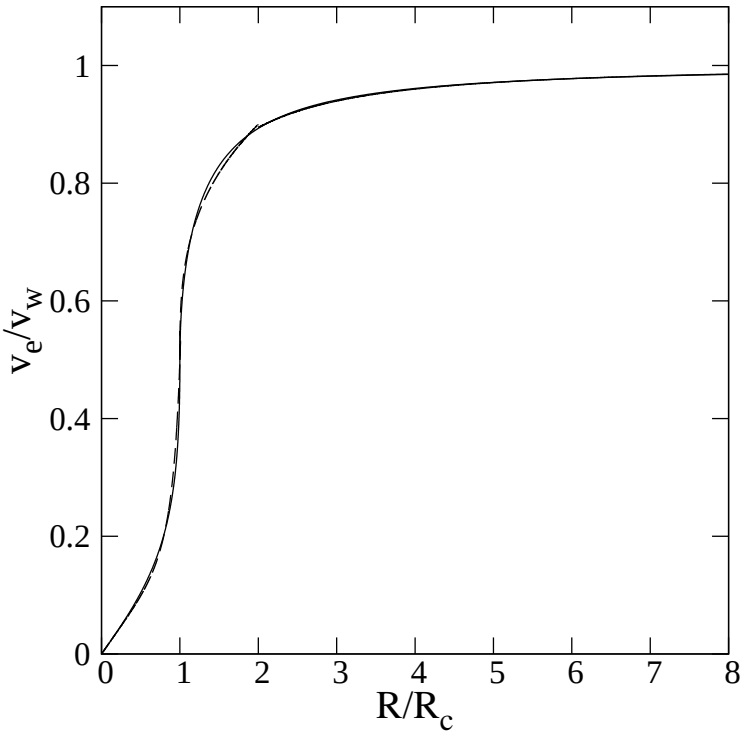

Figure B.1: Analytic fit for the cluster wind velocity as a function of radius (dashed line) given in equation (B.5), and the exact implicit analytic solution (solid line), given by equations (B.1) and (B.2), for the stationary cluster wind velocity model of Cantó et al. (2000). We plot the velocity in units of v_w (the wind velocity of the individual stars) as a function of radius in units of the cluster radius R_c.

Appendix C

Glossary of Abbreviations, Constants and Symbols

Ejecta: Ejected material.

Feedback: Radiative and mechanical energy injected by massive stars into the interstellar medium.

H: Hydrogen atom.

He: Helium atom.

HII: Ionised hydrogen.

ISM: Interstellar medium.

IMF: Initial mass function.

LHS: Left hand side.

OIII: doubly ionised oxygen.

RHS: Right hand side.

SF: Star formation.

SN: Supernova.

SNR: Supernova remnant.

T-S: Taylor-Sedov, in the context of the non-radiative phase of supernova remnants.

UC HII region: ultracompact HII region.

X-ray: Electromagnetic radiation with wavelengths in the range of 0.01 -10 nm.

L_*: Stellar luminosity, (erg s^{-1}).

S_*: Ionising photon rate, (s^{-1}).

$\gamma = C_P/C_V$, specific heat ratio.

$M_\odot = 1.99 \times 10^{33}$ g, solar mass.

$L_\odot = 3.9 \times 10^{33}$ erg s^{-1}, solar luminosity.

yr= year.

$m_H = 1.673 \times 10^{-24}$ g, hydrogen mass

pc=3.086×10^{18} cm, parsec.

$h = 6.626 \times 10^{-27}$ erg s, Plank constant.

$k = 1.38 \times 10^{-16}$ erg K^{-1}, Boltzmann constant.

$G = 6.672 \times 10^{-8}$ cm^3 g^{-1} s^{-2}, gravitational constant.

$c = 2.997 \times 10^{10}$cm s^{-1}, speed of light in vacuum.

References

Adams F. C. & Fatuzzo M. 1996, ApJ, 464, 256

Banerjee A., Jog C. J., Brinks E., Bagetakos I. 2011 MNRAS 415, 687

Barnabè M., Ciotti L., Fraternali F., Sancisi R. 2006, A&A 446, 61

Bisnovatyi-Kogan G. & Silich S., 1995, RvMP, 67, 661

Cantó J., Raga A.C., Rodríguez L.F. 2000, MNRAS, 896, 901

Capriotti E., Kozminski J. 2001, PASP, 113, 667

Carral P., Kurtz S., Rodríguez L. F., Menten K., Cantó J., Arceo, R., 2002, AJ, 123, 2574

Castor J., McCray R., & Weaver R. 1975, ApJ, 200, L107 Chevalier R. A. & Clegg A. W., 1985, Nature, 44, 45

Chernyi G. G., 1957, Dokl. Akad. Nauk. SSSR, 112, 213

Choudhuri, A. R., The physics of fluids and plasmas : an introduction for astrophysicists, Cambridge University Press, 1998

Chu Y-H. & Mac Low M., 1990, Apj, 365, 510

Draine B. 2011, ApJ, 732, 100

Dekel A. & Silk J., 1986, Apj, 303, 39

De Pree C. G., Wilner D. J., Deblasio J., Mercer A. J., & Davis, L. E., 2005,

ApJ, 624, L101

Dopita M. A., Groves B. A., Sutherland R. S., Kewley L. J., 2003, ApJ, 583, 727

Faucher-Giguere C. A., Quataert E., Hopkins P. F., 2013, MNRAS, 433, 1970

Ferrara A. 1993, ApJ, 407, 157

Franco J., Ferrini F., Ferrara A., Barsella B. 1991, ApJ, 366, 443

Franco J., Tenorio-Tagle G., Bodenheimer P. 1990, ApJ, 349, 126

Genzel et al. 2010, MNRAS, 407, 2091

Harper-Clak E. & Murray N., 2009, ApJ, 693, 1696

Haehnelt M. G., 1995, MNRAS, 273, 249

Hoffmann W. F., Dayal A., 2001, ApJ, 561, 282

Inoue A., 2002, ApJ, 579, 688

Jaskot A. E., Strickland D. K., Oey, M. S., Chu, Y.-H., García-Segura, G., 2011, ApJ, 729, 28

Jeans J. H. 1902, RSPTA, 199,1

Jun B. I., Norman, M. L. 1996, ApJ, 465, 800

Kennicutt R. C., Jr. 1998, ApJ, 498, 541

Kim J-G., Kim W-T, Ostriker E. C. 2016, ApJ 819, 137

Kim K-T. & Koo B-C., 2001, ApJ, 549, 979

Kraemer K. E., Jackson J. M., Deutsch L. K., Kassis M., Hora J. L., Fazio G. G.,

Krumholz M. R., Matzner C. D. 2009 ApJ 703, 1352

Kurtz S., Cesaroni R., Churchwell E., Hofner P., Walmsley, C. M. Protostars and Planets IV, Tucson: University of Arizona Press p. 299-326

Kurtz S. & Franco J. 2002 RMxAA Conf, 12, 16

Kurtz S. 2005, in *Massive star birth, a crossroads of astrophysics*, eds. Cesaroni R. et al. (Cambridge: Cambridge Univ. Press), p. 111

Larson R. B., 1974, MNRAS, 169, 229

Ledoux P., 1951, Ann Astrophys., 14, 438

Leroy A. K., Walter F., Brinks E., Bigiel F., de Blok W. J. G., Madore B., Thornley M. D., 2008, AJ 136, 2782

Martínez-González S., Silich S., Tenorio-Tangle G., 2014 ApJ 785, 164

Martins F., Schaerer D., Hillier D. J. 2005 A&A 436, 1049 Matzner, C. D. 2002 ApJ 566, 302

McKee C. F. & Ostriker E. V. 2007 ARA&A, 45, 565

McKee C. F. & Ostriker J. P. 1977, ApJ, 218, 148

Murray N., Quataert, E., Thompson T. A., 2005, ApJ, 618, 569

Murray N., Quateart E., Thompson T. A., 2010, ApJ, 709, 191

Natta A. & Panagia N. 1976, A&A, 50, 191

Osterbrock D.E. and Ferland Sausalito G. J., Astrophysics of gaseous nebulae and active galactic nuclei, 2nd.ed. CA: University Science Books, 2006.

Pérez-Rendón B., García-Segura G., Langer N., 2009, A&A, 506, 1249

Petrosian V., Silk J., Field G. B. 1972, ApJ, 177, L69

Raga A. C. & Lora V. 2015, RMxAA, 51, 189

Raga A. C., Cantó J., Mellema G., Rodríguez-González A., Esquivel A. 2015, RMxAA, 51, 27

Raga A. C., Cantó J., Rodríguez L. F. 2012a, MNRAS, 419, L39

Raga A. C., Cantó J., Rodríguez L. F. 2012b, RMxAA, 48, 199

Raga A. C., Cantó J., Rodríguez L. F., Velázquez, P. F., 2012c MNRAS 424, 2522

Rodríguez-González A., Velázquez P. F., Rosado M., Esquivel A., Reyes-Iturbide, J., Toledo-Roy, J. C., 2011, ApJ, 733, 34

Rodríguez-Ramírez J. C., Raga A. C., Velázquez P. F., Rodríguez-González A., Toledo-Roy J. C., 2014, MNRAS, 445, 1023

Rodríguez-Ramírez J. C. & Raga A. C., 2016, MNRAS, 460, 1876

Rodríguez-Ramírez J. C., Raga A. C., Lora V., Cantó J. 2016, ApJ, 833, 256.

Rosen A., Lopez L., Krumholz M., Ramírez-Ruiz E., MNRAS, 442, 2701

Salpeter E. E., 1955, ApJ, 121, 161

Sedov L. I., 1959, *Similarity and Dimensional Methods in Mechanics. Academic Press, New York*

Shu F., 1991 *The physics of astrophysics, Vol II: Gas Dynamics* University Science Books.

Silich S., Tenorio-Tagle G., Rodríguez-González A. 2004, ApJ, 610, 226

Silich S. & Tenorio-Tagle G., 2017, MNRAS, 465, 1375

Sternberg A., Hoffmann T. L., Pauldrach A., 2003, ApJ 599, 1333

Stevens I. & Hartwell J. 2003 MNRAS, 339, 280

Taylor G. 1950, Proc. R. Soc. Lond. 201, 159

Tan S. & Wang Q., 2005, ApJ, 628, 205

Thompson T. A., Quataert E., Murray N. 2005 ApJ, 630, 167

Tinoco-Arenas A., González-Bolívar M., Medina-Cobarrubias R., Raga A. C. 2015, RMxAA, 51, 241

Truelove J. K., McKee C. F. 1999, ApJS, 120, 299

Van Leer B., 1982 ICASE Report No. 82-30

Veilleux S., Rupke D., Swaters R., 2009 ApJ, 700L, 149

Velázquez P. F., Vigh, C. D., Reynoso, E. M., Gómez, D. O., Schneiter, E. M., 2006, ApJ, 649, 779

Walter F., Weiss A., Scoville N., 2002, ApJ, 580L, 21

Weaver, R., McCray, R., Castor, J., Sharpiro, P., & Moore, R. 1977, ApJ, 218, 377

Woosley S., Janka T., 2005, Nature, 147, 154

Yeh S., Matzner C., 2012, ApJ, 757, 108

Zeldovich I. A., Raizer Y. P., 1967, Physics of Shock Waves and High-Temperature Hydrodynamic Phenomena. Academic Press, New York